8-1-2024

# Advancements in Aerial Vehicle Platforms: A Guide for Design, Validation, and Implementation of 3D Printed Drones

Alan Salvador Urteaga
*The University of Texas Rio Grande Valley*

## Recommended Citation

Urteaga, A. S. (2024). *Advancements in Aerial Vehicle Platforms: A Guide for Design, Validation, and Implementation of 3D Printed Drones* [Master's thesis, The University of Texas Rio Grande Valley]. ScholarWorks @ UTRGV. https://scholarworks.utrgv.edu/etd/1593

# ADVANCEMENTS IN AERIAL VEHICLE PLATFORMS: A GUIDE FOR DESIGN, VALIDATION, AND IMPLEMENTATION OF 3D PRINTED DRONES

A Thesis
by
ALAN SALVADOR URTEAGA

Submitted in Partial Fulfillment of the
Requirements for the Degree of
MASTER OF SCIENCE IN ENGINEERING

Major Subject: Mechanical Engineering

The University of Texas Rio Grande Valley
August 2024

# ADVANCEMENTS IN AERIAL VEHICLE PLATFORMS: A GUIDE FOR DESIGN, VALIDATION, AND IMPLEMENTATION OF 3D PRINTED DRONES

A Thesis
by
ALAN SALVADOR URTEAGA

COMMITTEE MEMBERS

Dr. Constantine Tarawneh
Chair of Committee

Dr. Arturo Fuentes
Committee Member

Dr. Farid Ahmed
Committee Member

August 2024

# ABSTRACT

Urteaga, Alan S., Advancements In Aerial Vehicle Platforms: A Guide for Design, Validation, and Implementation of 3D Printed Drones. Master of Science in Engineering (MSE), August 2024, 134 pp., 5 tables, 117 figures, 128 references.

Additive manufacturing methods have revolutionized the way products are designed and developed through a product's entire design life cycle. This is in part correlated with the nature of additive manufacturing methods that differentiate them from traditional methods. Some of the benefits of additive manufacturing methods include customizability, rapid prototyping, the production of complex design geometry, and embedded assembly manufacturing. Unmanned aerial vehicles have been on the rise for various military, commercial, or personal applications. The focus of this study is to provide detailed instructions on how to engineer a viable drone design that is impact-resistant, modular, and customizable. This study will encompass everything from the design and iterations of components, the calculations and validation, experimental testing procedures, and results and discussion on 3D-printed drone components. The drone design discussed in this thesis was devised and fabricated with the end purpose of using integrated sensors that would allow the onboard computer system to be able to detect the presence of a crack formation through the sensor feedback. Other researchers are currently developing these sensors as part of a joint project initiative in our CREST Center for Multidisciplinary Research Excellence in Cyber-Physical Infrastructure Systems (MECIS).

# DEDICATION

This thesis is dedicated to my family and friends who have encouraged and supported me throughout my entire higher education career. To my father, Miguel Urteaga, and my mother, Maria Isabel Urteaga, I am forever grateful for your love, and support. To my brother, Miguel, thank you for being there for me on those days. To my friends, who have been like brothers to me and helped me out when I was away from my family, Alejandro, Emiliano, Antonio, and Jahaziel. I thank you for being like family and making me feel like I had a home away from home.

# ACKNOWLEDGMENTS

I am grateful for the financial support I received to conduct this research and obtain my master's. I would like to acknowledge funding provided by the National Science Foundation CREST Center for Multidisciplinary Research Excellence in Cyber-Physical Infrastructure Systems (NSF Award No. 2112650). This work was also partially funded by the following scholarships Daniel Foltz Memorial Scholarship, the Lloyd M. Bentsen Jr Engineering Scholarship, and the Center of Equity in Engineering.

I am grateful to Dr. Constantine Tarawneh for the support and guidance given during my research. I could not have completed my project without your help. Without your guidance in my academic and personal life, I would not have become the man that I am today. I have learned much from you, more than just heat transfer. Thank you for being my mentor and teacher

I am grateful to Dr. Arturo Fuentes for your help with my sanity check calculations and finite element analysis. Without your input, I would not have been able to accurately validate my designs and their performance on the drone assembly. I appreciate your help in looking through my calculations and confirming/correcting my assumptions.

I am grateful to Dr. Farid Ahmed for your help in providing a valuable perspective on the project. Without your input, I would not have been able to represent my work professionally. I appreciate your insights into the manufacturing aspects of my work.

## TABLE OF CONTENTS

# LIST OF TABLES

Page

LIST OF FIGURES

# CHAPTER I

## BACKGROUND AND INTRODUCTION

The objective of this study is to establish a comprehensive design process for a drone assembly manufactured through the implementation of additive manufacturing methods. Additionally, the study explains how to integrate sensors into the drone assembly. The ultimate application for these drones is to develop a fleet of drones equipped with embedded sensors to help aid the Federal Highway Administration (2024) by detecting crack formation in transportation infrastructure (BubsBuilds, 2023; Liu, 2021). This study is organized into the following chapters:

1. Background and Introduction (Chapter I): This chapter delves into the various additive manufacturing methods, material selection, and various drone designs, including additive-manufactured drone designs.
2. Design (Chapter II): This chapter delves into the various iterations of the drone design along with the optimal design features for the chosen additive manufacturing method.
3. Calculations and Finite Element Analysis (Chapter III): This chapter delves into the various calculations required to validate design features, accompanied by Finite Element Analysis (FEA). FEA is a numerical solver approximation model simulation used to validate individual part components, quantified by a simplified model analytical solution.

4. Manufacturing (Chapter IV): This chapter delves into optimal slicing parameters for manufacturing drone components using Prusa slicer software and the MK3s+ hardware.
5. Testing Procedures (Chapter V): This chapter delves into the different procedures for setting up and testing the manufactured components.
6. Chapter VI “Results and Discussion discusses the results obtained from testing and how they relate to the calculations and validations. Chapter VII “Conclusion and Future Work” summarizes the work done in this study, identifies the limitations, and suggests future work for the drone project.

## 1.1 Additive Manufacturing Methods

Additive manufacturing was first patented and invented by Hideo Kodama, at the Nagoya Municipal Industrial Research Institute in Japan in 1980. His original patent was for the manufacturing of rapid prototypes using a laser and vat of polymer resin that would harden when exposed to the laser ultraviolet (UV) light beams called stereolithography (SLA) (Su, 2018). This form of additive manufacturing has limitations to the end application of the drone assembly. The main advantages of this manufacturing process include high part resolution, high dimensional accuracy, and better layer adhesion (AlexPrint, 2023). However, SLA has limitations, including high yearly costs, extensive post-processing, and cannot have integrated parts (AlexPrint, 2023; Bryant, 2024; Shaikhang, 2020).

Another form of additive manufacturing is selective laser sintering (SLS). SLS utilizes a high-temperature laser to fuse metal or polymer powder into solid layers (Su, 2018). The Advantages of this additive manufacturing method include high dimensional accuracy, and near homogeneous mechanical properties (Xometry, 2022). However, SLS has several limitations including high initial and recurrent costs, warping on large flat surfaces, and limited commercial availability (Xometry, 2022).

Another additive manufacturing method is fused deposition modeling (FDM). FDM utilizes a heated extruder nozzle and polymer filament to manufacture components. FDM produces components by extruding molten polymer through a heated nozzle and depositing it onto a build plate to form a layer (Su, 2018). FDM is low-cost, open-sourced, customizable, and commercially available (AlexPrint, 2023; Bryant, 2024). Other interesting forms of additive manufacturing that employ similar mechanical operations as FDM include extrusion-based ceramics and 3D concrete printing (3DCP) (Buswell, 2018; Hergel, 2019). For this study, FDM emerged as the most optimal choice due to its advantages over SLA and SLS. Among the available FDM machines in the current market, the Prusa MK3s+ stood out for its reliability, open-sourced design, affordability, upgradability, material versatility, and huge community support (Bryant, 2024).

## 1.2 Material Selection

The MK3s+ 3D printer is compatible with a wide range of thermoplastic filaments. When selecting proper manufacturing materials for any application it is essential to evaluate the mechanical properties. The design expectations for the drone design include impact resistance, high material stiffness, wear resistance, thermal resistance, UV resistance, low density, and creep resistance. Additionally, cost-effectiveness and manufacturing complexity should be considered.

Two notable flexible and tough filament options are polypropylene (PP) and thermoplastic polyurethane (TPU). While PP is difficult to manufacture consistently TPU does not (Freedman, 2021). TPU exhibits excellent mechanical and material properties such as a high ultimate tensile strength (UTS) of 30 MPa, hygroscopic, temperature resistance up to 74°C, 0.06 g mass loss after the ASTM D4060 test, not suitable for prolonged UV exposure, 580% elongation before breaking, and a density of 1.22 g/cm$^3$ (3DSourced, 2024; Dynamism, 2022).

It is important to note that for FDM material properties of similar filament materials may vary in mechanical properties between filament manufacturers. For further insights, a YouTube channel “My Tech Fun” did some material testing on additive-manufactured components with the Polymaker TPU (My Tech Fun, 2022). Their results for the tensile tested samples of TPU 95A resisted a force equivalent of that produced by 46 kg. Converting this mass value to a force value and then a stress value uses the following equation for maximum axial stress.

$$\sigma = \frac{P}{A_C} \tag{1}$$

Where sigma (σ) is the stress induced by a load (P), acting over a cross-sectional area ($A_c$). Using the load and cross-sectional area values obtained from the source the UTS calculated is 28.2 MPa. This UTS value for TPU differs from the previously stated values mentioned in the material properties. This variation confirms the observable deviation of material properties between different manufacturers. Another study by “My Tech Fun” tested for the creep compliance of TPU. The results revealed minimal creep behavior after initial deformation. However, the limitations of this study include a small sample size of two samples and a non-standard testing setup (My Tech Fun, 2022). Being hygroscopic, TPU needs to be dried before or during the manufacturing process. Failure to properly dry TPU will affect layer line adhesion, surface quality, and mechanical properties of the manufactured component (Made With Layers, 2021).

Among commonly used FDM filament materials polylactic acid (PLA) stands out as the most popular choice. PLA exhibits a high UTS of 40 MPa and is biodegradable. (CNC Kitchen, 2020; 3DSourced, 2024; Hsueh, 2021; My Tech Fun, 2021; Trivedi, 2023). The YouTube channel "CNC Kitchen" tested PLA against polyethylene terephthalate glycol (PETG), and acrylonitrile styrene acrylate (ASA) (2020). In this experiment "CNC Kitchen" observed that PLA is more resistant than PETG and ASA in the G-hook tensile testing, less thermal resistant than PETG and ASA, and has a lower impact resistance than PETG and ASA. The study's limitations include a small sample size of three samples and a non-standard testing setup. These results show that PLA is not a suitable material for applications where elevated temperatures and impact loading are acting on the body. The YouTube channel "My Tech Fun" explored the creep compliance of multiple materials such as PLA, PETG, ASA, and polyamide (Nylon) (2021). The results of this experiment showed that ASA demonstrated the highest creep resistance, with 13.33 mm of permanent deformation after 6 days, followed closely by PETG with 14.69 mm. PLA and Nylon exhibited the worst performance with 28.79 mm and 26.77 mm of permanent deformation, respectively. The limitations of this study include the small sample size and non-standard testing equipment. Other researchers have formally explored the creep compliance of additive-manufactured components (Dogan et al., 2022). The materials tested were PLA, tough polylactic acid (TPLA), acrylonitrile butadiene styrene (ABS), polyethylene (PE), and polycarbonate (PC). Their findings revealed that PC had the highest creep resistance with a high load of 20 Mpa at an elevated temperature of 60°C. PLA was observed to have the lowest creep resistance. The researchers elaborate further by cautioning against the use of PLA for high-loading applications, especially in environments with higher temperatures than the ambient temperature of 25°C. ABS and PE were identified to be suitable for medium loading (10 MPa – 20 MPa) applications with moderate temperatures (25°C - 40°C).

ABS exhibits good mechanical properties but also exhibits considerable material limitations such as poor UV resistance, extreme warping, and the production of toxic by-products during manufacturing (Dogan, 2022; Polygenis, 2023). ASA has similar material properties to ABS, differing only by having better UV resistance and producing more toxic by-products during manufacturing (Freedman, 2021; My Tech Fun, 2021).

High-impact polystyrene (HIPS) is another polymer of interest. HIPS exhibits reasonable mechanical and material properties including an elastic modulus of 1.9 GPa, 40% elongation before fracture, impact strength of 45 J/m, solubility in d-limonene, recyclability, non-hygroscopic, and a density of 1 g/cm$^3$ (MakeItFrom, 2020; Xometry, 2023).

PETG exhibits great mechanical and material properties including an elastic modulus of 2.2 GPa, impact strength of 77 J/m, chemical resistance, UTS of 53 MPa, UV resistance, thermal resistance below 69°C at 1.82 MPa, creep resistance, a yield compressive strength of 35 MPa, and a density of 1.3 g/cm$^3$ (CNC Kitchen 2020; 3DSourced, 2024; Freedman, 2021; Miller, 2023; My Tech Fun, 2021; Polygenis, 2023; MakeItFrom, 2020; Valvez, 2022; Wu, 2018).

Valvez et al. explored the compressive behavior of PETG and fiber-reinforced composites of PETG to assess the material properties of composite polymers (Valvez et al., 2022). Their findings revealed that the yield compressive strength of neat PETG surpassed that of the various PETG composites tested.

In summary HIPS, PETG, and TPU each offer distinct mechanical and material advantages suitable for the development of various drone components. Considering the specific requirements such as high impact and bending loading resistance, elevated temperature resistance, UV resistance, creep resistance, low density, manufacturability, and affordability.

### 1.3 Drone Design Selection

Various UAV design formats have emerged, categorized into four distinct design languages: fixed-wing, rotary motor, vertical takeoff and landing (VTOL), and bio-mimetic designs. Fixed-wing drone designs resemble plane designs featuring traditional fixed airfoil wings that generate lift through forward thrust (Hassanalian, 2017; Phan, 2019; Stanton, 2016; Stanton, 2022). The advantage of a fixed-wing drone design lies in their extended flight time, this benefit comes at the cost of limited mobility making these designs unable to hover during flight. Figure 1 shows a 3D-printed fixed-wing drone design developed by the YouTube channel "Stanton" in 2016.

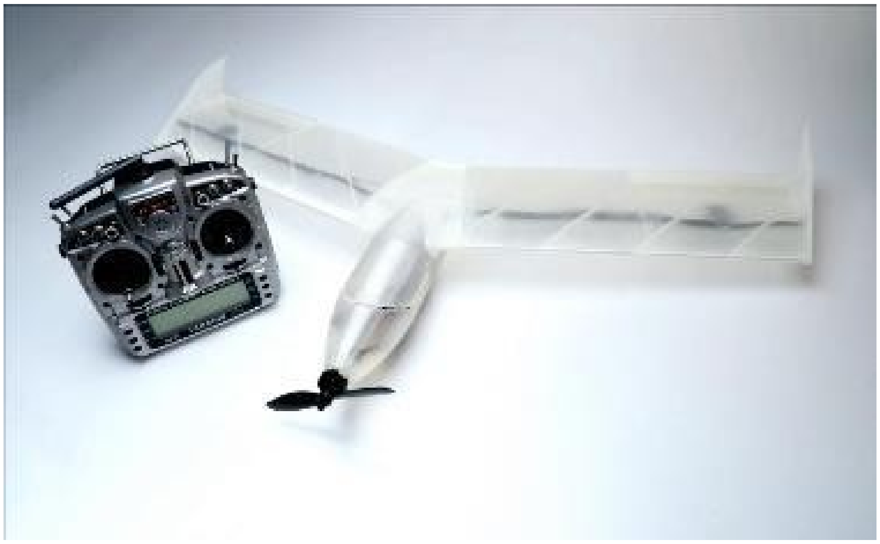

Figure 1: 3D Printed Fixed Wing Drone (Stanton, 2016).

The rotary motor drone design employs a combination of motors and propellers to achieve vertical lift (Gadget Flow, 2023; Hassanalian, 2017; Palomba, 2022; RCLifeOn, 2020; Rechtin, 2024). Most notable for its high maneuverability is this drone design. However, the tradeoff for this design is its high-power consumption, resulting in short flight durations. Various rotary motor configurations exist, including the tri-copter, quadcopter, and octocopter. When selecting the number of meters in a rotary motor drone design configuration it is essential to recognize that each additional motor increases the overall power consumption. This increase in power consumption correlates with a reduction in flight duration (Hassanalian, 2017). Figure 2 shows a rotary motor design quadcopter kit from Holybro.

Figure 2: X500 V2 Quadcopter Drone kit (Holybro, 2023).

The VTOL design combines elements from both fixed-wing and rotary motor designs. By combining these elements, the VTOL is more efficient than a rotary motor and more maneuverable than a fixed-wing. However, the limitations include compact main bodies, and large wing and tail structure (Hassanalian, 2017; Stanton, 2022). Additive manufactured fixed-wing drones have been explored by Pecho et al., and the YouTube channel “Tom Stanton” (Pecho, 2019; Stanton, 2022).

Figure 3: VTOL Design (Stanton, 2022).

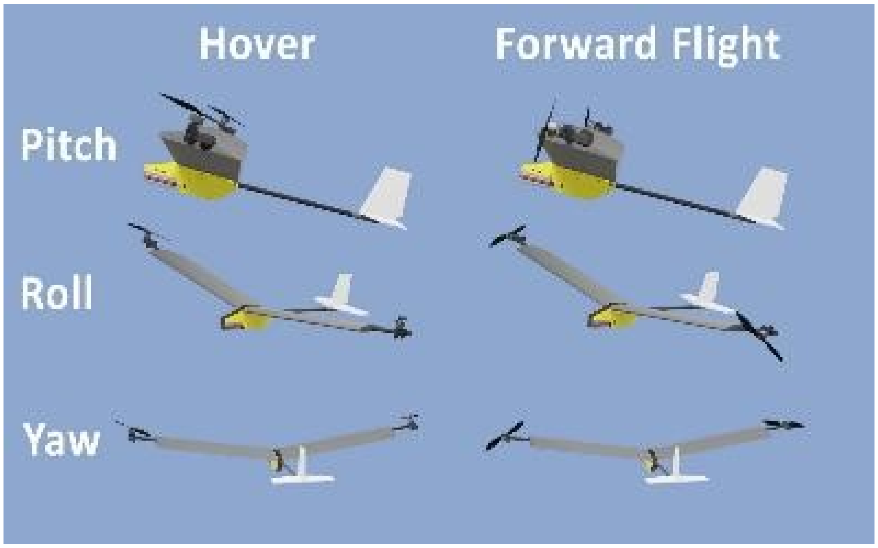

Figure 3: VTOL Design (Stanton, 2022).

The bio-mimetic drone design emulates the flight capabilities of biological organisms. These organisms exhibit a wide range of maneuverability, which aids in predation avoidance. Researchers exploring bio-mimetic structures aim to enhance the maneuverability of drones by incorporating these structures into UAV designs (Phan, 2020). However, the limitations include compressed bodies, short flight duration, and mechanical design limitations. Figure 4 shows various bio-mimetic drone designs being the topic of other research papers.

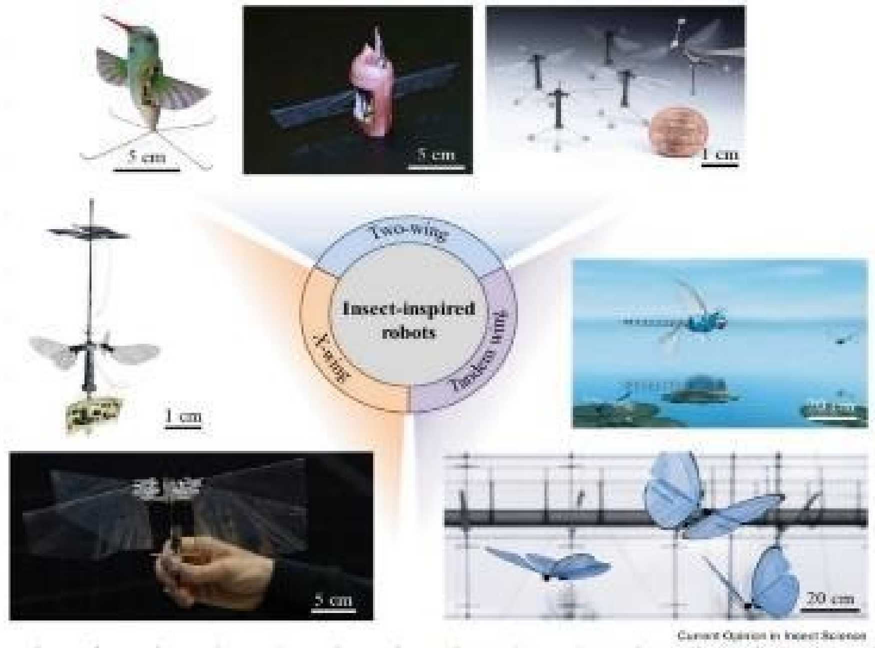

Figure 4: Bio-mimetic Drone Designs (Phan, 2020).

The final objective of this project is to create and manufacture a drone assembly that is modular, capable of embedding sensors, and robust. The embedded sensors application is to obtain sensor information that can identify crack formations on transportation infrastructure (BubsBuilds, 2024; Guidelines for Collection of Long-Term Pavement Performance Data, 2023; Liu, 2021). To achieve this objective, the drone needs to hover over infrastructure surfaces and accommodate all the necessary electrical components necessary for the condition monitoring task. The selected drone design that fulfilled these requirements is the rotary motor design, specifically the quadcopter configuration. The quadcopter configuration was selected for being the most stable motor configuration with the lowest power consumption.

Critical considerations for power consumption include the overall weight, propeller size, and motor power consumption (Hassanalian, 2017). Furthermore, onboard electronics increases the power consumption and overall weight. For this study, the X500 V2 kit was selected for its reliability and modularity. Necessary components that required integration include the Cube pilot orange flight controller, Hex Herew3+ CAN GNSS GPS, RFD 900x Modem, Nanotech 6000 Mah LiPo battery, the Logitech RealSense D455 camera, and the NVIDIA Jetson Nano. Given the price of these components, the robustness and resistance to impact were selected to be an important metric for the drone assembly.

Some impact-resistant drone configurations incorporate an exterior ball cage encompassing the entire quadcopter (Gadget Flow, 2023). Further discussion of impact resistance will be addressed in the subsequent chapters (Chapter 2, Chapter 3, Chapter 5, and Chapter 6).

## 1.4 Additively Manufactured Drone Design

Many enthusiasts and researchers have explored the design and manufacturing of additive-manufactured drones. In this study, the most notable ones will be examined and evaluated on the metrics relevant to the final objective for the proposed drone design.

Figure 5 shows a drone design that incorporates both additive manufactured components and metal screws and nuts as the main joining features. Notably, this design is open-sourced and has assembly instructions presented in the article. However, several limitations include the material selected being PLA, the absence of quantitative calculations and validation, and the absence of impact-resistant landing components (Robby-the-Robot, 2020).

Figure 5: Super Simple 3D Printed Drone Build (Robby-the-Robot, 2020).

Figure 6 shows a drone design that incorporates both additive manufactured components and polymer zip ties as the main joining feature. Notably, this drone design is open-sourced and can be assembled using the instructions provided in the article. A key attribute is the total lightweight frame weighing 110 g. However, the limitations include the material selected being PLA, the absence of impact-resistant and landing components, and the absence of quantitative calculations and validation (Brendan22, 2014).

Figure 6: T4 Quadcopter Mini 250 Drone (Brendan22, 2014).

Figure 7 shows a drone design that incorporates both additive manufactured components and metal screws and standoffs as the main joining features. Notably, this drone design is open-sourced and can be assembled using the instructions provided in the article. A key attribute is the total lightweight frame weighing 282 g. However, the limitations include the material selected not being specified, the absence of impact-resistant and landing components, and the absence of quantitative calculations and validation (treyes4, 2017).

Figure 7: Make an H Quadcopter with 3D Printing (treyes4, 2017).

Figure 8 shows a drone design that incorporates both additive manufactured components and metal screws and standoffs as the main joining features. Notably, this drone design is open-sourced and can be assembled using the instructions provided in the article. However, the limitations include the material selected not being PLA, the absence of impact-resistant and landing components, and the absence of quantitative calculations and validation (Nolan5454, 2017).

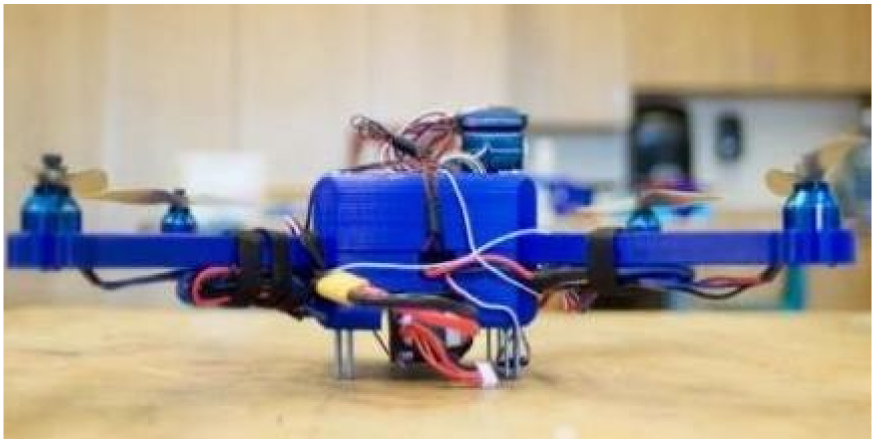

Figure 8: Printed Quadcopter with Arduino (Nolan5454, 2017).

Figure 9 shows a drone design that incorporates additive manufactured components and metal components in the hinge. Notably, this design is open-sourced, incorporates topology-optimized drone components, and has a design validated with FEA stress analysis and testing. However, the limitations include the material selection for the arms being PLA, the compact form factor, and the absence of impact-resistant landing gear (Rechtin, 2024).

Figure 9: Building a DIY 3D Printed FPV Race Quad (Rechtin, 2024).

Another notable example of an additive-manufactured drone design is the YouTube channel “RCLifeOn” (2020). “RCLifeOn” explored the material selection for the bottom frame of the drone, conducting informal testing. The most durable drone base with relative stiffness was fabricated in PP. Additionally, “RCLifeOn” explored the implementation of additive-manufactured propeller designs out of PLA and PETG (RCLifeOn, 2017). However, these propellers had some limitations including higher air resistance, increased sound production, and efficiency loss. Addressing the steps created during the slicing of curved geometries remains a challenge with traditional slicers. This obstacle can be overcome by implementing full control g-code (Glendall, 2021). Full control g-code allows the user to control the stepper motors of the 3D printer independently and can make the machine maneuver fully in three dimensions. Figure 10 shows the effect of implementing non-planar layer lines on a 3D print to better represent the component geometry. The implementation of non-planar g-code and manufacturing of additively manufactured propellers will not be discussed in this study.

Figure 10 shows the effect of implementing non-planar layer lines on a 3D print to better represent the component geometry. The implementation of non-planar g-code and manufacturing of additively manufactured propellers will not be discussed in this study.

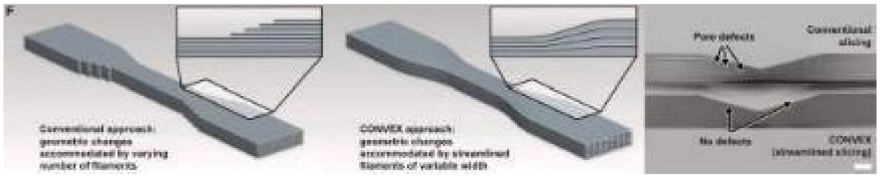

Figure: 10 Full Control Shape Optimization (Glendall, 2021).

Based on the literature review of additively manufactured drone designs, it is evident that previous designs lack comprehensive validation of their component design. To create a viable design that is robust and impact-resistant it is essential to analyze the components under stress loads induced by drone flight, landing, and impact. This study will explore how to validate the design of a quadcopter using engineering analysis and Finite Elements Analysis (FEA). Additionally, the optimal manufacturing parameters will be discussed from the existing literature review and component testing

# CHAPTER II

# DESIGN

## 2.1 Drone Version 0

The design for drone version 0 draws inspiration from the Holybro X-500 development kit. This quadcopter is in the X configuration, with arms 45° away from the body (Hassanalian, 2017; Holybro 2023). The modeling process utilized Shapr3D software with all components developed in metric units, aligning with dimensions obtained for hand calculations. During this initial design phase, detailed CAD models for the essential components of the Holybro X-500 kit were developed, CPU (NVIDIA Jetson Nano), Cube Orange flight controller, motors (Holybro Brushless 2216-920KV), Power Distribution Board (PDB), radio (RFD 900x), battery (Nano-tech 6000mah), propellers, GPS (Hex Here3), and D455 Logitech camera.

Figure 11 shows the CAD model of drone version 0 along with all the essential components developed within the Shapr3D software. Drone version 0 diverges from the Holybro X-500 kit in the design of the top boards, bottom boards, and arm standoff attachment sockets. The top and bottom boards have increased width and length, while the arm sockets are taller. These alterations to the Holybro X-500 kit allow the integration of the NVIDIA Jetson Nano within the main body of the drone. However, it is essential to emphasize that this design was intentionally modeled to replicate the Holybro X-500 kit. While the kit frame is not optimized for FDM, it serves as a foundational reference for subsequent drone iterations. Future iterations will utilize the essential components developed alongside drone version 0.

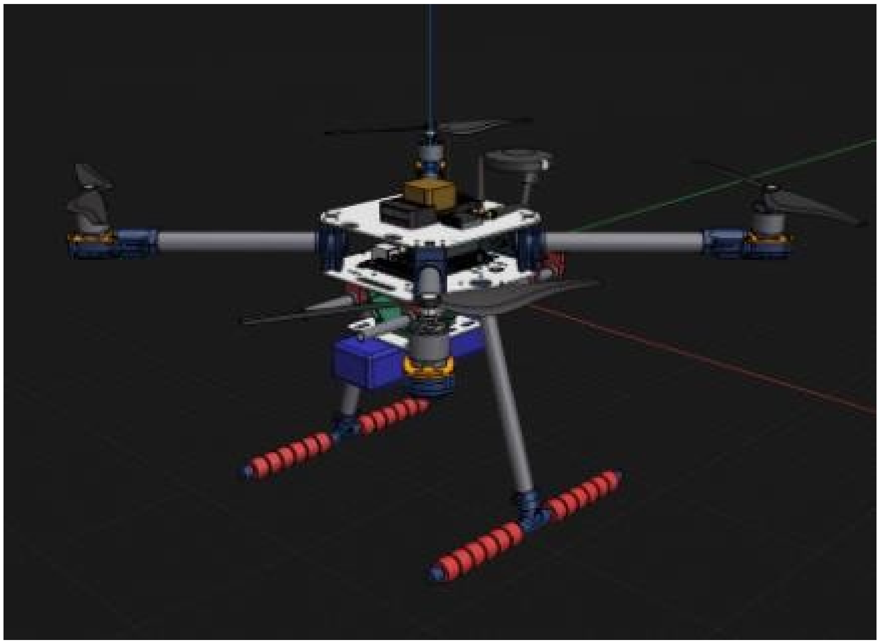

Figure 11: Drone Version 0.

## 2.2 Drone Version 1

The primary objective for drone version 1 was to develop an initial drone design that could serve as a foundation for iterative optimization while incorporating all the essential components. However, this initial approach was developed before properly understanding the weight limitations and manufacturing constraints for fused deposition modeling (FDM). Consequently, the weight of drone version 1 surpasses the thrust capabilities of the Holybro brushless motors, along with the FAA regulations for commercial use drones. Most of the weight for drone version 1 came from the inclusion of metal screw components like the drone designs explored in Chapter I (Robby-the-Robot, 2020; Brendan22, 2014; treyes4, 2017; Nolan5454, 2017; Rechtin, 2024). According to the manufacturer's test data sheet, these motors can produce a maximum thrust of 1332 g of thrust at 100% throttle (Holybro, 2023). To obtain the weight calculation the following equation was utilized.

$$w = \Sigma w_c + \Sigma w_L \tag{2}$$

Equation 2 calculates the total weight (denoted as w) by adding up the sum of the FDM component's weight (denoted as $w_c$) with the summation of the non-FDM component's weight (denoted by $w_L$). Utilizing Equation 2 for all the components within drone version 1 yielded a total weight of 28 kg. This weight is greater than five times the thrust capacity for all four motors. Furthermore, the Federal Aviation Administration (FAA) limits the weight of commercial/personal drones to less than 55 lb, with a maximum flight speed of 100 mph at an altitude of 400 ft. The 28 kg (equivalent to 61.6 lb) weight of drone version 1 also exceeded these limits (FAA, 2023; Micro Unmanned Aircraft Systems Aviation Rulemaking Committee, 2016). Consequently, drone version 1 underwent a redesign focusing on the reduction of weight to meet both the FAA regulations and project requirements.

Figure 12 shows the design of drone version 1. The complexity of both the arms and main body frame of the drone can be seen. These complex geometries prove to be very difficult to manufacture utilizing FDM methods. Therefore, the redesign of drone version 1 also considered altering the design to be better suited for FDM.

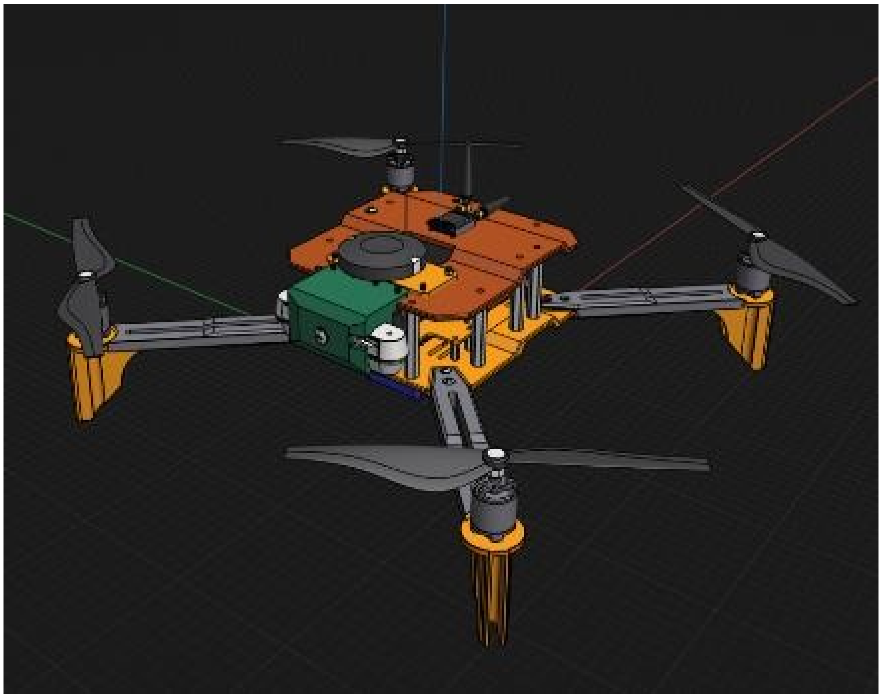

Figure 12: Drone Version 1.

### 2.3 Drone Version 2

Drone version 2 addresses both limitations of drone version 1 by streamlining the design and reducing the overall weight of the assembly. The weight optimization was achieved by replacing the heaviest components from drone version 1 (stainless steel standoffs) with polymer-based components (compliant mechanism body clips (BC)). Compliant mechanisms are features designed to flex as a desired response (BubsBuilds, 2024; Macro 3D Prints, 2023; Slan 3D, 2023). The design for BC was validated through an analytical and numerical analysis of a cantilever, further detailed in Chapter III.

Figure 13 shows the design of drone version 2. While the design improves upon that of drone version 1, the simplicity and roughness lend credence to some notable areas for improvement. Specifically, the placement of the legs on the arms requires further analysis and the main body remains asymmetrical. Notably drone version 2 relies on metal components such as M5 screws and threaded heat inserts for crucial structural joints. To meet the requirements for the project objective further iterations of the drone design needed to be developed to further eliminate the need for metal structural components.

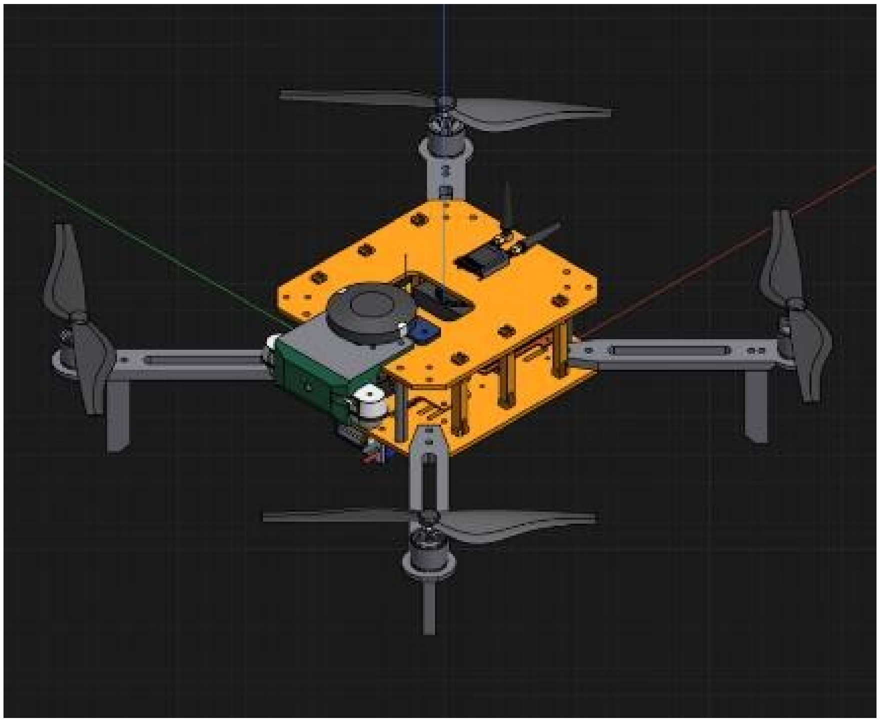

Figure 13: Drone Version 2.

### 2.3.1 Literature Review on Threaded Heat Inserts

The strength of threaded heat inserts and manufactured threaded designs have been discussed by the YouTube channels "Made with Layers (Thomas Sanladerer)", and "Slant3D" (2024, 2023). In the video produced by Made with Layers (Thomas Sanladerer) the best-performing heated inserts were the long heat-set inserts sold by CNC Kitchen with a failure torque of 1.38 N/m for the M5. The worst-performing threads were the FDM M5 threads with a 0.5 N/m failure torque. As stated in “Made with Layers (Thomas Sanladerer)” the main issue with any of these threads lies in achieving sufficient torque resistance to properly preload screw joints. The results of this study suggest that it is almost impossible to preload a screw with the current threads available for FDM components and that FDM threads can be used for certain applications. Further exploration into the mechanical properties of FDM threads and screws is essential to reducing the number of metal components.

### 2.3.2 FDM Screw and Threads Mechanical Strength

The design and implementation of additively manufactured screws and nuts have been explored by the YouTube channel “My Tech Fun” (2020). To design the screw and nut, “My Tech Fun” utilized an online vendor website (McMasterCarr) to obtain 3D models of a selected screw size (McMaster, 2023). Fusion 360 was employed by “My Tech Fun” to alter the design to see which design was most optimal for FDM. Noteworthy findings include the horizontally oriented M10 screw design which withstood a maximum force resistance equivalent to a mass of 289.2 kg before fracture. Additionally, a split design withstood a maximum force resistance of 267.2 kg until fracture. The third strongest design was the 2-slice configuration which withstood a maximum force of 245 kg before failure. However, limitations include the sample size, the selected material being PLA, and 100% infill. Based on the testing the most practical and optimal design is the 2-slice design (My Tech Fun, 2020).

### 2.3.3 FDM Threaded Nut Mechanical Strength

In a separate study by “My Tech Fun” horizontally orientated FDM threaded nuts performed better than vertically orientated FDM threaded nuts. The horizontally orientated M6 nut resisted a force generated by a 60.5 kg mass until failure. An interesting observation between both FDM screw testing and FDM nut testing is that FDM screws outperform FDM nuts by about 55%. Therefore, the nut can be assumed to fail before the screw (My Tech Fun, 2020). The strength of a screw joint and a nut is directly proportional to the number of threads engaged. Increasing the length of the threaded nut directly increases the load-bearing capacity (Roy Mech, 2023).

## 2.4 Drone Version 3

Drone version 3 addresses the key limitations of its predecessor, drone version 2. Notably, this iteration further reduces the overall weight. The drone version achieves this weight reduction by implementing two non-standard screw sizes: the Big Screw and Small Screw. While minor screw sizes for smaller attachments remain, further iterations address them. The validation process involved impact calculations and assessment of attachment joints for the drone legs. Notably, the repositioning of the legs closer to the main body reduced the moment induced on the arm attachment joint. Additionally, further validation was conducted through various testing of FDM components. The optimal wall clearance between two FDM components was obtained from reproducing a test inspired by a design presented by the YouTube channel “Maker’s Muse” (2017).

Figure 14 shows the FDM wall clearance test sample, which was manufactured with the following slicer settings

- Layer height: 0.2 mm

- Perimeter count: 3
- Material: HIPS

Further discussion on optimal slicing parameters will be provided in Chapter IV. This sample tests the minimal wall clearance between two walls inclined at a 60-degree overhang, starting at 0.1 mm and incrementally increasing by 0.1 mm increments up to 0.6 mm. The observed results of this test are as follows: a very tight wall clearance occurs at 0.3 mm, while 0.1 mm, and 0.2 mm exhibit perimeter fusion. Wall clearances of 0.4 mm, 0.5 mm, and 0.6 mm are considered loose.

Figure 14: Tolerance Test (0.1mm) 60°.

Another notable form of inspiration for certain design features stems from the YouTube channel “Slant3D”. Most notably, self-supporting structures, threaded holes, and snap fits (2023). These design features influenced the design language of various components within drone version 3, optimizing them for FDM.

In the development of drone version 3, design considerations and validation calculations proceeded in tandem. This would be the case for most of the drone designs as these validation calculations required finite element analysis (FEA) and FDM component testing. However, it is essential to recognize that this simultaneous approach poses limitations, as the current design is inherently constrained by the current understanding of the underlying theory behind the mechanical performance of FDM components.

Figure 15 shows an image of the complete assembly of drone version 3. Notably, this iteration represents a significant overhaul and complete redesign of drone version 2. Subsequent iterations, however, focused on further design and component optimization while maintaining a similar design.

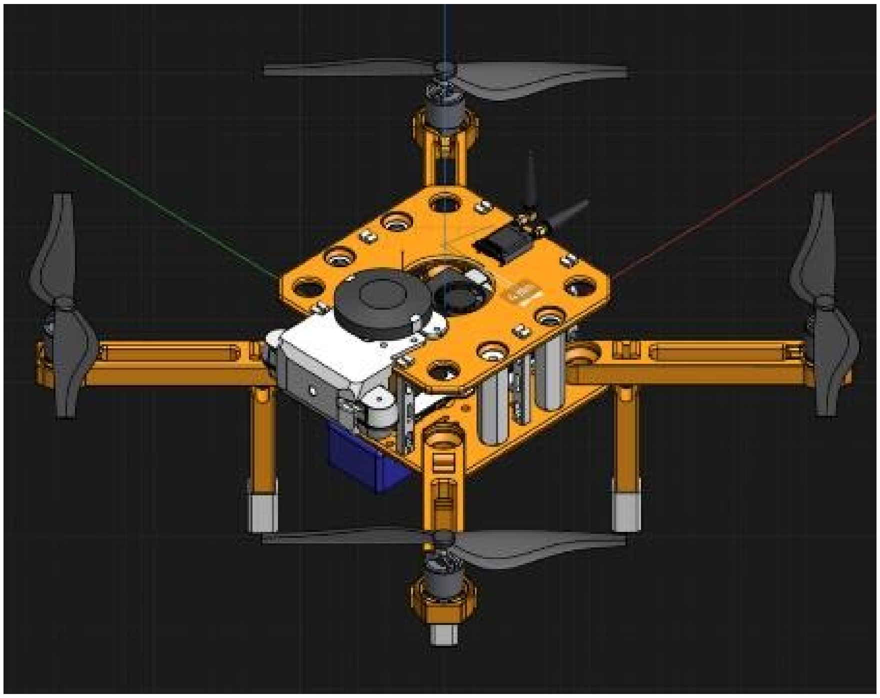

Figure 15: Drone Version 3.

## 2.5 Drone Version 4

Drone version 4 was developed with a refined understanding of impact calculations and validation. To enhance impact resistance, compliant mechanisms were integrated into the leg design. Additionally, a refined understanding of FDM allowed the production of functional standard screws and standoffs, eliminating the need for metal screws larger than M5.

Drone 4 marked a significant milestone as it was the first drone to undergo full manufacturing, assembly, and impact testing. Incorporating the spring-compliant mechanism ("Long Spring") onto the drone leg increased the impact resistance of drone version 4. Additionally, further weight reduction was achieved by replacing the Big Screw with the Small Screw, the Small Screw standoff and attachment for an M10 screw-based design, and the introduction of FDM M5 screws and standoffs.

Figure 16 shows the long spring design integrated into the legs of drone version 4. The spring's stiffness characteristics will be explored in greater detail in Chapter III. Another design alteration between drone version 3 and drone version 4 is the removal of the mount for the D455 Logitech. After careful consideration of the drone assembly's objectives, a decision was made regarding the effective camera range. The range of motion for the camera was set at 90° to capture images below and in front of the assembly. While the design of a mount with a 90° range of motion would require further development and integration into the electrical configuration of the drone system, this study focuses on the structural integrity and robustness of the drone under flight and impact loading conditions. Consequently, the design of this mount is beyond the scope of this study. Instead, mounting holes were incorporated into the top board to allow for flexibility in further implementations.

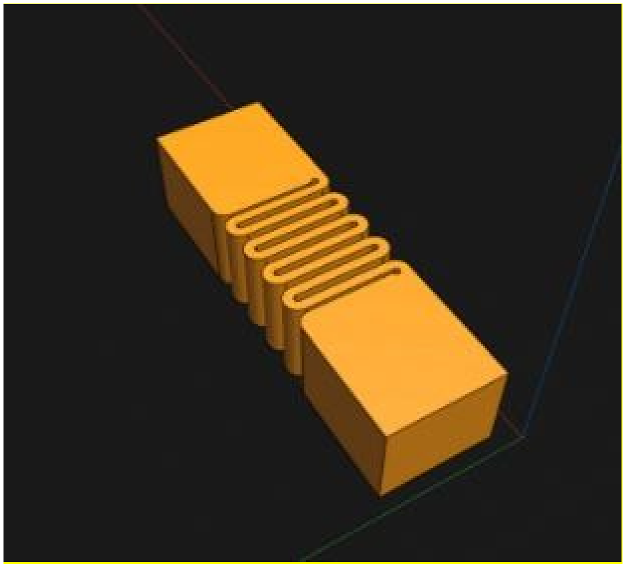

Figure 16: Long Spring.

Figure 17 shows drone version 4. The results of impact testing of drone version 4 revealed the impact resistance limitations of this design, which are further discussed in Chapter VI.

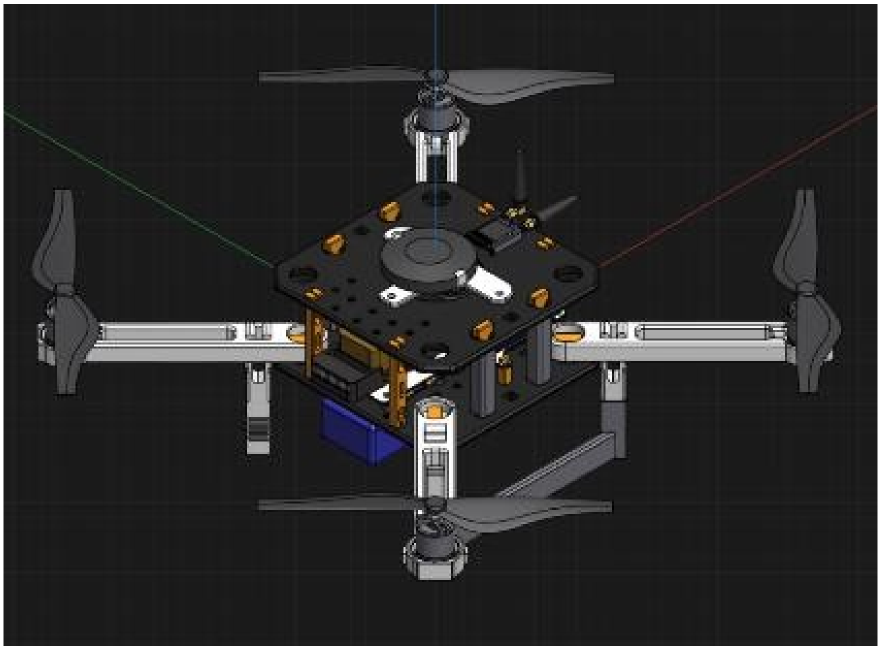

Figure 17: Drone Version 4.

## 2.6 Drone Version 5

Drone version 5 rectified the asymmetrical error present in the earlier drone designs, and directly addressed its limitations. During assembly, impact testing, and manufacturing of drone version 4 many limitations became apparent. These limitations include component warping, significant post-processing, complicated assembly procedures, multiple degrees of freedom on fixtures, and low-impact resistance. To decrease the complexity of assembly and limit the degrees of freedom drone version 5 incorporated slot designs for the new screw joints, ensuring simple secure placement. Additionally, the manufacturing process was optimized by utilizing PETG filament for the drone components as opposed to HIPS. Furthermore, drone version 5 improves the impact resistance by increasing the thickness of failure points, optimizing the fixture points, and implementing a better compliant spring design. This new spring, manufactured with

TPU, is more robust and resists lateral deformation. Figure 18 shows the design of the new compliant mechanism, TPU spring single, implemented in drone version 5.

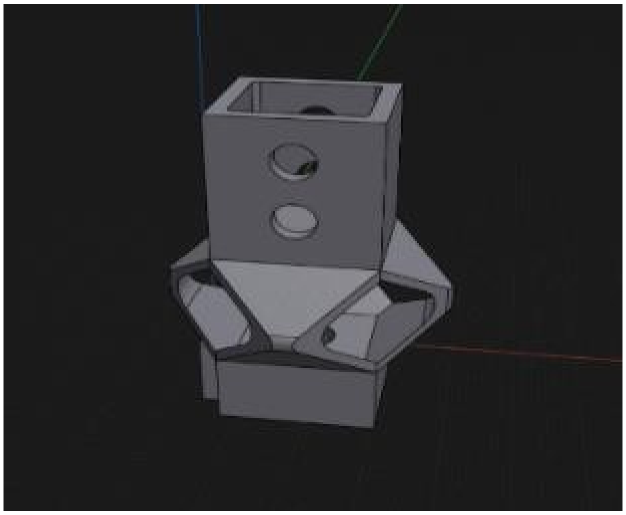

Figure 18: TPU Spring Single

Figure 19 shows the complete structural assembly of drone version 5. To better analyze and test the strength of 3D printed fixtures the screw sizes for drone version 5 were all switched to M10 or M5 screw variants. Although drone version 5 improves upon the impact resistance of drone version 4, the limitations of drone version 5 were identified during impact. These limitations are further discussed in Chapter VI.

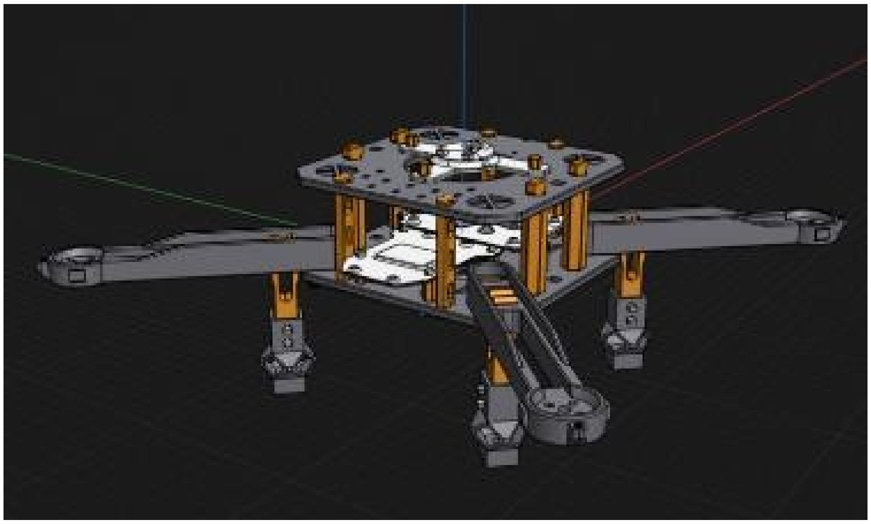

Figure 19: Drone Version 5.

## 2.7 Drone Version 6

In response to the limitations observed during impact testing on drone version 5, drone version 6 underwent specific design improvements to rectify these limitations. These modifications primarily focused on increasing the thickness of the bottom board and refining the compliant TPU spring. Altering the thickness of the bottom board required the alteration of all the attachment fixtures. Certain manufacturing parameters for the M10 screws were adjusted to address previous strength limitations discussed in Chapter VI and Chapter VI. Additionally, the design of the M5 screws were modified to enhance thread engagement for subassemblies. After further analysis and research, the decision was made to manufacture screw components with PETG, due to its superior creep resistance and robust properties (Davis, 2023; MakeItFrom, 2023; My Tech Fun, 2021).

Figure 20 shows the complete assembly of drone version 6. Drone version 6 was able to meet the stringent impact resistance required to fulfill the project objectives. No further drone versions were developed in this study.

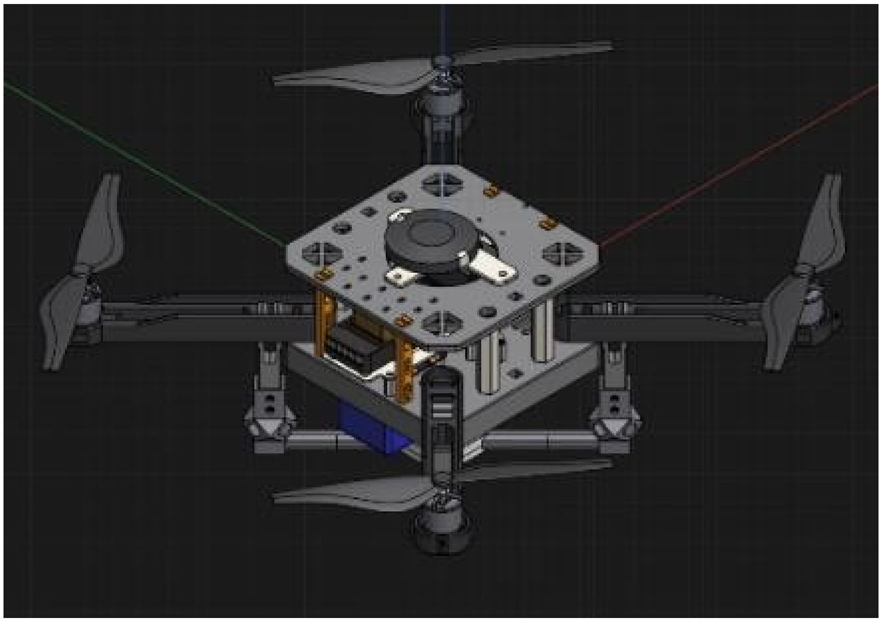

Figure 20: Drone Version 6.

## 2.8 Design Conclusions

### 2.8.1 Problem Statement

The design of a quadcopter drone relies on several critical factors including loading conditions, fixtures/attachment joints, and manufacturing method. One primary loading condition on a drone assembly is thrust loading on the arms and the force applied to the arms and legs during an impact event. When designing a drone assembly or any design for FDM, it is important to know the limitations of the manufacturing method. A proficient engineer is well-versed in the constraints specific to the manufacturing method.

### 2.8.2 Tolerances

For FDM components, tolerance plays a significant role in achieving proper component interactions. Properly assessing the component tolerances required to achieve a specific intended wall clearance is critical when designing and manufacturing part assemblies. Each FDM machine has different tolerances which can be tested by reproducing test components (Maker's Muse, 2017).

### 2.8.3 Screw Orientation

The optimal design for horizontal FDM screws is the 2-slice design for the M10 and M6 (My Tech Fun, 2020). The optimal FDM orientation for threaded nuts is horizontally flat on the print bed (My Tech Fun, 2020). CAD files for standard screw and nut sizes for both metric and ISO can be obtained from McMaster.

### 2.8.4 Compliant Mechanisms

When connecting or fixing two FDM components, consider employing compliant mechanisms as a reliable connection method (Slant 3D, 2023). Compliant mechanisms can be implemented to absorb energy produced by impact loading cases and design connection joints. Lastly, addressing horizontal overhangs involves implementing strategic support placement such as chamfering the lower surface, designing optimally positioned supports, or bridging (Macro 3D Prints, 2023; Slant 3D, 2023).

# CHAPTER III

# CALCULATIONS AND FINITE ELEMENT ANALYSIS

## 3.1 Assumptions

In designing and optimizing the robustness of the drone assembly, several assumptions about the reactions and structures were made. These assumptions aided in cross-validating Finite Element Analysis (FEA) verification with those obtained through an analytical approach. The following assumptions were made: (1) all complex bodies can be represented as a combination of simpler geometries, (2) all component structures are homogenous solid bodies, (3) all attachment joints are fixed or supported connection points, (4) the drag force component can be neglected for low operational speeds required to capture sensor data properly, and (5) all loading cases can be represented by point loads. Throughout the development of an analytical approach, the metric international system of units was employed. Consequently, all the forces were in Newtons, all measurements and dimensions were in meters/millimeters, all stress values were in Pascals/Megapascals, all moments and torques were in Newtons meter, and all displacements were in meters/millimeters.

## 3.2 Weight, Cost, and Print Time Calculation

Considerable values of interest when designing an FDM drone assembly include the numerical values for the total weight of the drone assembly, the total cost of the drone assembly, and the total print time

$$w = \Sigma w_c + \Sigma w_L \tag{2}$$

$$\text{Total Print Time} = \Sigma t_i \tag{3}$$

$$\text{FDM cost} = \Sigma(m_i \cdot c_i) \tag{4}$$

The total weight of the drone assembly (w) was obtained by employing Equation 2. Equation 2 shows the total weight (w) as the sum between the summation of the FDM components ($w_c$) and the summation of the non-FDM components ($w_L$). The total print time of the drone assembly was obtained by employing Equation 3, which is simply the summation of each print time for the FDM components ($t_i$). The FDM cost of the drone assembly was obtained by employing Equation 4, which is the FDM cost as the summation of the product between the mass of each component in grams ($m_i$) and the cost per gram of the material ($c_i$). The total weight of the assembly for Drone Version 6 is 3.5 kg, the total cost of the manufactured components is 24 USD, and the total print time is 5 days.

## 3.3 Weight Percentage

When designing a drone, weight is a major limiting factor in the flight duration of a drone. Identifying the components that contribute most to the overall weight is crucial for optimizing a drone assembly. The weight mass percentage of each component ($P_i$) can be obtained using the following equation.

$$P_i = \frac{m_i}{m_T} \cdot 100\% \tag{5}$$

Where $P_i$ is the quotient of the mass of each component ($m_i$), and the total mass of the drone assembly ($m_T$).

Figure 21 shows the weight percentage contributed by each external component to the total weight. The Bottom Board and the Arms significantly contribute to the total weight. The Bottom Board accounts for 11.42% of the total drone weight, and the Arms accounts for 9.32%. The observations from Figure 21 offer useful insight into where to reduce the drone weight.

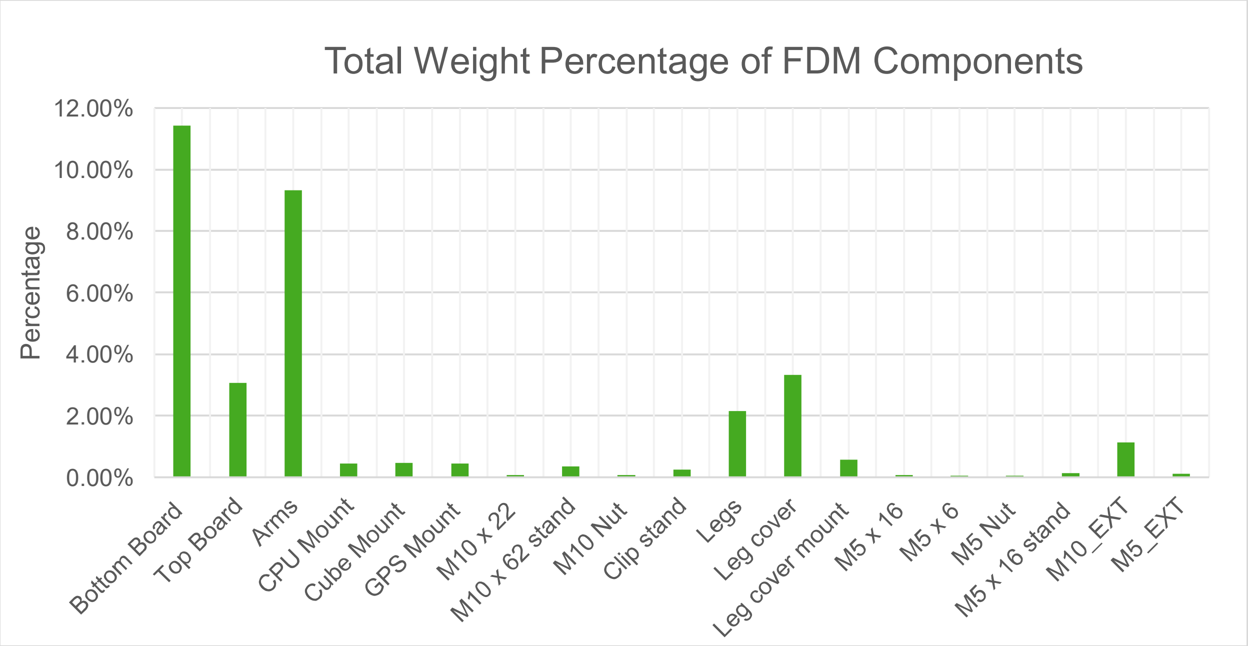

Figure 21: Total Weight Percentage of FDM Components.

Figure 22 shows the weight percentage contributed by each external component to the total weight. Notably, the Battery and Camera significantly contribute to the total weight. The Battery accounts for 17.91% of the total drone weight, and the Camera accounts for 9.32%—the observations from Figure 22 offer useful insight into where to reduce the drone weight.

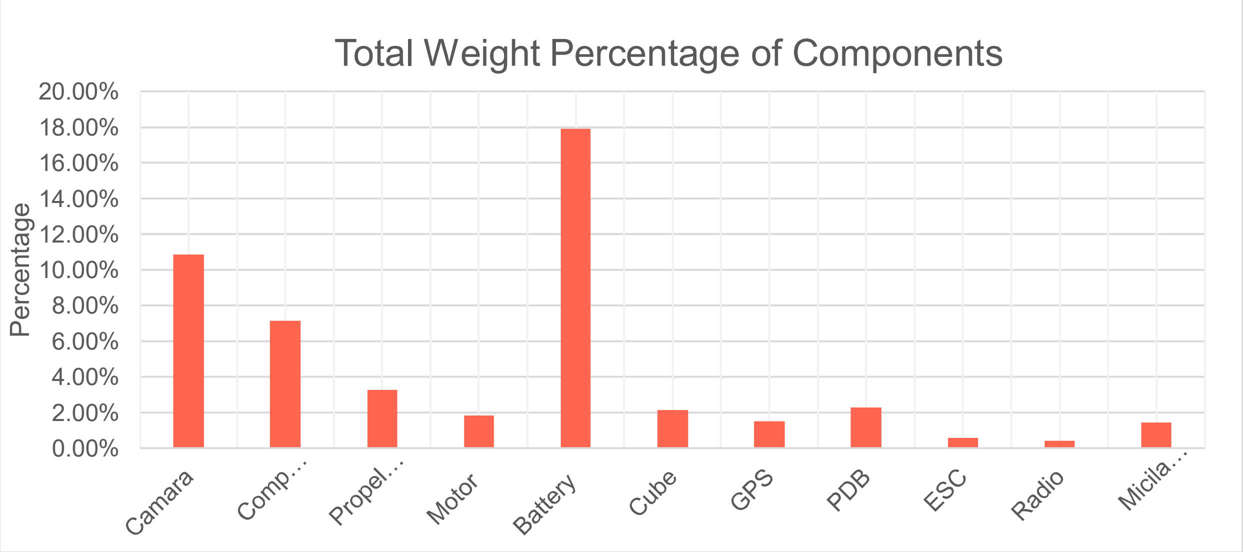

Figure 22: Total Weight Percentage of Components.

### 3.4 Center of Mass Calculations

When designing a drone assembly, the location of the center of mass is a key input for the flight controller to function properly and support stable flight operations. The center of mass for a three-dimensional object is denoted by the center distance ($d_c$) of each respective coordinate (x, y, z). Subsequently, the center of mass for the drone FDM components and the center of mass for the entire drone assembly are different. The absolute center of mass ($c_d$) is obtained but utilizing Equation 6. The subscript  d represents the coordinates in (x, y, z)

$$d_c = \frac{\sum m_i \cdot d_i}{\sum m_i} \tag{6}$$

$$\mathrm{c_d} = \frac{d_c \cdot m_d + \sum m_i \cdot d_i}{m_d + \sum m_i} \tag{7}$$

Equation 6 expresses $d_c$ to be a quotient. The numerator consists of the summation of the product between the mass of each component ($m_i$) and the distance between the geometric center ($d_i$). The denominator consists of the summation of $m_i$. Equation 7 expresses cd to be a quotient. The numerator consists of the sum of the product of $d_c$ and the mass of the drone ($m_d$) and the summation of the product of $m_i$ and $d_i$. The denominator consists of the sum of $m_d$ with the summation of $m_{i.}$

The results obtained from Equation 6 are as follows:

- X – axis = 0.23 mm
- Y – axis = 0.00 mm
- Z – axis = 1.40 mm

The results obtained from Equation 7 are as follows:

- X – axis = 12.69 mm
- Y – axis = 0.00 mm
- Z – axis = 13.67 mm

This approach assumes that the center of mass for each component is located at the center of geometry. This is not necessarily the case for each component and would require further research to obtain the location of the geometric center for each component and plug those values into Equation 6 and Equation 7.

### 3.5 Climb, Roll, Pitch, and Hover Calculations

For a drone assembly, certain flight maneuvers are essential for the end operational use case. To understand the required thrust ($F_T$) for these maneuvers the following free-body-diagrams (FBD) and equations were utilized for climb, roll, pitch, and hover maneuvers (Allain, 2019; EngineersEscape, 2019). Figure 23 represents the FBD that was developed for the climb maneuver.

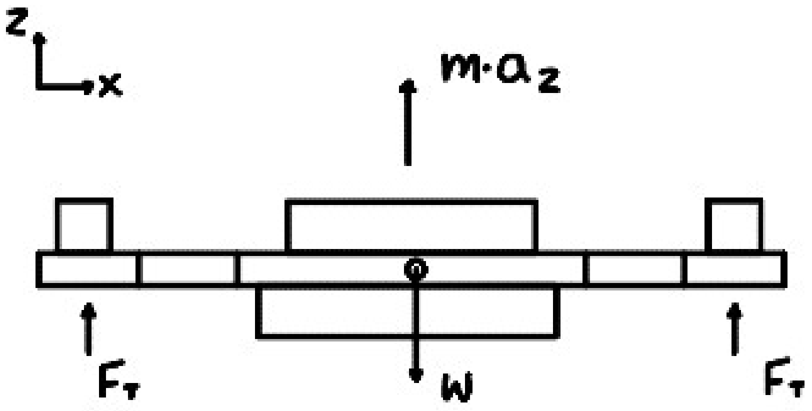

Figure 23: Climb FBD.

$$F_T = 0.25 \cdot w + \frac{0.25 \cdot w \cdot a_z}{g} \tag{8}$$

Equation 8 represents $F_T$ as the sum of 25% of the weight (w) and a quotient. The numerator of the quotient is the product of 25% of w and the acceleration in the z-axis ($a_z$). The denominator is the gravitational acceleration constant (g). The required $F_T$ to achieve a desired climb acceleration of 4 $m/s^2$ in the z-axis is equivalent to a mass of 1.23 kg. This $F_T$ is 92% of the maximum available thrust for the Holybro brushless motors making the desired input climb acceleration a viable input (Holybro, 2023). Figure 24 represents the FBD for the roll and pitch maneuvers. These maneuvers require the same calculations because the drone assembly is nearly symmetrical.

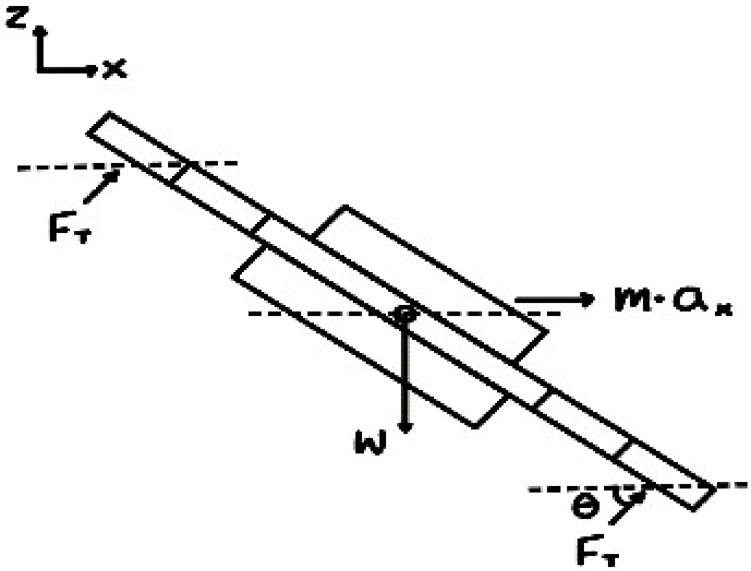

Figure 24: Roll and Pitch FBD.

$$F_T = \frac{w}{4 \cdot \sin\theta} \tag{9}$$

$$a_x = \frac{4 \cdot F_T \cdot \cos\theta \cdot g}{w} \tag{10}$$

Equation 9 represents the thrust force ($F_T$) as the quotient between the total weight (w) and the product of four times the sin of an angle (θ). Equation 10 represents the acceleration in the x-axis ($a_x$) as a quotient. The numerator is a product of four times $F_T$, cos θ, and the gravitational acceleration constant (g). The denominator is comprised of w. The results of Equation 9 and Equation 10 for an input angle of 45° are a force equivalent to a mass of 1.23 kg for $F_T$, and 9.78 m/s2 for $a_x$ respectively. This thrust is 92% of the maximum available thrust for the Holybro brushless motors making the input angle a viable input (Holybro, 2023). Figure 25 represents the FBD of the drone for the hovering maneuver.

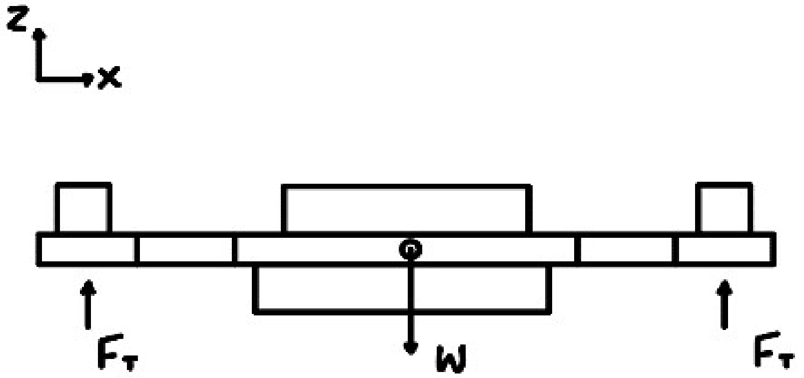

Figure 25: Hovering FBD.

$$F_T = 0.25 \cdot w \tag{11}$$

Equation 11 represents the thrust force ($F_T$) as 25% of the total weight (w). This is because the drone weight is distributed between the four motors. The result from Equation 11 is force equivalent to a mass of 0.87 kg for $F_T$. This is 65% of the maximum available thrust for Holybro brushless motors making the total weight a viable input (Holybro, 2023).

### 3.6 Flight Time Calculations

Calculating the flight time of a drone is essential for understanding the capabilities to meet project objectives. To obtain the flight time for the drone assembly the following equation were used (Szyk, 2023).

$$AAD = \frac{w \cdot P}{V} \tag{12}$$

$$\text{Flight Time} = (\text{Capacity} \cdot \text{Discharge})/\ \text{AAD} \tag{13}$$

Equation 12 represents the average amp drawn AAD as a quotient. The numerator is a product between the total weight of the drone (w) and the power consumption rate per kg (P). The denominator is the nominal voltage of the battery (V). Utilizing the manufacturer's flight time data and drone weight specifications, P was obtained. Equation 13 represents the Flight Time as a quotient. The numerator is the product between the battery capacity (Capacity) and the allowable percentage that can be discharged (Discharge), and the denominator is the average amp draw (AAD). Imputting the P of the drone assembly into Equation 12 and Equation 13 yielded a 7-minute flight time for the drone assembly. This flight time does not meet the project objective as it is desired to have a flight time of at least 18 minutes. From Equation 12 the main limiting factor is the drone's weight. To better visualize this issue a plot was generated to show the drone's weight against the flight time.

Figure 26 shows the relation between the drone weight and flight time. The red marker indicates the weight of the non-FDM drone components. The green line indicates the total weight of the drone assembly on the manufacturer's website (Holybro, 2023). Some significant observations from Figure 26 are the steep slope between 2250 g and 1200 g, whereas between 3500 g and 2300 g, the slope is shallow. The slope of Figure 26 represents the rate at which the weight of the assembly affects the flight time performance. To achieve a substantial increase in the flight time of the drone assembly significant weight reductions need to be implemented. This topic will be further discussed in Chapter VII.

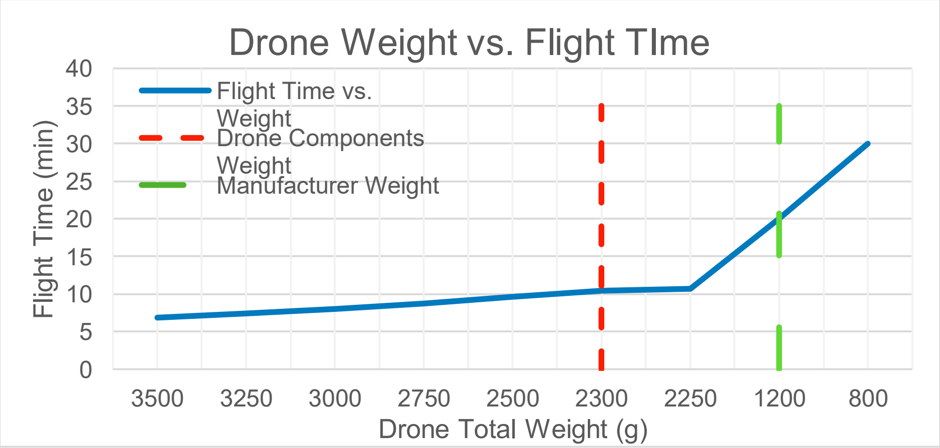

Figure 26: Drone Weight vs. Flight Time.

### 3.7 Body Clips and Leg Calculations

To validate the design and function of the attachment connection joints for the Body Clips and the Leg designs FBD was used to obtain analytical solutions. These solutions would be used to validate the FEA results and validate the design of the components. Figure 27 (left) shows the FBD of a cantilever beam that represents the Body Clip design and Leg design loading case. Figure 27 (right) shows the rectangular cross-sectional area.

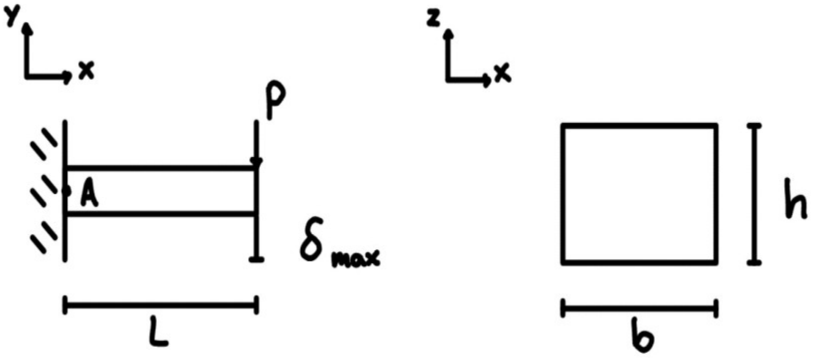

Figure 27: Body Clip and Leg FBD (left) Body Clip and Leg Cross-Section (right).

$$P = \frac{3 \cdot \delta \cdot E \cdot I}{L^3} \tag{14}$$

$$I = \frac{b \cdot h^3}{12} \tag{15}$$

$$\sigma_{\max} = \frac{P \cdot L \cdot \left(\frac{h}{2}\right)}{I} \tag{16}$$

Equation 16 represents the maximum stress ($\sigma_{max}$) where the numerator is a product between the applied load (P), the length of the beam (L), and half the height (h), and the denominator is the mass moment of inertia (I). Equation 15 gives the I to be the product of the length of the base (b) and the height (h) cubed divided by 12 for a rectangular cross-section. Equation 14 gives the applied load P as three times the beam deflection (δ), the elastic modulus of the material (E), and I divided by the length of the beam L cubed. The maximum stress value obtained from Equation 16 for the Body Clip design was 18.52 MPa. This value is lower than HIPS's yield strength, making it a practical design (MakeItFrom, 2020). The maximum stress value obtained from Equation 16 for the Leg design was 20.16 MPa. This value is lower than the yield strength for PETG making it a practical design (MakeItFrom, 2020). When designing compliant mechanisms such as these two designs the fatigue life and number of cycles before failure are usually required to validate the design. Unfortunately, certain variables such as the component material's endurance limit are required to validate components for fatigue accurately. FDM is a new form of manufacturing and these variables have not been properly investigated, thus making it outside the scopeof this study.

## 3.8 Body Clip and Leg FEA

To perform a static FEA for the BC and the Leg the following steps were conducted in Fusion 360.

1. Import CAD models
    1.1. Imported model file format should be IGES
    1.2. Click the "Design" button and select "Simulation"

    1.3. In the ensuing pop-up, select “Static Analysis”

2. Material selection
    2.1. Select the appropriate material for component analysis
    2.2. Note that Fusion 360’s material library lacks profiles for PETG, HIPS, and TPU
    2.3. Custom material profiles were created for PETG, HIPS, and TPU utilizing the material properties obtained in Chapter I
3. Fixed geometry and load application
    3.1. Apply fixed geometry that best represents the component application
    3.2. For BC and Leg, the fixed geometry was the bottom face
    3.3. Apply the load obtained from Equation 14
    3.4. Make sure the load is facing the correct orientation and applied in the correct geometry
4. Mesh generation
    4.1. Create a mesh for simulation
    4.2. The mesh size for this simulation is 3%
    4.3. A convergence analysis was conducted between 2%, 3%, and 4% mesh size
5. Solving and analysis
    5.1. Once the green check mark appears on the clipboard icon, click “Solve” to run the simulation
    5.2. Analyze the results and compare them with the analytical solution

Figure 28 shows the setting popup for changing the mesh size in Fusion 360. The mesh size selected in Figure 28 is 3%.

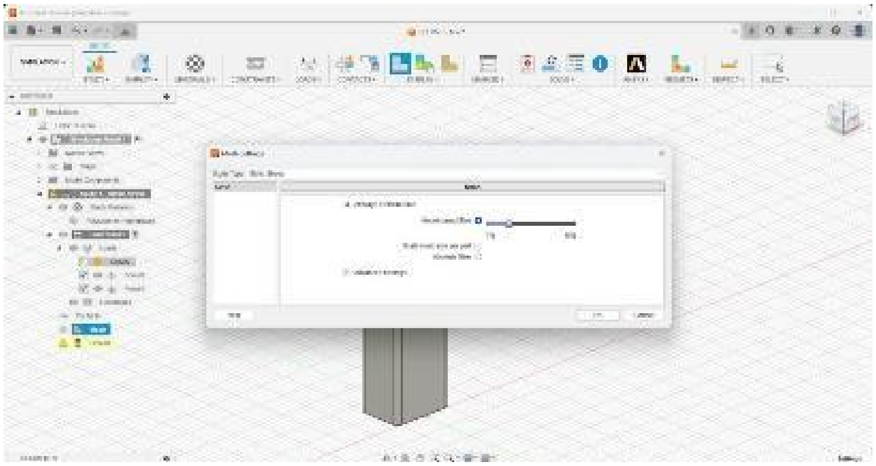

Figure 28: Body Clip with 3% Mesh Size.

Figure 29 shows the maximum FEA displacement of the Body Clip as 1.451 mm.

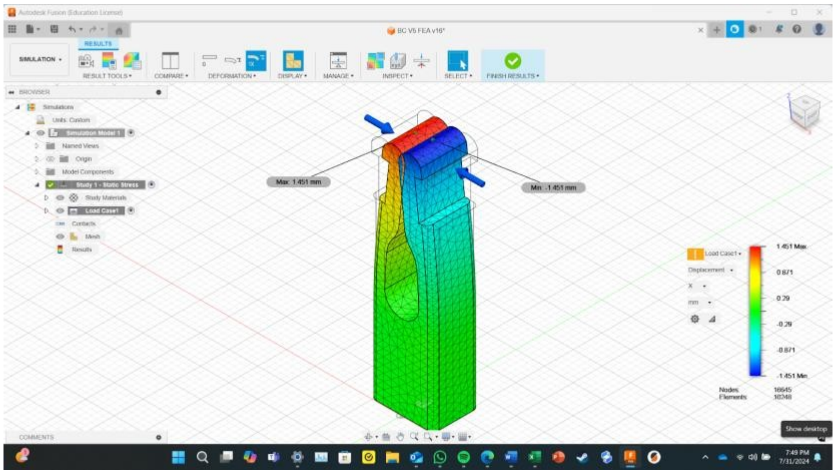

Figure 29: Displacement Results (mm) for Body Clip FEA (3% Mesh Size).

Figure 30 shows the maximum and minimum FEA stress of Body Clip as 17.342, and -20.35 MPa respectively.

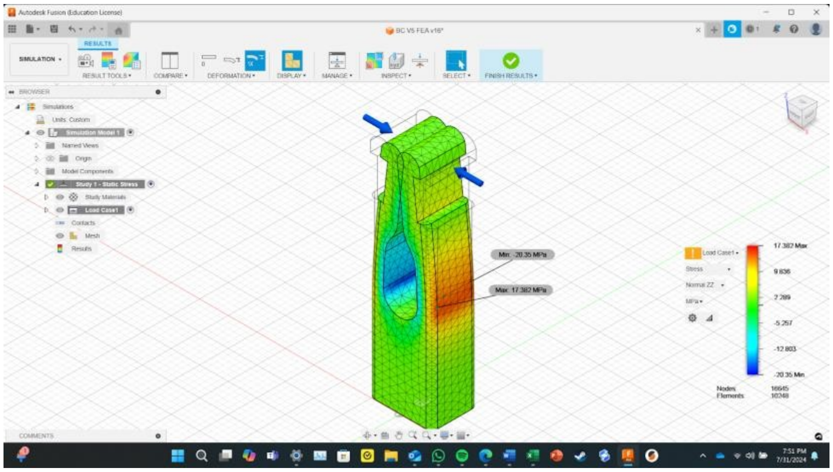

Figure 30: Stress Results (MPa) for Body Clip FEA (3% Mesh Size).

Figure 31 shows the setting popup for changing the mesh size in Fusion 360. The mesh size selected in Figure 31 is 4%.

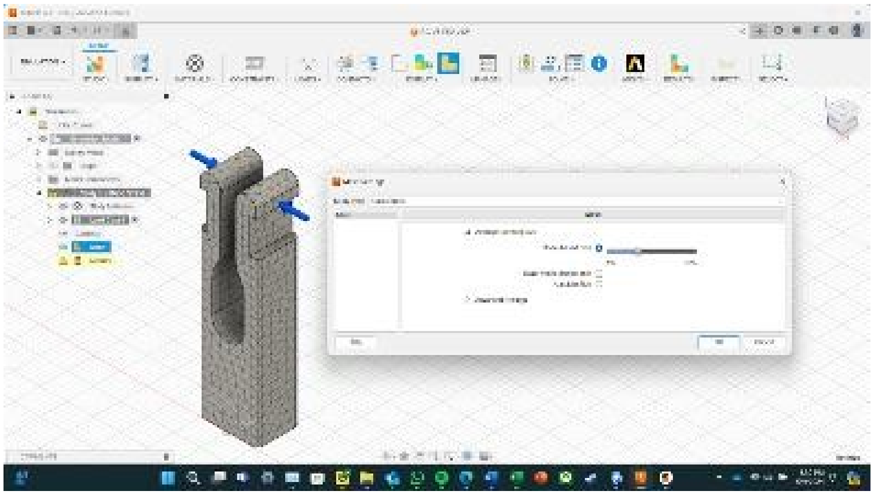

Figure 31: Body Clip with 4% Mesh Size.

Figure 32 shows the maximum FEA displacement of the Body Clip as 1.455 mm.

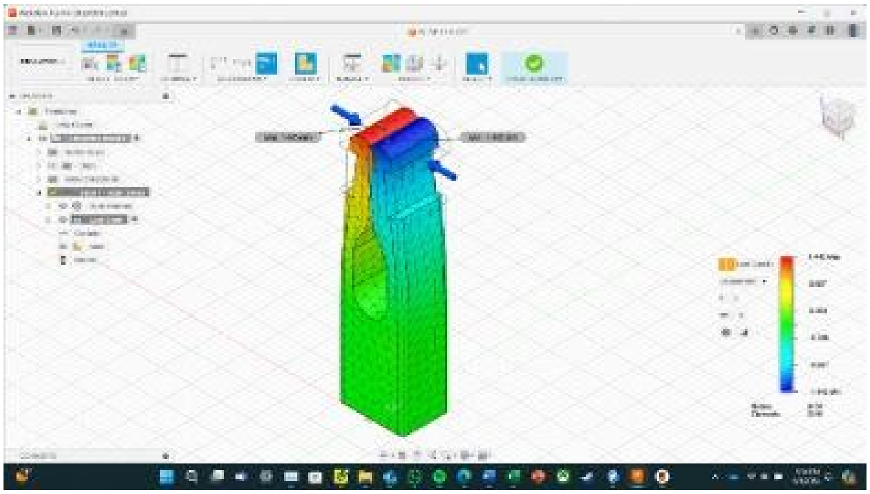

Figure 32: Displacement Results (mm) for Body Clip FEA (4% Mesh Size).

Figure 33 shows the maximum and minimum FEA stress of the Body Clip as 17.088, and -20.735 MPa respectively.

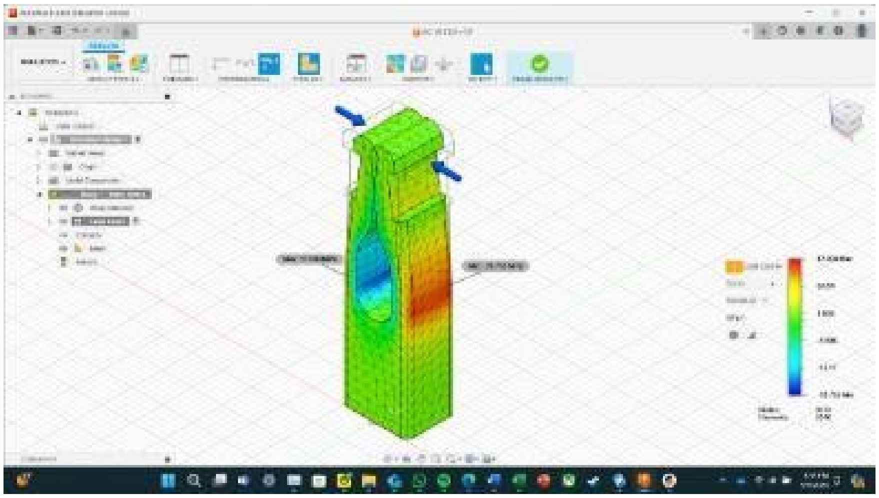

Figure 33: Stress Results (MPa) for Body Clip FEA (4% Mesh Size).

Figure 34 shows the setting popup for changing the mesh size in Fusion 360. The mesh size selected in Figure 34 is 2%.

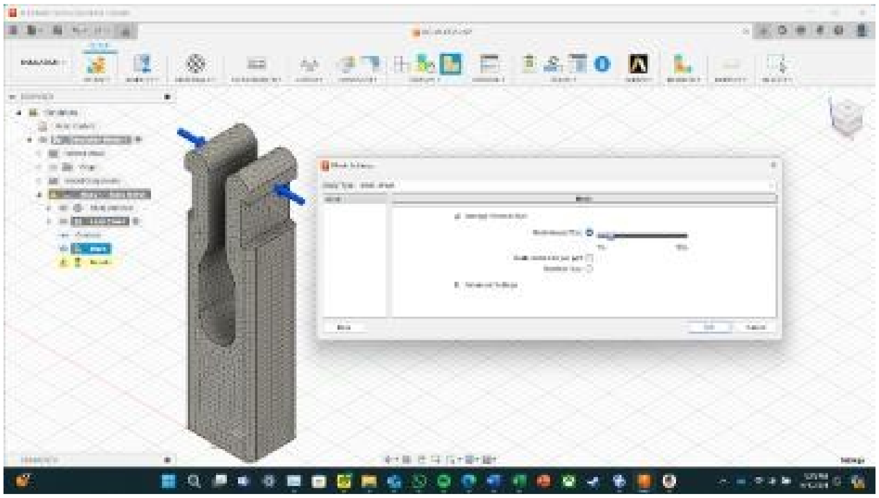

Figure 34: Body Clip with 2% Mesh Size.

Figure 35 shows the maximum FEA displacement of the Body Clip as 1.454 mm.

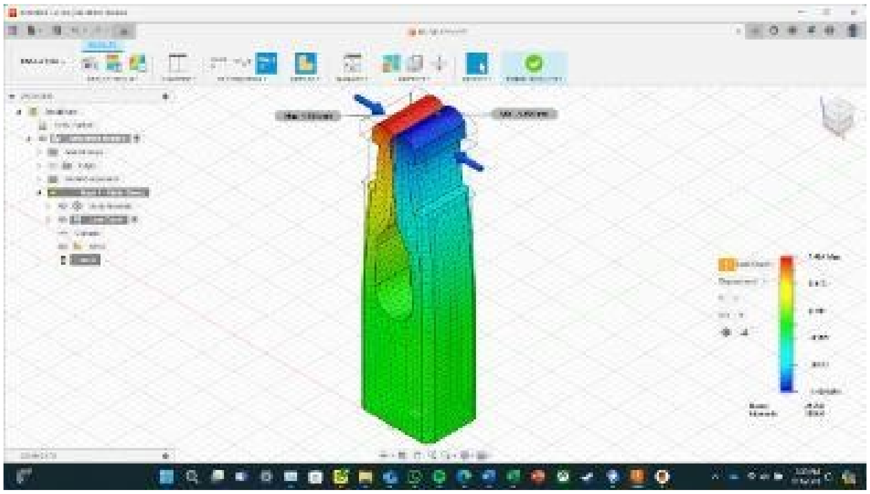

Figure 35: Displacement Results (mm) for Body Clip FEA (2% Mesh Size).

Figure 36 shows the maximum and minimum FEA stress of Body Clip as 16.942, and -20.965 MPa respectively.

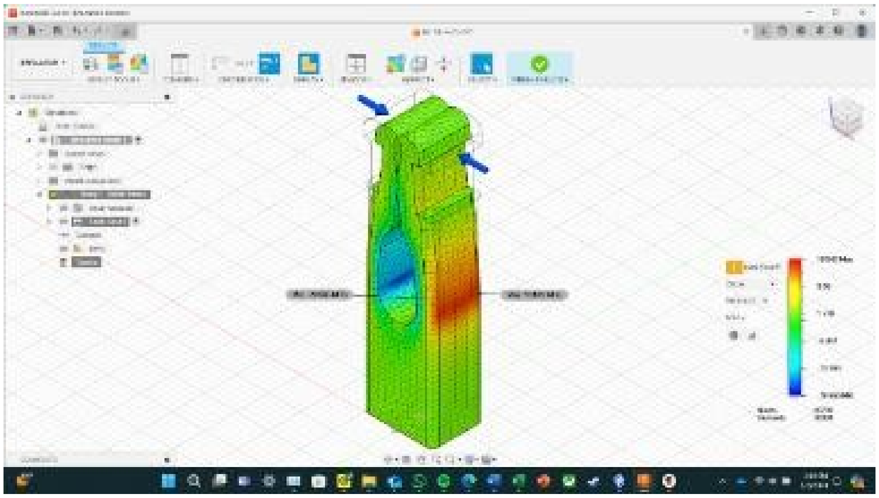

Figure 36: Stress Results (MPa) for Body Clip FEA (2% Mesh Size).

Figure 37 shows the setting popup for modifying the mesh size in Fusion 360. The mesh size selected in Figure 37 is 3%.

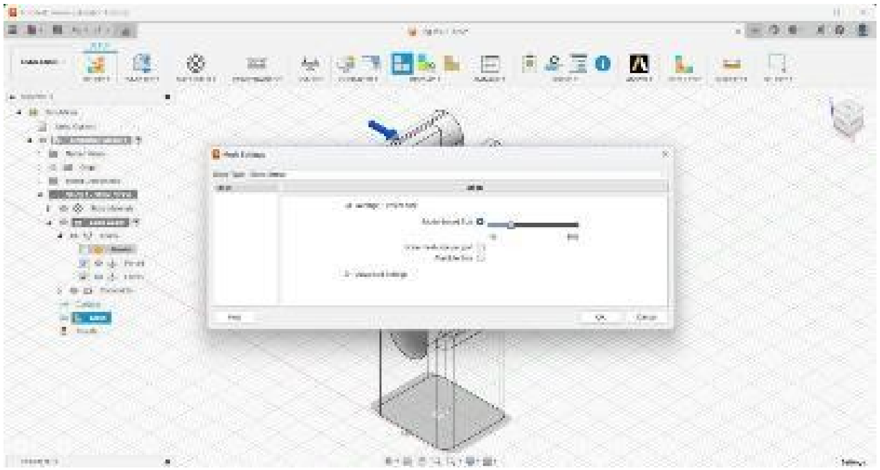

Figure 37: Leg FEA with 3% Mesh Size.

Figure 38 shows the maximum FEA displacement of the Leg as 1.961mm.

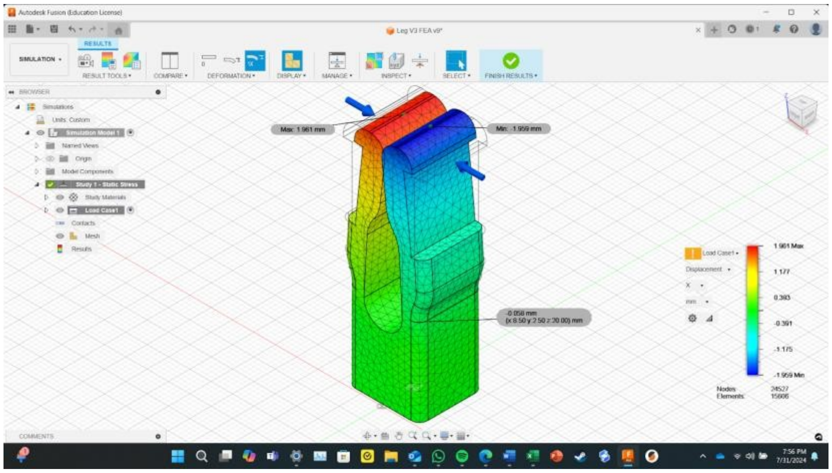

Figure 38: Displacement Results (mm) for Leg FEA (3% Mesh Size).

Figure 39 shows the maximum and minimum FEA stress of the Leg as 24.144, and -23.541 MPa respectively. Additionally, the stress at the point of interest is shown to be 19.82 MPa.

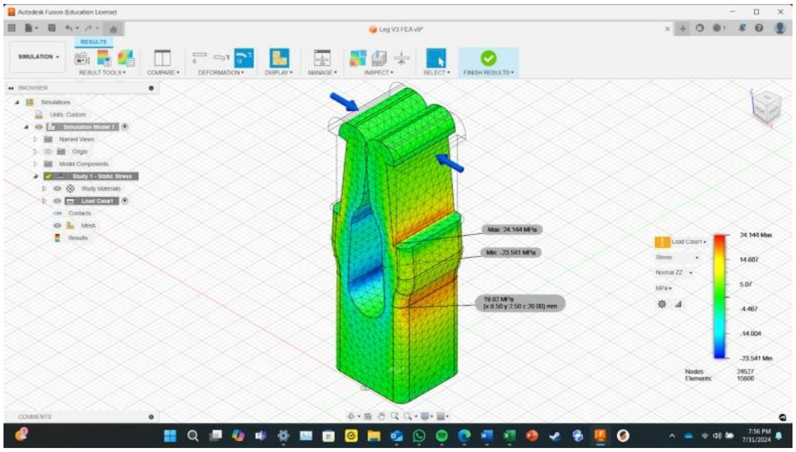

Figure 39: Stress Results (MPa) for Leg FEA (3% Mesh Size).

Figure 40 shows the setting popup for modifying the mesh size in Fusion 360. The mesh size selected in Figure 40 is 4%.

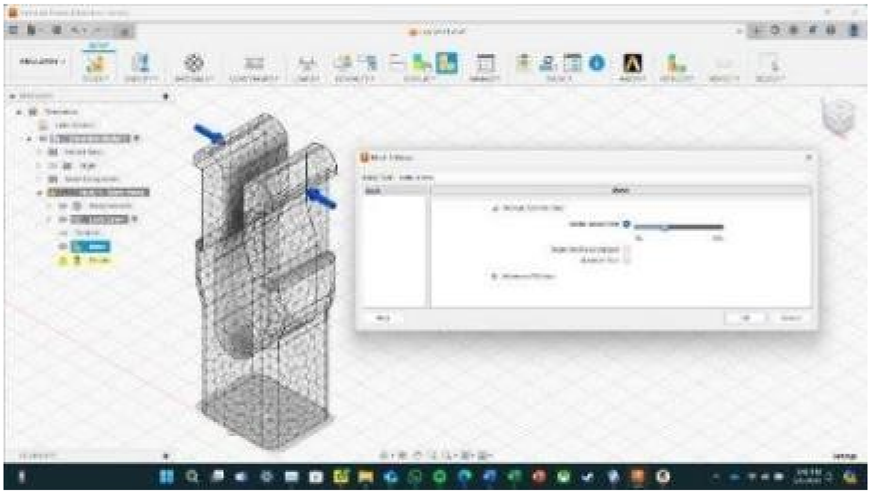

Figure 40: Leg FEA with 4% Mesh Size.

Figure 41 shows the maximum FEA displacement of the Leg as 1.943mm.

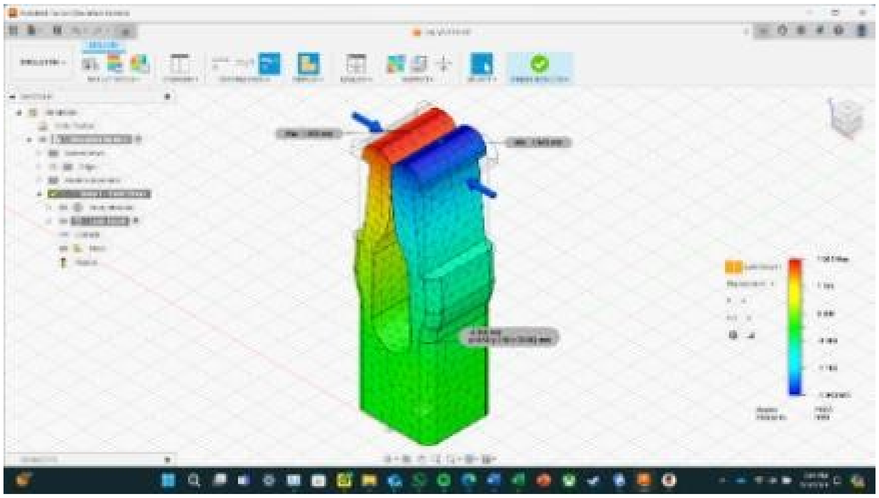

Figure 41: Displacement Results (mm) for Leg FEA (4% Mesh Size).

Figure 42 shows the maximum and minimum FEA stress of the Leg as 22.20, and -23.58 MPa respectively. Additionally, the stress at the point of interest is shown to be 19.838 MPa.

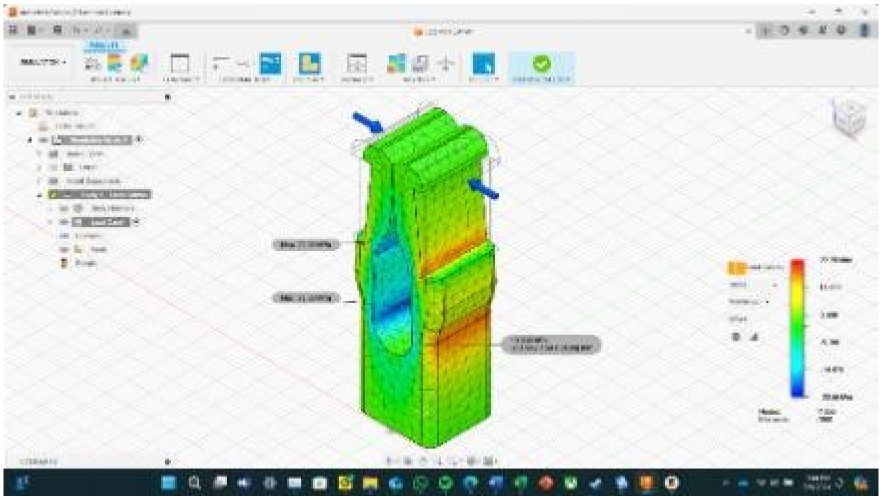

Figure 42: Stress Results (MPa) for Leg FEA (4% Mesh Size).

Figure 43 shows the setting popup for modifying the mesh size in Fusion 360. The mesh size selected in Figure 43 is 2%.

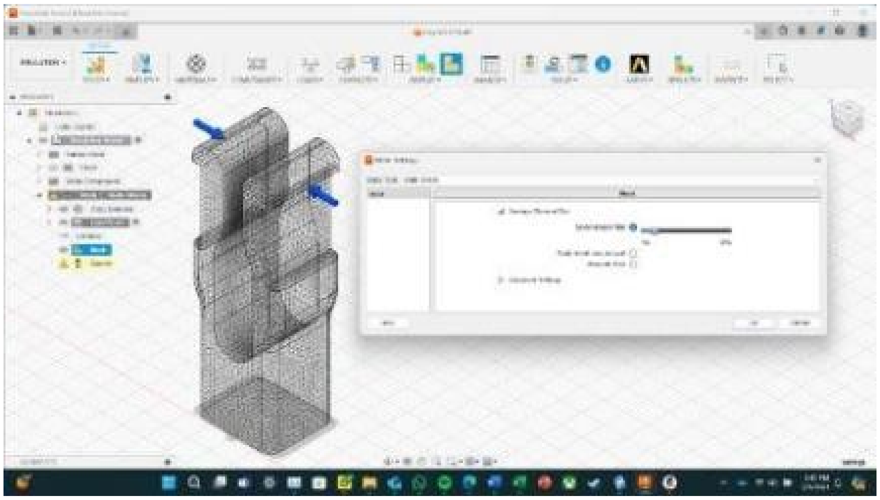

Figure 43: Leg FEA with 2% Mesh Size.

Figure 44 shows the maximum FEA displacement of the Leg as 1.972 mm.

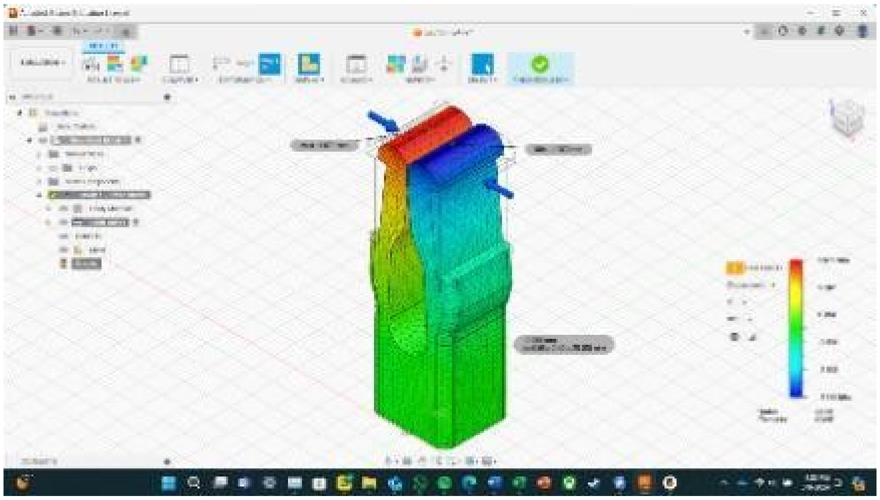

Figure 44: Displacement Results (mm) for Leg FEA (2% Mesh Size).

Figure 45 shows the maximum and minimum FEA stress of the Leg as 26.169 and -23.513 MPa respectively. Additionally, the stress at the point of interest is shown to be 19.79 MPa.

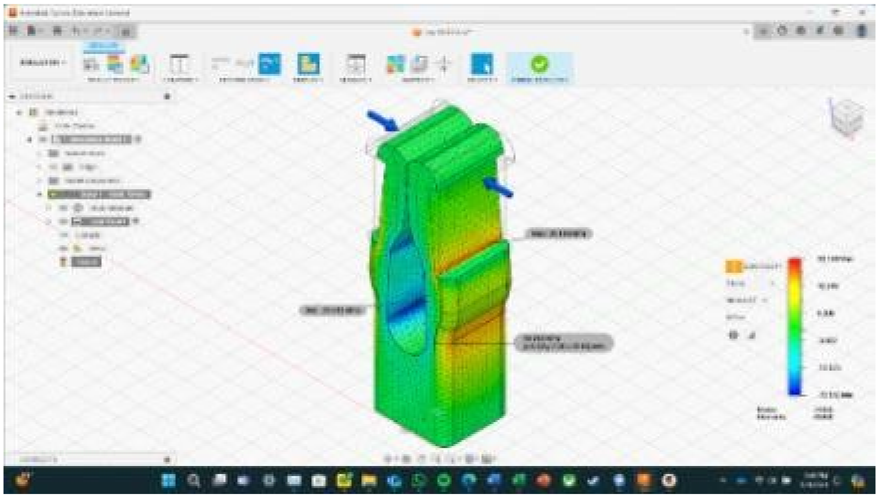

Figure 45: Stress Results (MPa) for Leg FEA (2% Mesh Size).

The results of the FEA were compared with the results obtained from the analytical solution (for a simplified model) utilizing the following equation, which gives the percentage error between the two results.

$$error = \mathrm{abs}\left(\frac{Cal - FEA}{Cal}\right) \cdot 100\% \tag{17}$$

Equation 17 represents the percent error between the analytical solution (Cal) and the numerical solution (FEA) with the basis of the analytical solution (Cal).

$$error = \mathrm{abs}\left(\frac{\mathrm{b} - \mathrm{n}}{b}\right) \cdot 100\% \tag{18}$$

Equation 18 represents the percent error between the base mesh size (b) and the utilized mesh size (n). For this study, b was 3% and the n utilized were both 2% and 4%.

The percentage error assessment for Body Clip utilizing Equation 17 yielded the following results for deflection the percent error was 16%, for the stress at the point of interest the percent error was 1.25%. The convergence analysis for the Body Clip showed that changing the mesh size by ±1% from the base 3% mesh size yielded less than 2.52% change in the results for the stress at the point of interest and less than 0.3% for deflection. Therefore a 3% mesh size is adequate for obtaining the stress and deflection values for Body Clip, and the FEA results for the stress at the point of interest align well with the analytical solution of a simplified model. However, this is not the maximum stress in the FEA which is 20.35 MPa. This value exceeds HIPS's yield strength, making the BC design an unviable option for HIPS. In contrast, PETG has a UTS strength that is much higher than HIPS and therefore is a more adequate material. Additionally, the maximum deflection in the FEA exceeds the design's allowable limit of 1.25mm. Reasons for this error may include the lack of showing potential collisions between solid bodies in Fusion 360.

The percentage error assessment for Leg utilizing Equation 17 yielded the following results for deflection the percent error was 2%, for the stress at the point of interest the percent error was 10.64%. The convergence analysis for the Leg showed that changing the mesh size by ±1% from the base 3% mesh size yielded less than 0.28% change in the results for the stress at the point of interest and less than 0.56% for deflection. Therefore a 3% mesh size is adequate for obtaining the stress and deflection values for Body Clip, and the FEA results for the stress at the point of interest align well with the analytical solution of a simplified model. However, this is not the maximum stress in the FEA which is 24.144 MPa. This value is within the yield strength of PETG making this a viable material selection for this application.

### 3.9 Arm Calculations

During flight operations, the drone is subject to thrust forces requiring the validation of design structures to ensure that the drone arms remain stiff and resist large deformations. The following FBD and equations were used to validate the design of Arm V5 utilized in drone version 4 and Arm V8 utilized in drone versions 5 and 6. Figure 46 shows the FBD during flight operations on Arm V5. Figure 47 shows the cross-sectional area of Arm V5.

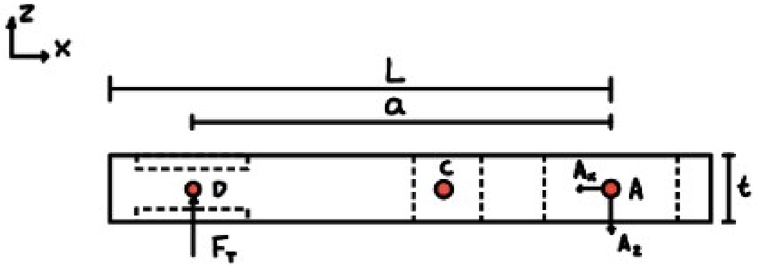

Figure 46: Arm V5 FBD (Flight).

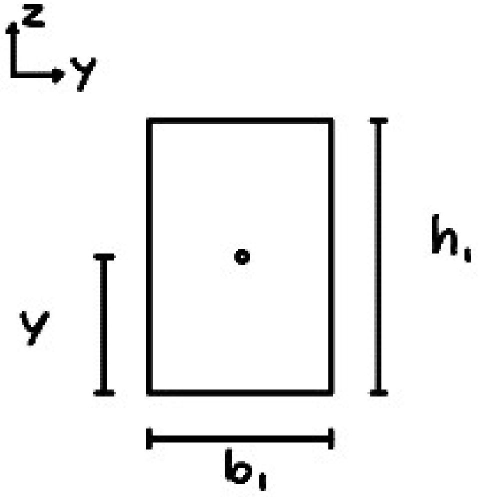

Figure 47: Arm V5 Cross Section.

$$y = \frac{h_1}{2} \tag{19}$$

$$I = \frac{b_1 \cdot {h_1}^3}{12} \tag{20}$$

$$\sigma_{max} = \frac{-F_T \cdot a \cdot y}{I \cdot N} \tag{21}$$

$$\delta_{max} = \frac{F_T \cdot a^2 \cdot (L - a)}{6 \cdot E \cdot I \cdot N} \tag{22}$$

Equation 19 represents the distance from the neutral axis (y) as half the height of the cross-section ($h_1$). Equation 20 represents the mass moment of inertia (I) as the product of the base ($b_1$) and the height ($h_1$) cubed divided by 12 for a rectangular cross-section. Equation 21 represents the maximum stress ($\sigma_{max}$) as the product of the negative thrust force ($F_T$), the distance between $F_T$ and point A (a) squared, and y. Divided by the product of I and the number of beams (N). Equation 22 gives the maximum deflection ($\delta_{max}$) as the product of $F_T$, "a" squared, and the subtraction of the total length (L) and "a" divided by 6 times the product of the elastic modulus of the material (E), I, and N. The maximum stress and deflection for Arm V5 during flight operations are 2.08 MPa, and 1.36 mm respectively. These values are below the yield stress for HIPS making this a viable design. Figure 48 shows the FBD for Arm V8 during flight operations. Figure 49 shows the cross-section of Arm V8. Notably, this cross-section is a simplex shape and requires a parallel axis theorem to be able to calculate the mass moment of inertia.

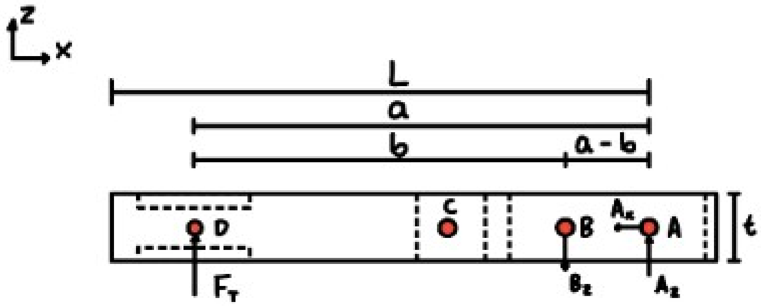

Figure 48: Arm V8 FBD (Flight).

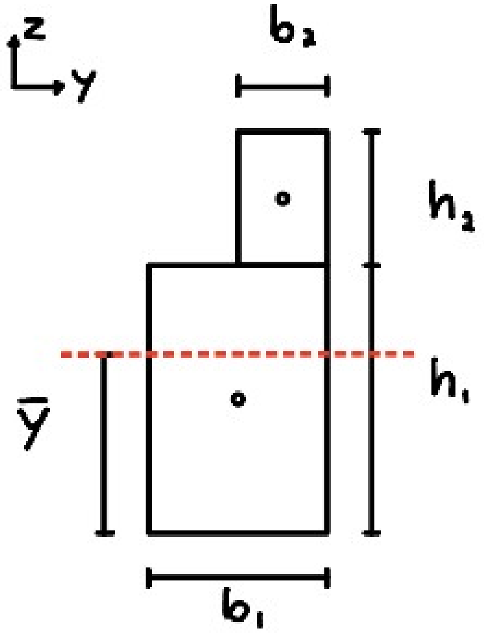

Figure 49: Arm V8 Cross Section.

$$y_1 = \frac{h_1}{2} \tag{23}$$

$$y_2 = \frac{h_2}{2} + h_1 \tag{24}$$

$$A_i = b_i \cdot h_i \tag{25}$$

$$\bar{y} = \frac{\sum y_i \cdot A_i}{\sum A_i} \tag{26}$$

$$d_i = abs|\bar{y} - y_i| \tag{27}$$

$$I_{z1} = \frac{b_1 \cdot h_1^3}{12} + b_1 \cdot h_1 \cdot d_1^2 \tag{28}$$

$$I_{z_2} = \frac{b_2 \cdot h_2^3}{12} + b_2 \cdot h_2 \cdot d_2^2 \tag{29}$$

$$I_z = \mathrm{N}(I_{z_1} + I_{z_2}) \tag{30}$$

$$\sigma = \frac{F_T \cdot b \cdot \bar{y}}{I_z} \tag{31}$$

$$\delta = \frac{F_T \cdot b^2 \cdot L}{3 \cdot E \cdot I_z} \tag{32}$$

Equation 23 represents the distance from the neutral axis of the first shape ($y_1$) as half the height of the first shape ($h_1$). Equation 24 represents the distance from the neutral axis of the second shape as a sum of half of the height of the second shape ($h_2$) and $h_1$. Equation 25 represents the area of each shape ($A_i$) as the product of each base ($b_i$) and each height ($h_i$). Equation 26 represents the actual distance of the composite shape from the neutral axis ($\bar{y}$) as the summation of the product between each y ($y_i$) and each area ($A_i$) divided by the summation of all areas ($A_i$). Equation 27 represents the distance between the $\bar{y}$ and each $y_i$ ($d_i$) as the absolute value of the subtraction of $y_i$ from the $\bar{y}$. Equation 28 represents the mass moment of inertia for the first shape as the summation of the product of $b_1$ and $h_1$ divided by 12 and the product of the $b_1$, $h_1$, and the first distance ($d_1$). Equation 29 follows the same calculations but for the second shape. Equation 30 represents the total mass moment of inertia as a product between the number of beams (N) and the sum of both I. Equation 31 gives the maximum stress ($\sigma$) as the product of the thrust force ($F_T$), the distance between the force and point B (b), and $\bar{y}$ divided by $I_z$. Equation 32 represents the maximum deflection ($\delta_{max}$) as the product of $F_T$, b squared, and the length (L). Divided by the product of 3, the Elastic Young's Modulus of the material (E), and I. The maximum stress and deflection values that were calculated for Arm V8 are 0.55 MPa, and 0.239 mm respectively. These stress values are below the yield values for PETG making this a viable design.

## 3.10 Arm FEA

To perform a static FEA for the Arm the following steps were conducted in Fusion 360.

1. Import CAD models
    1.1. Imported model file format should be IGES

    1.2. Click the “Design” button and select “Simulation”
    1.3. In the ensuing pop-up, select “Static Analysis”
2. Material selection
    2.1. Note that Fusion 360’s material library lacks profiles for PETG, HIPS, and TPU
    2.2. Custom material profiles were created for PETG, HIPS, and TPU utilizing the material properties obtained in Chapter I
3. Fixed geometry and load application
    3.1. Apply fixed geometry that best represents the component application
    3.2. For Arm V5 the fixed geometry was the screw pocket at point A
    3.3. For Arm V8 the fixed geometry was in the screw pocket at point A
    3.4. For Arm V8 point B was assigned a roller geometry
    3.5. Apply the load
    3.6. Make sure the load is facing the correct orientation and applied in the correct geometry
4. Mesh generation
    4.1. Create a mesh for simulation
    4.2. The mesh size for this simulation is 3%
    4.3. A convergence analysis was conducted between 2%, 3%, and 4% mesh size
5. Analyze results

Figure 50 shows the boundary conditions for Arm V5.

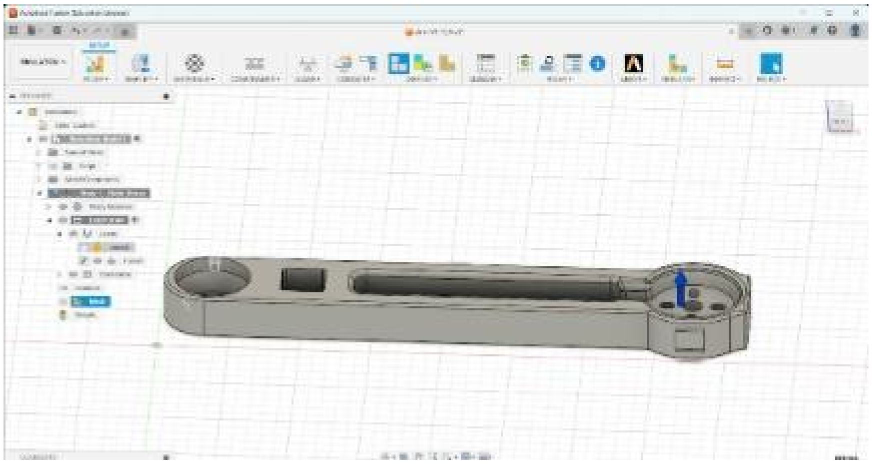

Figure 50: Arm V5 FEA Boundary Conditions.

Figure 51 shows the maximum deflection of Arm V5 as 1.463 mm.

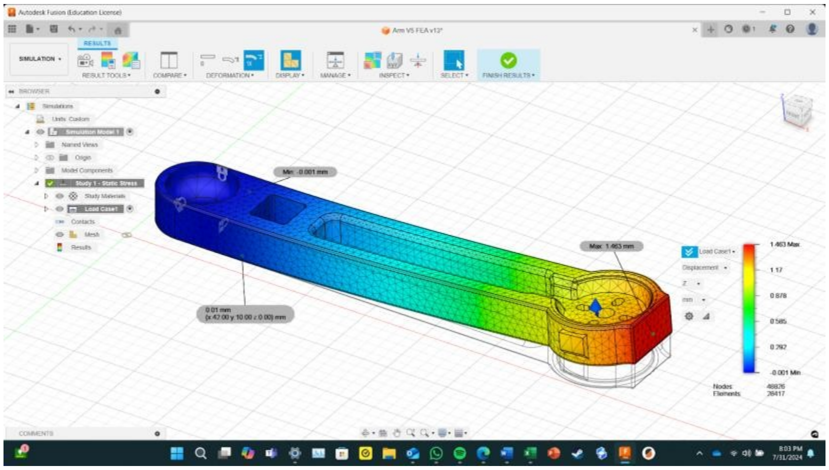

Figure 51: Displacement Results (mm) for Arm V5 FEA (3% Mesh Size).

Figure 52 shows the maximum stress of Arm V5 at 4.15 MPa. The stress at the point of interest is 2.17 MPa.

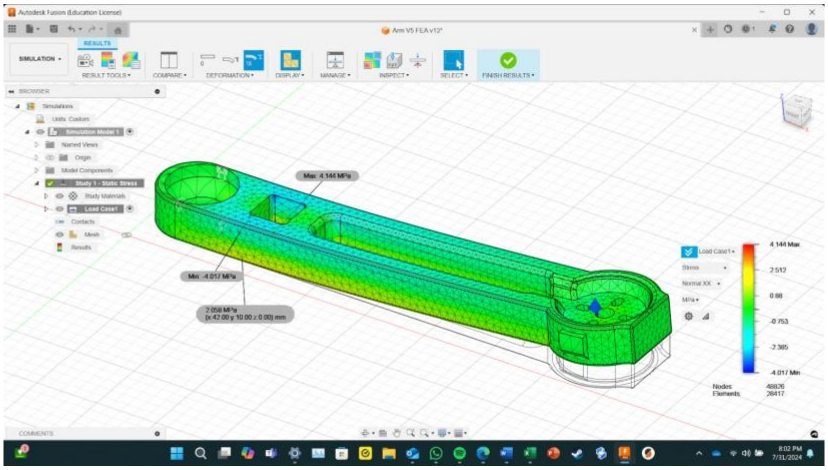

Nodes: 48826
Elements: 28417

Figure 52: Stress Results (MPa) for Arm V5 FEA (3% Mesh Size).

Figure 53 shows the mesh of Arm V5 at 4%.

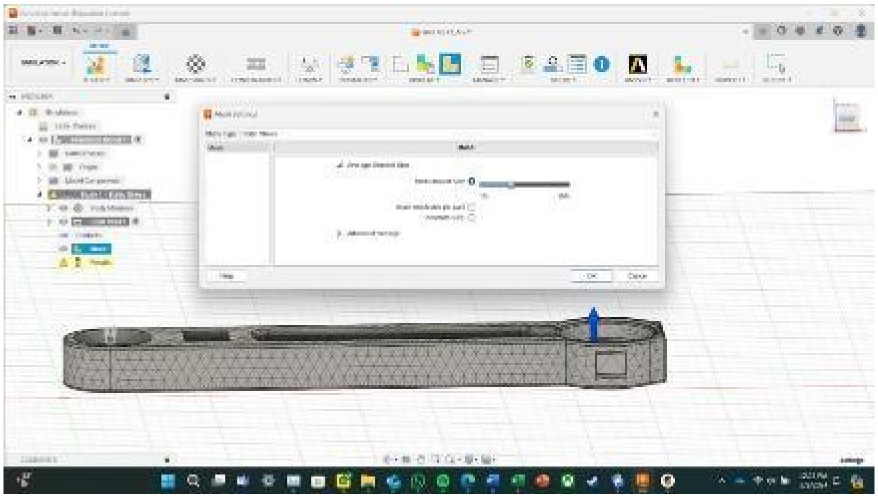

Figure 53: Arm V5 FEA with 4% Mesh Size.

Figure 54 shows the maximum deflection of Arm V5 as 1.463 mm.

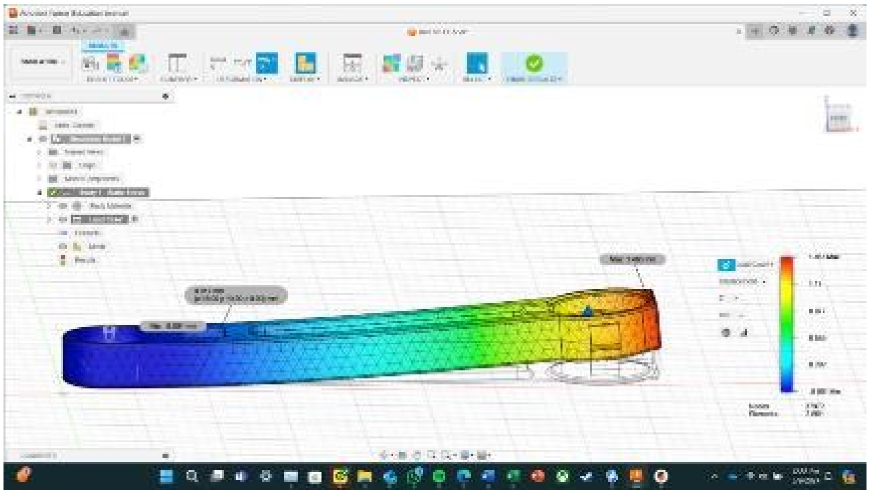

Figure 54: Displacement Results (mm) for Arm V5 FEA (4% Mesh Size).

Figure 55 shows the maximum stress of Arm V5 at 4.25 MPa. The stress at the point of interest is 2.168 MPa.

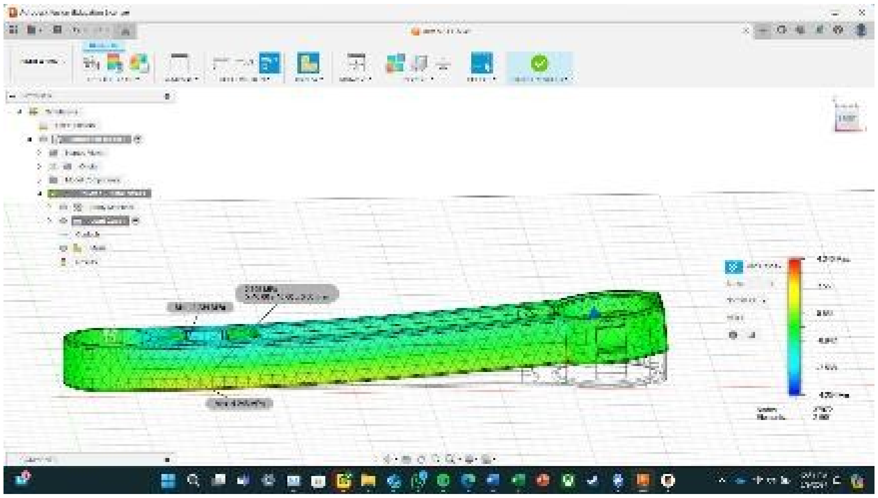

Figure 55: Stress Results (MPa) for Arm V5 FEA (4% Mesh Size).

Figure 56 shows the mesh of Arm V5 at 2%.

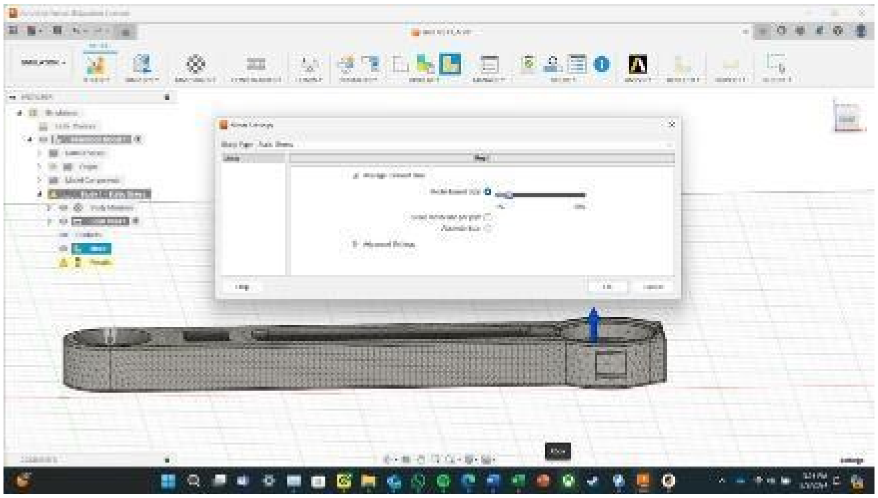

Figure 56: Arm V5 FEA with 2% Mesh Size.

Figure 57 shows the maximum deflection of Arm V5 as 1.465 mm.

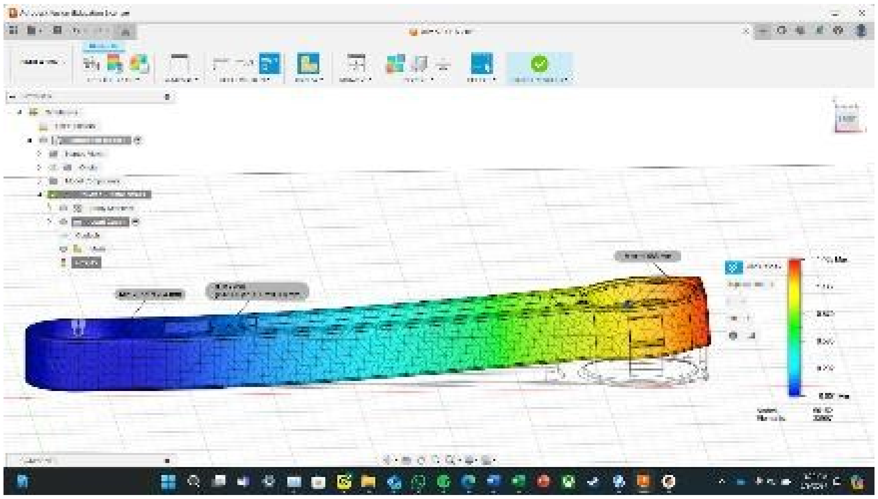

Figure 57: Displacement Results (mm) for Arm V5 FEA (2% Mesh Size).

Figure 58 shows the maximum stress of Arm V5 at 3.91 MPa. The stress at the point of interest is 2.17 MPa.

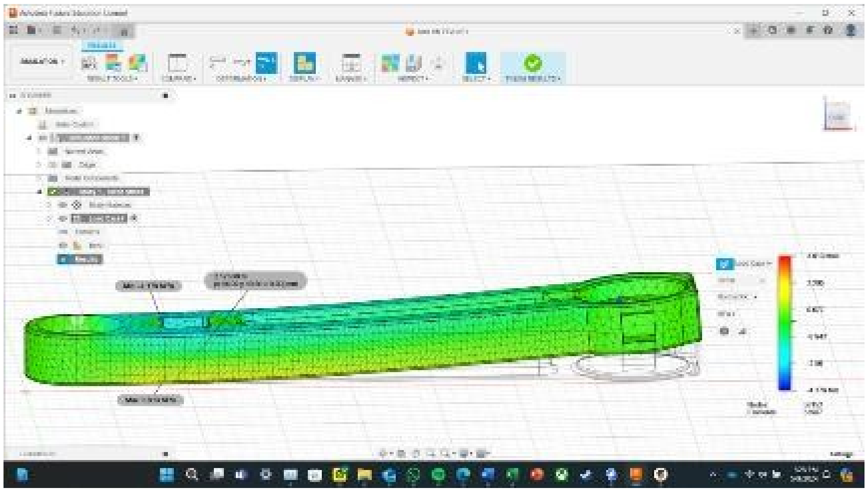

Figure 58: Stress Results (MPa) for Arm V5 FEA (2% Mesh Size).

Figure 59 shows the mesh of Arm V8 at 3%.

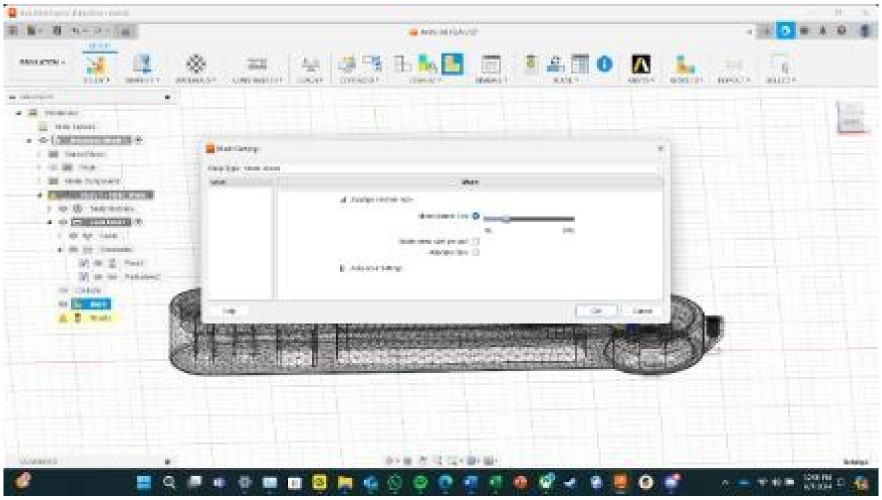

Figure 59: Arm V8 FEA with 3% Mesh Size.

Figure 60 shows the maximum deflection of Arm V8 as 0.631 mm.

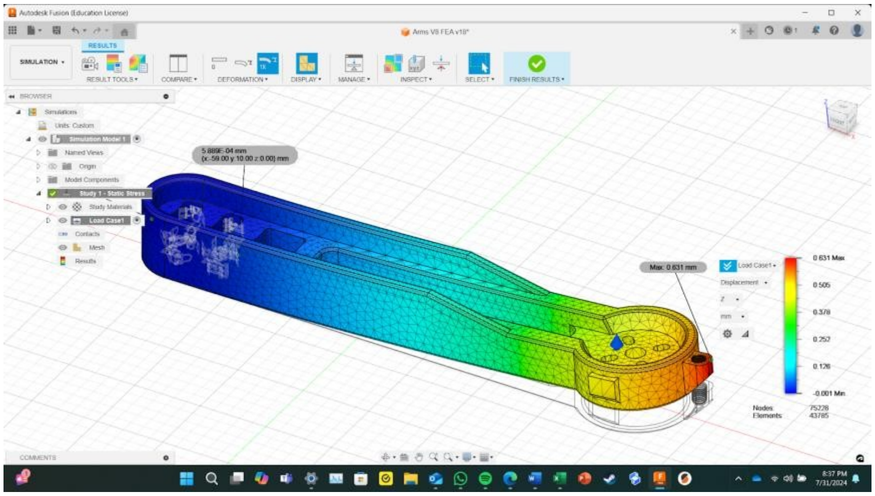

Figure 60: Displacement Results (mm) for Arm V8 FEA (3% Mesh Size).

Figure 61 shows the maximum stress of Arm V8 at 2.09 MPa. The stress at the point of interest is 0.61 MPa.

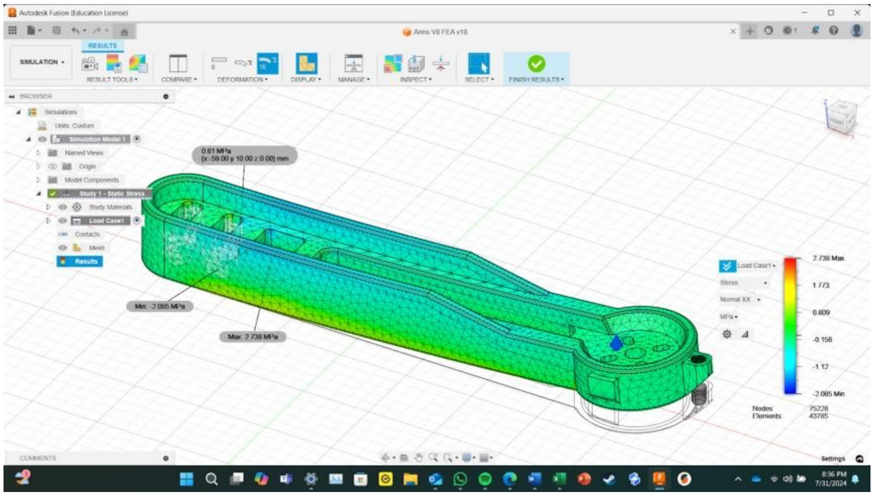

Figure 61: Stress Results (MPa) for Arm V8 FEA (3% Mesh Size).

Figure 62 shows the mesh of Arm V8 at 2%.

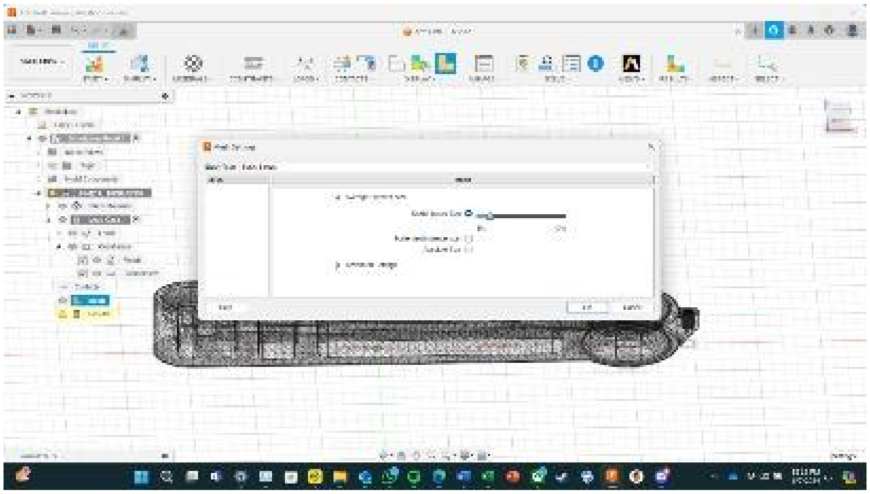

Figure 62: Arm V8 FEA with 2% Mesh Size.

Figure 63 shows the maximum deflection of Arm V8 as 0.63 mm.

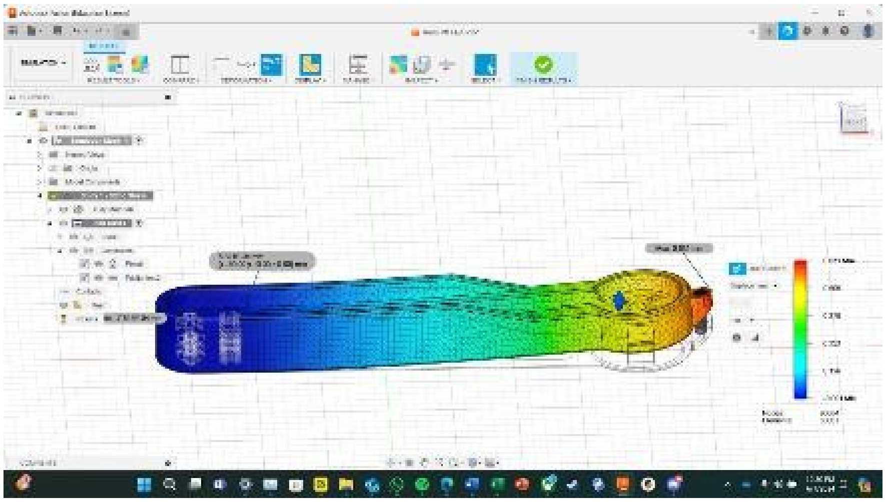

Figure 63: Displacement Results (mm) for Arm V8 FEA (2% Mesh Size).

Figure 64 shows the maximum stress of Arm V8 at 2.49 MPa. The stress at the point of interest is 0.59 MPa.

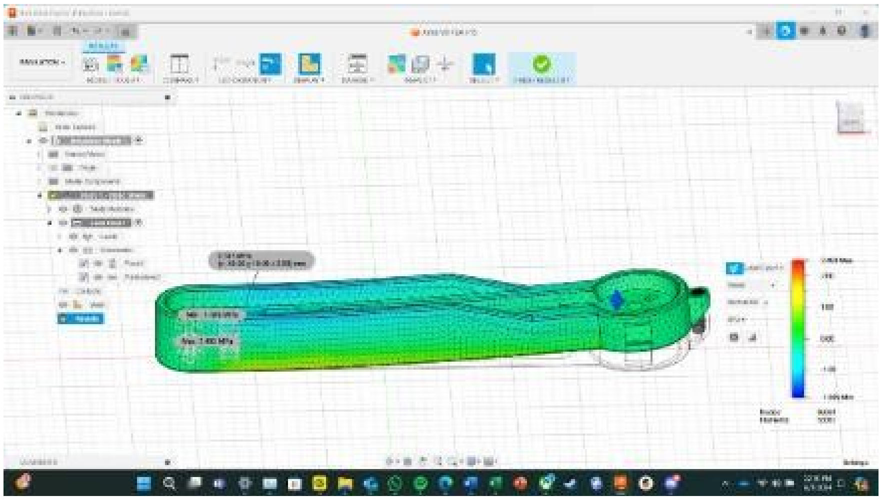

Figure 64: Stress Results (MPa) for Arm V8 FEA (2% Mesh Size).

Figure 65 shows the mesh of Arm V8 at 4%.

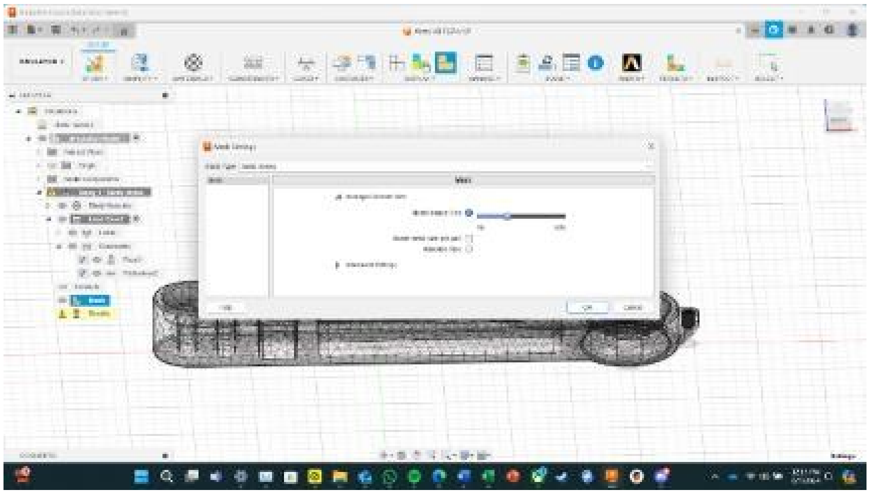

Figure 65: Arm V8 FEA with 4% Mesh Size.

Figure 66 shows the maximum deflection of Arm V8 as 0.63 mm.

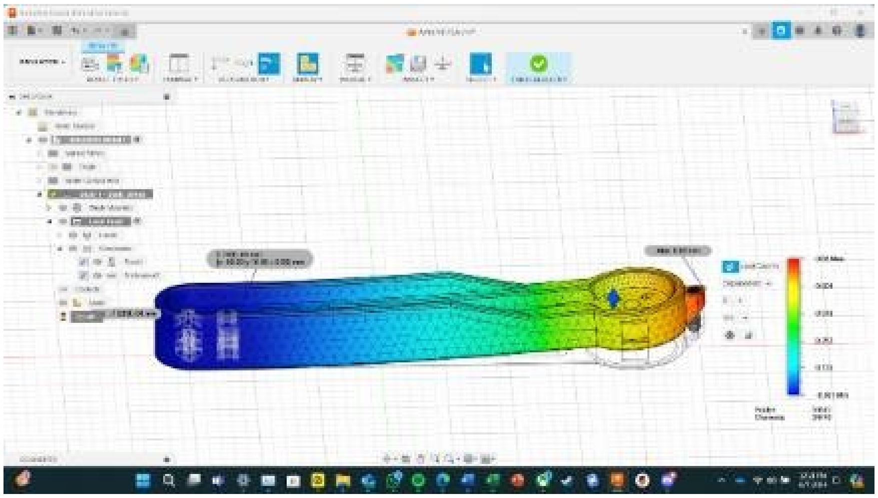

Figure 66: Displacement Results (mm) for Arm V8 FEA (4% Mesh Size).

Figure 67 shows the maximum stress of Arm V8 at 2.8 MPa. The stress at the point of interest is 0.59 MPa.

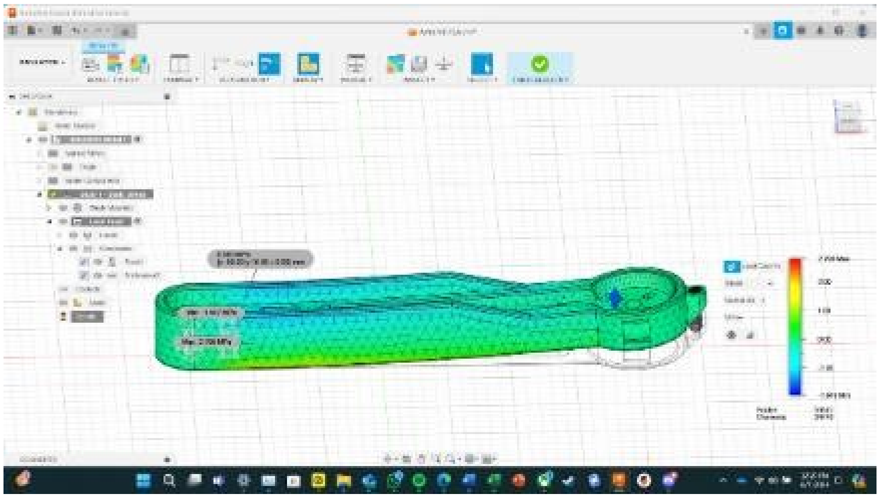

Figure 67: Stress Results (MPa) for Arm V8 FEA (4% Mesh Size).

The percent error assessment for Arm V5, utilizing Equation 17, yielded the following result for deflection an error of 7.35% was observed, for the stress at the point of interest an error of 0.72% was observed. The convergence analysis for Arm V5 showed that changing the mesh size by ±1% from the base 3% yielded a 0.14% difference for stress and a 0.34% difference for deflection. Therefore, a 3% mesh size is adequate for obtaining accurate stress and deflection values for Arm V5. The FEA results for the stress at the point of interest align well with the analytical solution of a simplified model. Note that this is not the maximum stress in the FEA which is 4.14 MPa. This value does not exceed the yield stress for HIPS, making it a suitable material. However, the maximum deflection for the loading condition of Arm V5 exceeds the conditional limit of sub 1 mm. The design of Arm V5 also had some considerable limitations concerning impact resistance. The topic of impact resistance will be discussed in Chapter VI.

The percent error assessment for Arm V8, utilizing Equation 17, yielded the following result for deflection an error of 163.6% was observed, for the stress at the point of interest an error of 10.9% was observed. This high error in deflection can be routed into an error during the simplification of the Arm V8 design for the analytical approach. The analytical approach assumes the beam to be stiffer all around by not considering the lack of height increase at the end of the design. Additionally, the error calculated is the absolute error, but the deflection values are still in the same size and sub 1 mm. The stress seems to align very well for a simplified model with a 10.9% error. Therefore, for this study, the error between the analytical solution and FEA can be due to not fully representing the structure in the analytical approach. Since the FEA stress is within the margin of error (15% for complex geometry) for the design the FEA values will be used to validate the design. The convergence analysis for Arm V5 showed that changing the mesh size by ±1% from the base 3% yielded a 3.28% difference for stress and a 0.0% difference for deflection. Therefore, a 3% mesh size is adequate for obtaining accurate stress and deflection values for Arm

V8. The FEA results for the stress at the point of interest align well with the analytical solution. Note that this is not the maximum stress in the FEA, which is 2.01 MPa. This value does not exceed the yield stress for HIPS, making it a suitable material. However, the maximum deflection for the loading condition of Arm V8 does not exceed the conditional limit of sub 1 mm.

### 3.11 Impact Calculations

To validate the design and function of the drone impact resistance, the impact force experienced during a free fall from the operational height of 1 meter needed to be calculated. The following FBD and equations were used to validate the screw design selection and the spring mechanism. Figure 68 shows the FBD of one of the arm assemblies during impact loading. Since the drone design is symmetric, the analysis for all the arms is the same.

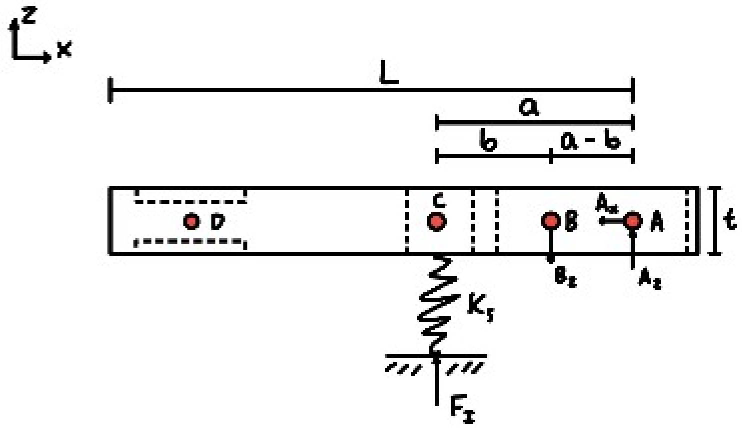

Figure 68: Impact Calculations FBD.

$$IF = 1 + \sqrt{1 + \frac{2 \cdot h}{\delta_{st}}} \tag{33}$$

$$\delta_{st} = \delta_{B_z} + \delta_s \tag{34}$$

$$\delta_s = \frac{w}{4 \cdot k_s} \tag{35}$$

$$\delta_{B_z} = \frac{\frac{w}{4} \cdot b^2 \cdot L}{3 \cdot E \cdot I_B} \tag{36}$$

$$\delta_I = \delta_{st} \cdot IF \tag{37}$$

$$F_I = \frac{w \cdot IF}{4} \tag{38}$$

Equation 33 gives the impact factor (IF) as a function of the operational drop height (h), and the static deflection of the arm leg assembly due to the static load of the drone weight ($\delta_{st}$). Equation 34 gives $\delta_{st}$ as the sum of the static deflection of the arm ($\delta_{Bz}$), and the static deflection of the spring ($\delta_s$ given by Equation 35 as the weight of the drone (w) divided by four times the stiffness of the spring ($k_s$). Equation 36 gives $\delta_{Bz}$ as a function of the drone weight (w), the distance between the first screw and the impact force (b), and the length of the arm (L), the modules of elasticity for the material (E), and the total mass moment of inertia for the arm ($I_B$). Equation 37 represents the deflection of impact ($\delta_I$) as the product of $\delta_{st}$ and IF. Equation 38 represents the force of impact ($F_I$) as the product of one-fourth of the weight and IF.

### 3.12 Screw Calculations

To justify the screw design selection the reactionary force experienced on the screw during an impact case needed to be obtained and compared to the proof strength of the bolt and nut ($S_p$). The following FBD and equations were utilized to obtain the maximum reactionary force ($B_z$). Figure 69 shows the FBD for the Arm V8 during impact loading.

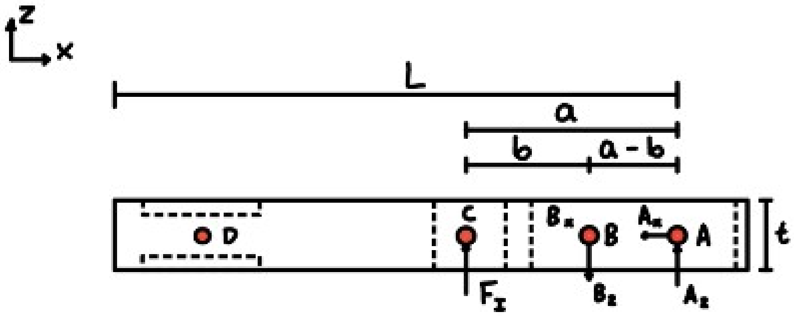

Figure 69: Screw Impact Loading FBD.

$$A_z = \frac{F_I \cdot b}{(a - b)} \tag{39}$$

$$B_z = F_I + A_z \tag{40}$$

$$B_z < S_p \tag{41}$$

Equation 39 represents the reaction at point A (Az) due to the force of impact as the product between the force of impact ($F_I$) and the distance between the impact force and point B (b). The denominator is the subtraction of the b divided by the difference between points A and B. Equation 40 represents the reaction force of point B ($B_z$) as the sum of $F_I$ and $A_z$, and Equation 41 represents the governing condition of validation for the screw design between $B_z$ and the proof strength of the screws ($S_p$). To obtain the $S_p$ of the screw design the screws were manufactured and tested following the procedures in Chapter V. The $S_p$ of the screw and results of testing will be further discussed in Chapter VI.

## 3.13 Spring Stiffness Calculations

To help validate the effectiveness of the spring design the spring stiffness of the three spring designs were calculated. Proper stiffness of a spring has been proven to help reduce the impact force experienced by a solid body.

$$k = \frac{F}{\delta} \tag{42}$$

Equation 42 gives the spring constant (k) by dividing the force applied (F) by the deflection experienced on the solid body (δ). To obtain “k” the spring designs were manufactured and tested using the following procedures.

### 3.13.1 Spring Testing Procedures

1. Slice the spring test sample design
    1.1. Follow the optimal material manufacturing profiles as stated in Chapter IV
2. Manufacture the spring test sample
    2.1. Clean up the stringing observed in FDM samples.
3. Obtain the measuring materials
    3.1. Caliper for measuring
    3.2. Calibrated weights for applying the load
    3.3. Cleared flat surface as a controlled testing surface

    3.4. Notepad and pencil for recording test results

4. Place the spring on the flat surface
5. Measure the spring-unweighted distance and record it
6. Apply the load as uniaxially as possible
7. Measure the spring-weighted distance and record it
8. Conduct the test five times in one-minute intervals
9. Calculate the average deflection from the tests
10. Using Equation 41, the average deflection, and applied load calculate the spring stiffness (k)
11. Conduct FEA with the same applied load
12. Compare FEA results with the experimental results

Table 1: Long Spring Test (HIPS)

| Long Spring Test (HIPS) | | | | |
|---|---|---|---|---|
| | **Unweighted [mm]** | **Weighted [mm]** | **Deflection [mm]** | |
| 1 | 58.6 | 57.5 | 1.1 | |
| 2 | 58.3 | 57.8 | 0.5 | |
| 3 | 58.6 | 57.6 | 1 | |
| 4 | 58.4 | 57.2 | 1.2 | |
| 5 | 58.7 | 57 | 1.7 | |
| | | | | |
| Average Deflection [mm] | 1.1 | | | |

The average deflection for all the testing conducted on the Long Spring Test (HIPS) design was calculated to be 1.1 mm.

Table 2: Spring Single Test (TPU)

| Spring Single Test (TPU) | | | | |
|---|---|---|---|---|
| | Unweighted [mm] | Weighted [mm] | Deflection [mm] | |
| 1 | 60.2 | 58.4 | 1.8 | |
| 2 | 60.2 | 57 | 3.2 | |
| 3 | 60.2 | 57.8 | 2.4 | |
| 4 | 60.2 | 57.4 | 2.8 | |
| | | | | |
| Average Deflection [mm] | 2.55 | | | |

The average deflection for all the testing conducted on the Spring Single Test (TPU) design was calculated to be 2.55 mm.

Table 3: Spring Double Test (TPU)

| Spring Double Test (TPU) | | | | |
|---|---|---|---|---|
| | unweighted (mm) | weighted (mm) | Deflection (mm) | |
| 1 | 102 | 101.8 | 0.2 | |
| 2 | 101.3 | 101 | 0.3 | |
| 3 | 101.4 | 100.6 | 0.8 | |
| 4 | 101.4 | 100.6 | 0.8 | |
| | | | | |
| Average deflection (mm, m) | 0.525 | 0.000525 | | |

The average deflection for all the testing conducted on the Spring Double Test (TPU) design was calculated to be 0.535 mm. Figure 70 shows an example of how the measuring was performed for an unweighted spring.

Figure 70: Long Spring (HIPS) Unweighted Measurement (mm).

Figure 71 shows all the testing equipment used to conduct the tests for the spring stiffness.

Figure 71: Spring Testing Equipment (with Long Spring Test Sample).

Figure 72 shows an example of the single TPU spring sample used for testing.

Figure 72: Spring Single (TPU) Test Sample.

Figure 73 shows an example of the double TPU spring sample used for testing.

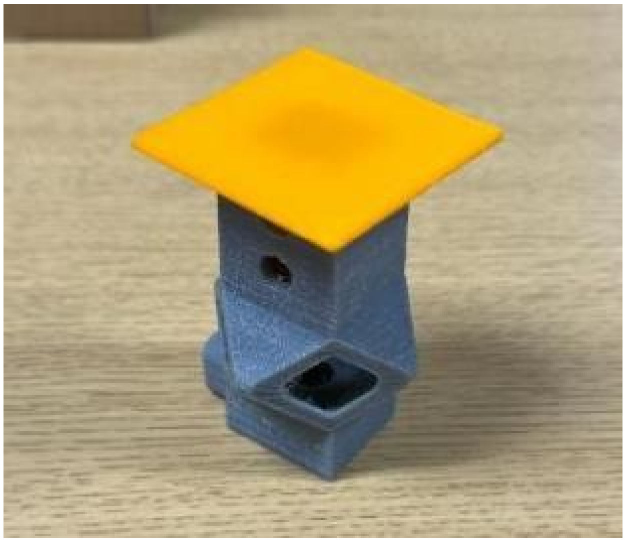

Figure 73: Spring Double (TPU) Test Sample.

## 3.14 Spring Stiffness FEA

To perform a static FEA for the spring designs the following steps were conducted in Fusion 360.

1. Import CAD models
    1.1. The imported model file format should be IGES
    1.2. Click the “Design” button and select “Simulation”
    1.3. In the ensuing pop-up, select “Static Analysis”
2. Material selection
    2.1. Select the appropriate material for component analysis
    2.2. Note that Fusion 360’s material library lacks profiles for PETG, HIPS, and TPU
    2.3. Custom material profiles were created for PETG, HIPS, and TPU utilizing the material properties obtained in Chapter I
3. Fixed geometry and load application
    3.1. Apply fixed geometry that best represents the component application
    3.2. For the spring designs the fixed geometry was the bottom face
    3.3. Apply the load corresponding to the load applied during testing
    3.4. Make sure the load is facing the correct orientation and applied in the correct geometry
4. Mesh generation
    4.1. Create a mesh for simulation
    4.2. The mesh size for this simulation is 3%
    4.3. A convergence analysis was conducted between 2%, 3%, and 4% mesh size

5. Compare FEA results with those obtained through experimental testing

Figure 74 shows the mesh of the Long Spring at 3%.

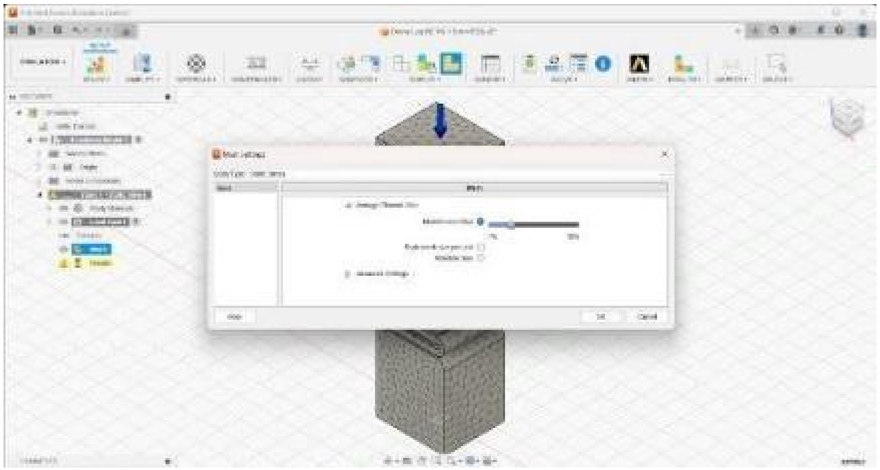

Figure 74: Long Spring FEA with 3% Mesh Size.

Figure 75 shows the maximum deflection of the Long Spring as 1.81 mm.

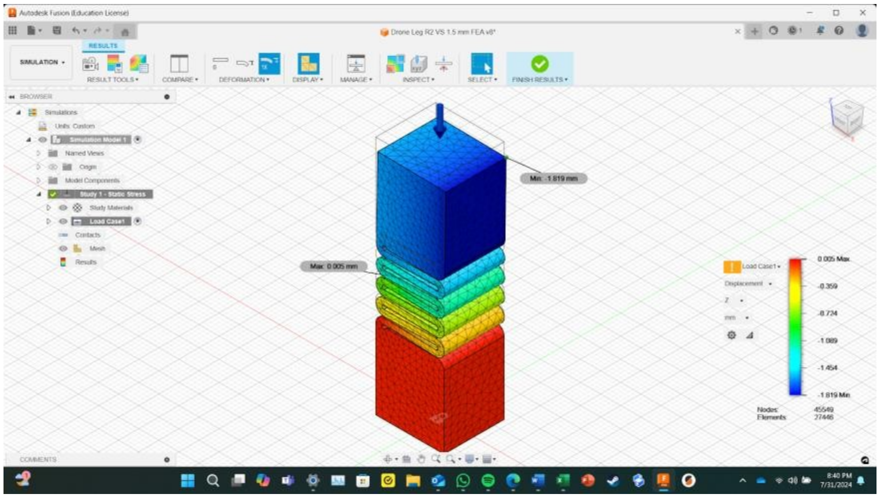

Nodes: 45549
Elements: 27448

Figure 75: Displacement Results (mm) for the Long Spring.

Figure 76 shows the mesh of the Long Spring at 4%

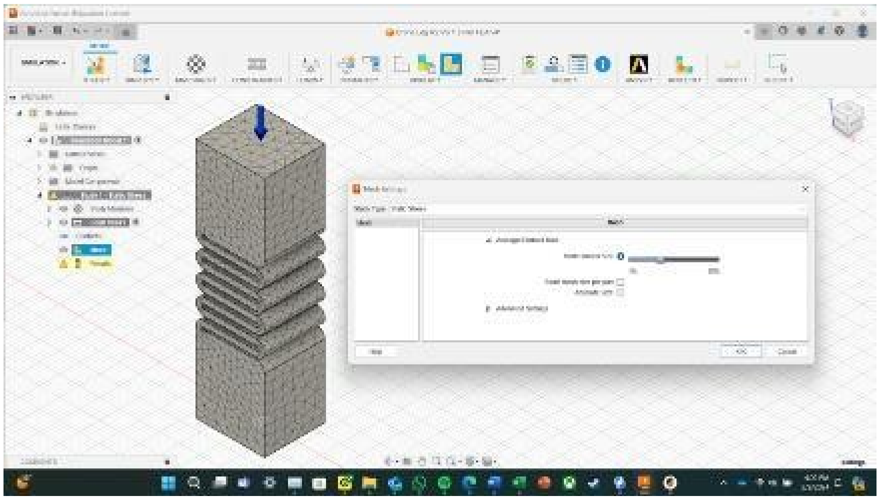

Figure 76: Long Spring FEA with 4% Mesh Size.

Figure 77 shows the maximum deflection of the Long Spring as 1.793 mm.

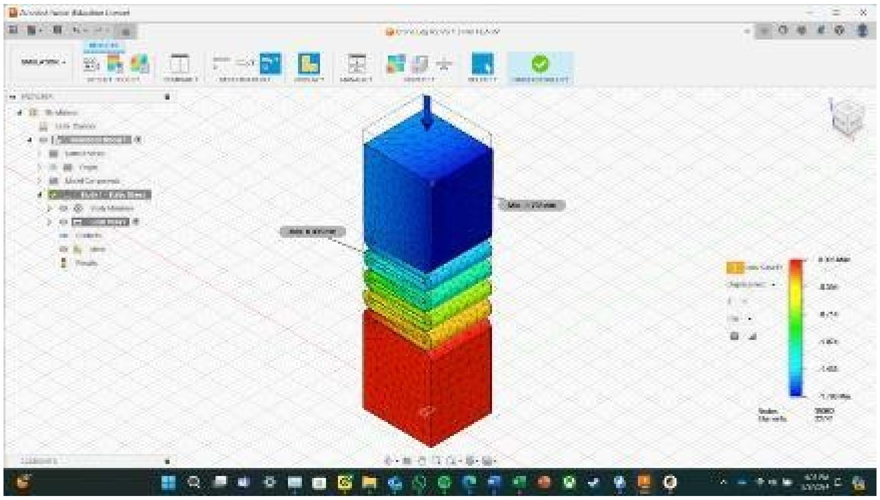

Figure 77: Displacement Results (mm) for Long Spring FEA (4% Mesh Size).

Figure 78 shows the mesh of the Long Spring at 2%.

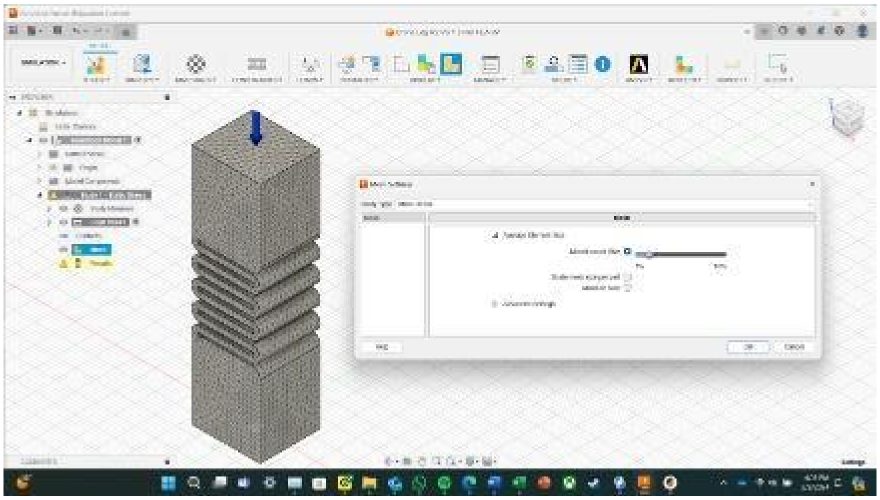

Figure 78: Long Spring FEA with 2% Mesh Size.

Figure 79 shows the maximum deflection of the Long Spring as 1.843 mm.

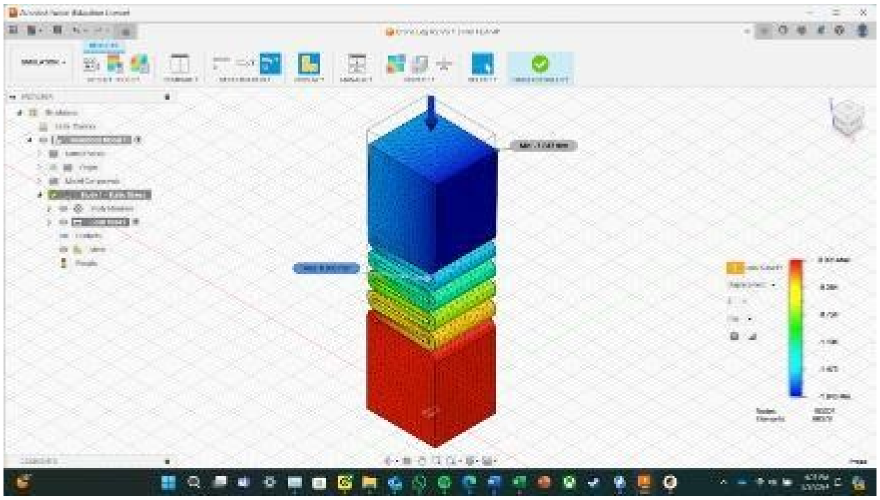

Figure 79: Displacement Results (mm) for Long Spring (2% Mesh Size).

Figure 80 shows the mesh of the Spring Single at 3%.

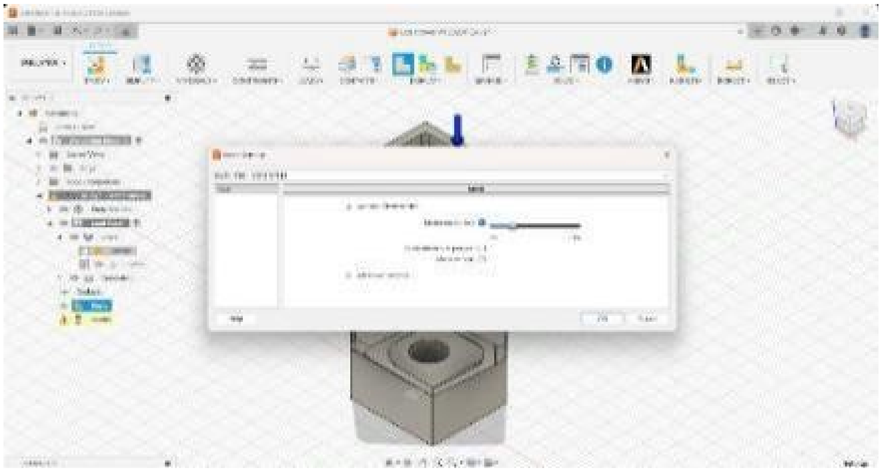

Figure 80: Spring Single FEA with 3% Mesh Size.

Figure 81 shows the maximum deflection of the Spring Single as 2.23 mm.

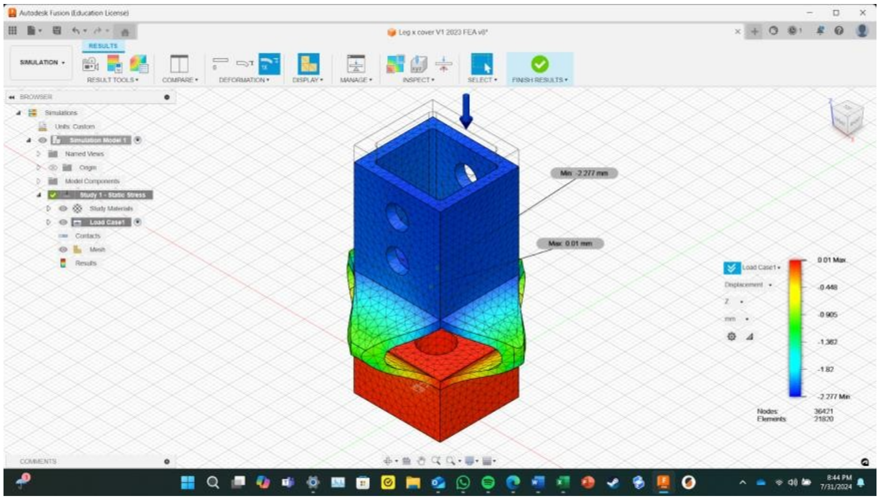

Figure 81: Displacement Results (mm) for Spring Single FEA (3% Mesh Size).

Figure 82 shows the mesh of the Spring Single at 4%.

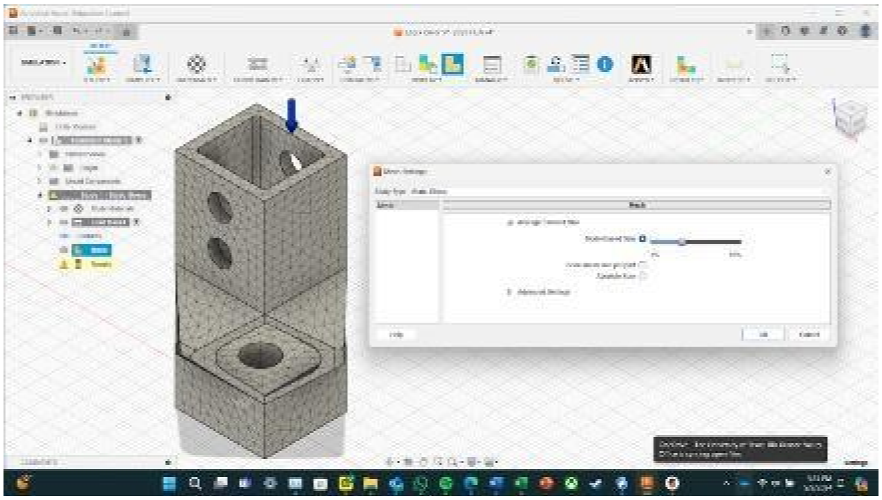

Figure 82: Spring Single FEA with 4% Mesh Size.

Figure 83 shows the maximum deflection of the Spring Single as 2.193 mm.

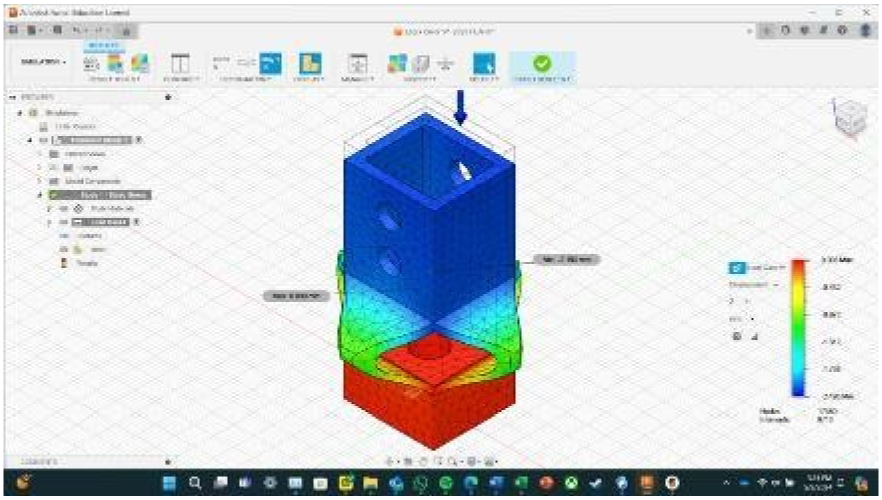

Figure 83: Displacement Results (mm) for Spring Single FEA (4% Mesh Size).

Figure 84 shows the mesh of the Spring Single at 2%.

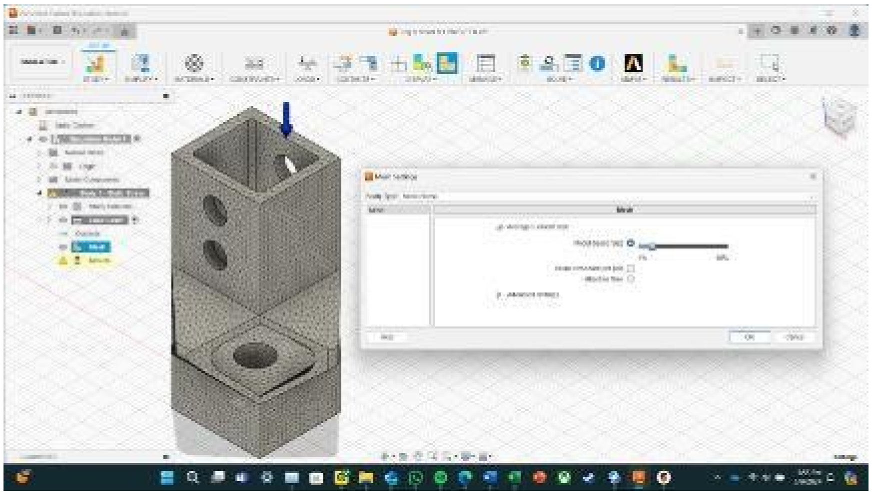

Figure 84: Spring Single FEA with 2% Mesh Size.

Figure 85 shows the maximum deflection of the Spring Single as 2.349 mm.

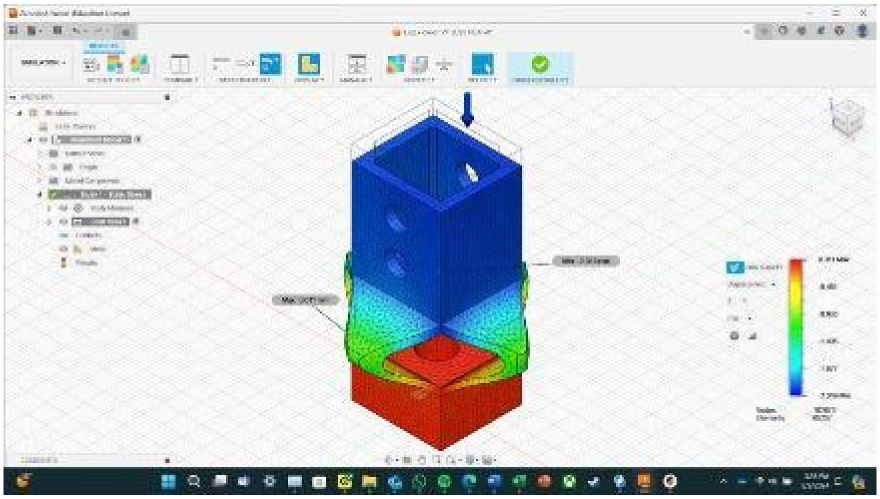

Figure 85: Displacement Results (mm) for Spring Single FEA (2% Mesh Size).

Figure 86 shows the mesh of the Spring Double at 3%.

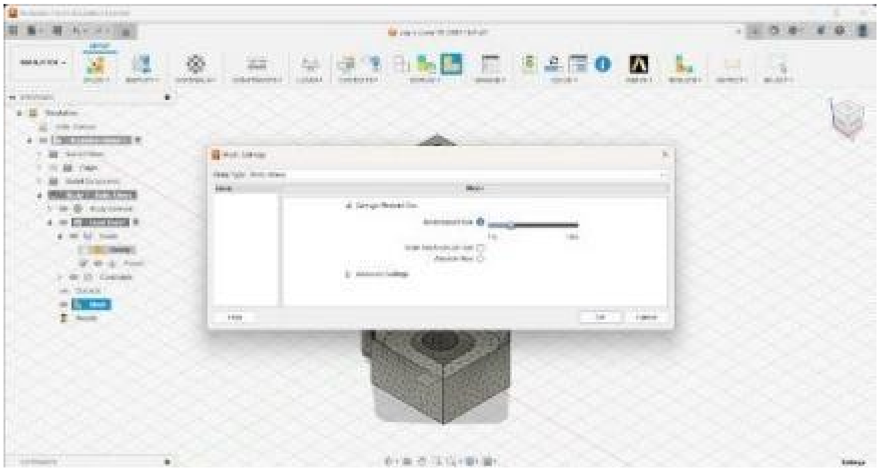

Figure 86: Spring Double FEA with 3% Mesh Size.

Figure 87 shows the maximum deflection of the Spring Double as 0.77 mm.

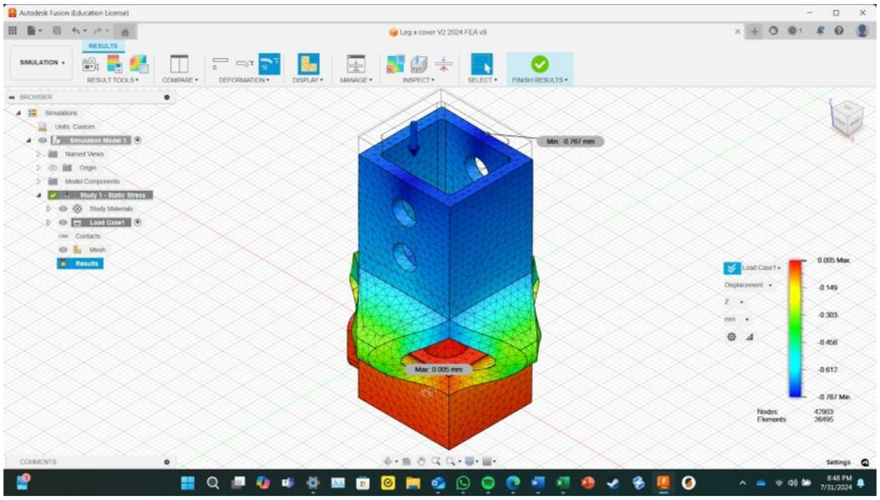

Nodes: 42903
Elements: 26495

Figure 87: Displacement Results (mm) for Spring Double FEA (3% Mesh Size).

Figure 88 shows the mesh of the Spring Double at 4%.

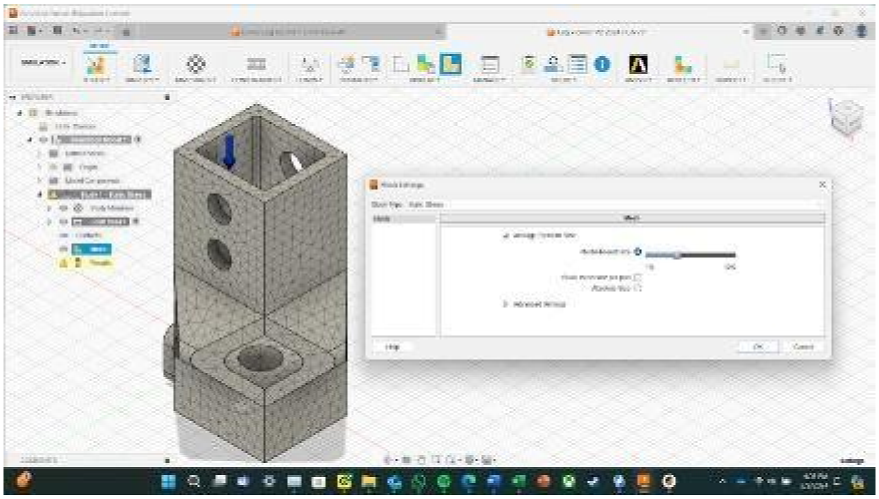

Figure 88: Spring Double FEA with 4% Mesh Size.

Figure 89 shows the maximum deflection of the Spring Double as 0.78 mm.

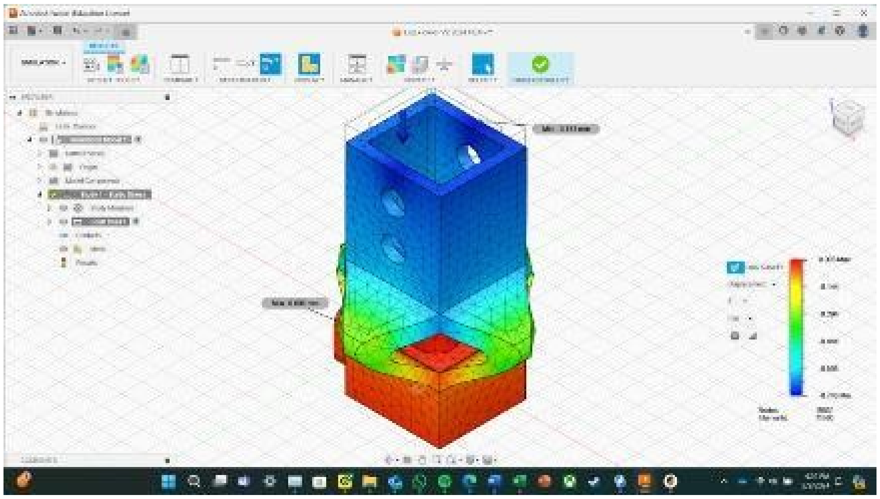

Figure 89: Displacement Results (mm) for Spring Double FEA (4% Mesh Size).

Figure 90 shows the mesh of the Spring Double at 2%

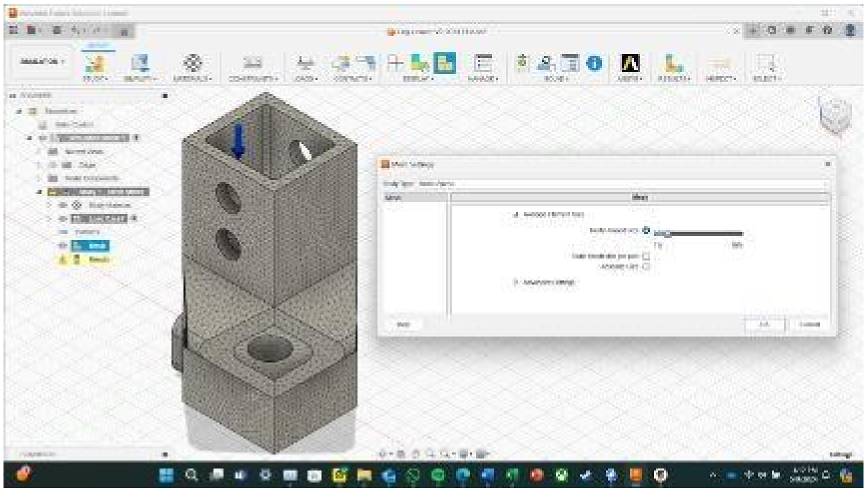

Figure 90: Spring Double FEA with 2% Mesh Size.

Figure 91 shows the maximum deflection of the Spring Double as 0.743 mm.

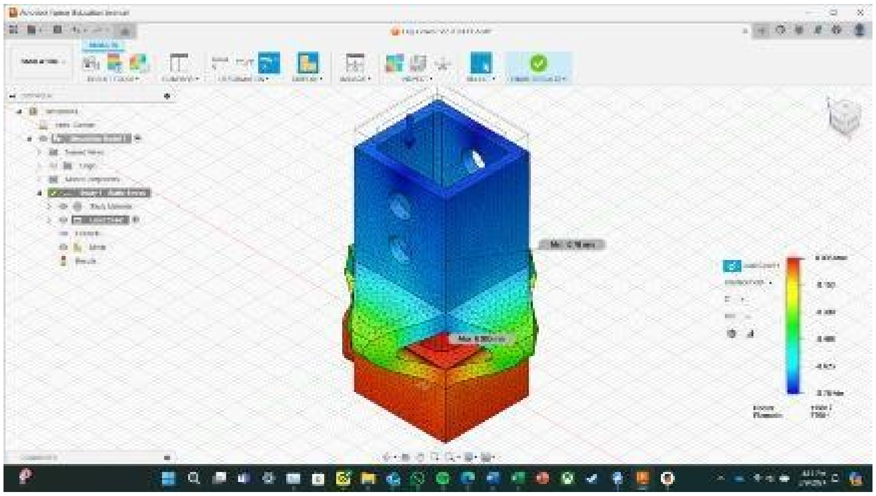

Figure 91: Displacement Results (mm) for Spring Double FEA (2% Mesh Size).

The percentage error assessment for the Long Spring, utilizing Equation 17 yielded the following results: for deflection, an error of 64.55% was seen. The reason for this high error is that the method of obtaining the weighted measurements was not fully reliable. This can be observed in the scatter within the five recordings in Table 1. The maximum deflection for the loading condition of the Long Spring in the FEA is 1.81 mm which is within the realistic scatter of the measurements obtained in Table 1. Therefore, the values of the FEA are valid. The convergence analysis for the Long Spring showed that changing the mesh size ±1% from the base 3% resulted in a 1.82% variance in values, hence the 3% mesh size is adequate for obtaining accurate deflection values for the Long Spring.

The percentage error assessment for the Single Spring, utilizing Equation 17, for deflection yielded an error of 12.55%. Although this error is relatively low, it does not imply the analysis is accurate. Noticeable scatter can be observed within the four recordings in Table 2. Notably, the 1.8 and 3.2 measurements. The maximum deflection for the loading condition of the Single Spring in the FEA is 2.23 mm which is within the realistic scatter of the measurements obtained in Table 2. Therefore, the values of the FEA are valid. The convergence analysis for the Single Spring revealed a variance within 5.34% when the mesh size was changed within ±1% from the base mesh size of 3%, thus the 3% mesh size is only adequate for obtaining rough estimates of the deflection values for the Single Spring.

The percentage error assessment for the Double Spring, utilizing Equation 17, for deflection yielded an error of 46.67%. The reason for this high error is that the method of obtaining the weighted measurements lends itself to human error and unbalanced loading resulting in the variance observed in Table 3. The maximum deflection for the loading condition of the Double Spring in the FEA is 0.77 mm which is within the realistic scatter of the measurements obtained in Table 1. Therefore, the values of the FEA are valid. The convergence analysis for the Double

Spring revealed a variance within 3.51% when a mesh size was changed within ±1% from a base mesh size of 3%, thus the 3% mesh size is only adequate for obtaining an estimate of the deflection values for the Double Spring.

Figure 92 shows the comparison between the FEA spring stiffness. Since the spring stiffness directly affects the static deflection of impact, as shown in Equation 35, increasing the spring stiffness decreases the spring deflection ($\delta_s$). Since $\delta_s$ and total static deflection ($\delta_{st}$) are directly proportional, decreasing the $\delta_s$ decreases $\delta_{st}$. Since the IF has an inverse relationship with $\delta_{st}$, decreasing $\delta_{st}$ increases IF as shown in Equations 34 and 35. A higher IF increases the force of impact as shown by Equation 38. That said the $\delta_{st}$ increases significantly. This increase in static deflection also correlates with a high $\delta_I$ as shown in Equation 37. This maximum deflection of 196 mm is significantly higher than the allowable design deflection of 20 mm, making the impact calculations invalid. Therefore, the higher stiffness of the Double Spring was selected over the lower stiffness of the Single Spring to better qualify the impact calculations. The impact deflection (70 mm) is still not within the allowable design deflection (20 mm) after applying this change, but it is significantly closer to the allowable deflection (20 mm). Ideally, the spring stiffness should be within the allowable design deflection (20 mm). Further research needs to be conducted to devise a better spring design.

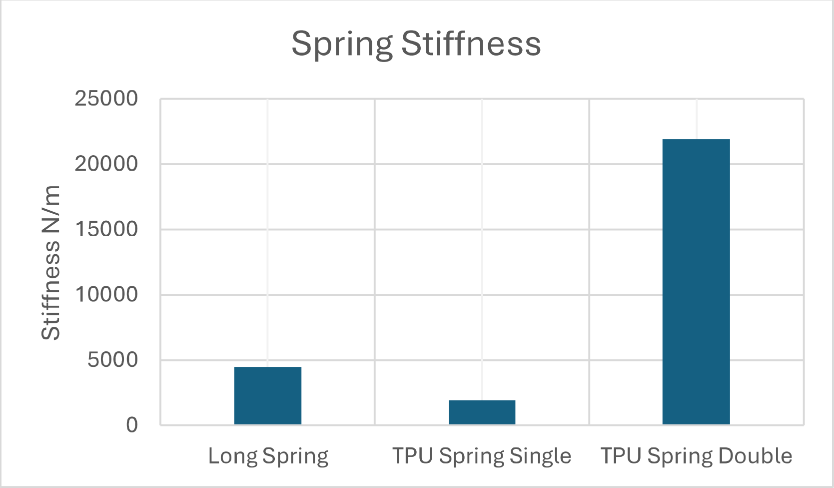

Figure 92: Spring Stiffness (FEA).

# CHAPTER IV

# MANUFACTURING

This chapter will discuss the optimal print settings for optimizing the mechanical properties of FDM components. It begins by reviewing relevant research and ends by examining the information obtained from manufacturing drone components. Notably, this chapter will present the advantages and limitations of FDM.

## 4.1 Slicer Mechanical Properties

### 4.1.1 Optimal Overhang Angle

In the study conducted by Ye et al. (2024), the optimal overhang self-supporting angle was observed to be 60°, with a minimal error of 2.68% between the designed diameter and the measured diameter. The second-best overhang angle was 50° with an error of 8.95% between the diameters. However, it is important to acknowledge the limitations of this study, which include a small sample size and the omission of exploring critical slicer settings such as layer height and print speeds which affect the dimensional accuracy of FDM components.

### 4.1.2 Layer Height Accuracy

In the study conducted by Wu et al. (2018), the dimensional accuracy in the z-axis of FDM components was investigated. The study identified that a layer height of 0.02 mm yielded the least amount of error of 2%. However, due to the significant time investment required to manufacture these components this layer height was not recommended by the researchers. Instead, the researchers recommended a layer height of 0.14 mm with an error of 6%. For this study, the 0.2 mm layer height was selected for its lower time to manufacture compared to the 0.14 mm layer height. Wu et al. observed that a 0.2 mm layer height only had a 0.5% increase in error compared to the 0.14 mm layer height. Notably, Wu et al. work had limitations, which included the material selected (PLA), print temperature, and layer thickness of 2 mm.

### 4.1.3 Layer Height Strength

The YouTube channel “CNC Kitchen” explored the impact of layer height on component strength. In the horizontal orientation, various layer heights yielded similar results, with the strongest layer height observed to be 0.1 mm. In the vertical orientation, the layer height that performed the best was seen to be 0.15 mm. Increasing the layer height above 0.2 mm was observed to drastically decrease the strength of the FDM component. Notably, the study conducted by “CNC Kitchen” had limitations related to the material selected (PLA), the omission of other slicer parameters, and the use of a do-it-yourself (DIY) tensile tester (CNC Kitchen, 2019).

### 4.1.4 Infill Pattern Strength

The mechanical performance of different infill patterns for compression and tension has been discussed by Srinivasan et al, 2020., and the YouTube channels “CNC Kitchen”, “3D Printer Academy”, and “Slant 3D (CNC Kitchen, 2018; 3D Printer Academy, 2024; Slant 3D, 2023; Srinivasan, 2020). In the study conducted by Srinivasan et al. the strongest infill pattern during tensile loading was observed to be grid, the second best was honeycomb. The study conducted by “CNC Kitchen” observed that the strongest infill pattern for both compression and tension was the gyroid infill pattern and the second best was cubic. The study conducted by “3D Printer Academy” observed that the strongest infill was a 3D honeycomb followed by a gyroid. The study conducted by “Slant 3D” observed that the compression strength of an FDM sample increased linearly with the infill percentage. “Slant 3D” also observed that for compression the increase in mechanical performance from 90% to 100% infill was almost double. Notably, the limitations in all these studies include the material selected (PLA), and small sample sizes. Additionally, “CNC Kitchen” and “3D Printer Academy” employed the use of DIY testing machines.

### 4.1.5 Perimeter Count/ Wall Thickness Strength

The effect of the wall thickness on the mechanical performance of manufactured components has been discussed by the YouTube channels “CNC Kitchen”, “My Tech Fun”, and “Slant 3D” (CNC Kitchen, 2019; My Tech Fun, 2021; Slant 3D, 2023). In the study conducted by “CNC Kitchen” regarding extrusion width, the following was observed. Out of the tested samples, the samples with an extrusion width increase of 200% had an increase in mechanical performance of 95% compared to an extrusion width of 100%. Additionally, increasing the perimeter count increased the strength by 65% on the extrusion width of 100%. In the study conducted by “My Tech Fun” regarding 100% infill vs Max Wall count the following was observed. Of the tested samples the 100% infill samples were 6% stronger than the Max Wall count samples in tensile and bending loading applications. Additionally, the torsion resistance of the 100% infill samples was 10% greater than the Max Wall with a maximum torque of 2.1 N m. In the first study conducted by “Slant 3D” regarding the mechanical compression resistance the following was observed. As the perimeter count increased so did the compression resistance of the cube. In the second study conducted by “Slant 3D” regarding the perimeter count resistance to shearing loads, the following was observed. As the perimeter count increased the shear resistance increased. Notably, the limitations in all these studies include the small sample sizes, and the scatter in the results observed by “CNC Kitchen” “My Tech Fun”, and “Slant 3D”.

### 4.1.6 Thermal Annealing Strength

In the study conducted by Holcomb et al. (2022), the impact of thermally annealing FDM samples was explored. The following was observed when annealing PETG at various temperatures (50°C, 70°C, 90°C, and 110°C) for 2 and 4 hours. Notably, the ultimate tensile strength (UTS) of neat PETG remained unaffected by the annealing process. Additionally, the UTS of carbon fiber-reinforced PETG (CF-PETG) was observed to be lower than neat PETG before and after annealing.

### 4.1.7 Manufacturing Parameter Conclusions

In the context of FMD, considering the structural integrity of components, engineers should draw parallels with composite materials such as (concrete) and truss structures used in bridges. The combination of various parameters, notably infill and perimeter count directly affect the mechanical performance of FDM components. The engineer must understand the underlying internal loading conditions of the component application to adequately select the proper combination of parameters for the loading application. In the case of a drone assembly the main components such as the Arms, Leg, and BC experience bending loads. The bending loads are maximum on the outer surface of the geometry and zero on the neutral axis. Therefore, increasing the perimeter count and having a lower infill is optimal for these components. The screws and nuts experience axial loading, where the load is applied throughout the entire cross-section. Therefore, it is important to have a high infill percentage and flat print orientation where the layer lines would not be directly loaded.

## 4.2 Study Parameter Selection

All components were manufactured using the following printing parameters on the Prusa slicer. The HIPS used for this study was obtained from the manufacturer Gizmo-Dorks on amazon.com. The PETG used in this study was obtained from the manufacturer Overture on amazon.com. The TPU used in this study was obtained from the manufacturer Amolen on amazon.com. TPU and PETG are hygroscopic materials, for optimal material manufacturability these materials need to be stored in a dry box while manufacturing (Made with Layers (Thomas Sanlanderer), 2021).

### 4.2.1 General Additive Manufacturing Slicing Settings

- Infill Pattern: Cubic
- Infill Percentage: 20%
- Perimeter Count: 5
- Top Layers: 5
- Bottom Layers: 5
- Nozzle Temperature: varies by material (TPU = 235°C, PETG = 245°C, HIPS = 220°C)
- Printing Speed: 40 mm/s for PETG and HIPS, 20 mm/s for TPU
- Nozzle Diameter: 0.4 mm
- Post Processing: none required, except for support material removal
- Bed Temperature: Varies by material (TPU = 60°C, PETG = 70°C, HIPS = 100°C)

- Bed preparation: 3-5 layers of washable glue stick
- Area of Operation: Well-ventilated indoor environment
- Slicer Software: Prusa slicer 2.7.3
- FDM Machine Model: Prusa MK3s+
- Common Errors: Preheat Error, Crash Detection

Specific Settings for Screw and Nut Design:

- Infill Percentage: 100% (for increased strength)
- Perimeter Count: 2 (reduced from 5)

### 4.2.2 Drone Manufacturing

Three drone versions (4, 5, and 6) were manufactured, assembled, and subjected to impact testing. The results of impact testing will be further discussed in Chapter VI.

# CHAPTER V

# TESTING PROCEDURES

This chapter will go into the specific details of the testing procedures followed for the different testing that the drone and components were put through to validate the design and calculations. This chapter will be formatted as laboratory test procedures.

## 5.1 Screw Testing Procedures

1. Preparation of Test Samples:
    1.1. Fabricate four distinct batches of test specimens for each specified additive manufacturing slicing parameter.
2. Test Setup Configuration:
    2.1. Assemble the testing apparatus by procuring a cable pulley system with a maximum load of 600 N, and a loading scale with an accuracy of ±0.1%.
    2.2. Affix the pulley assembly to a stationary structure securely, ensuring that the rotational freedom of the handle is not compromised.
    2.3. Verify the operational status of the load scale by powering on the device.
    2.4. Employ the upper loop attachment from the load scale and lower lobster clasp attachment to connect the load scale to the pulley system and test sample respectively.
    2.5. Establish a rigid anchorage point located 60 millimeters from the pulley.

3. Eye-Nut Attachment:
    3.1. Obtain two eye nuts corresponding to each specific screw size. Integrate the screw into the eye-nut at the midpoint on both ends fully encompassing the test sample, ensuring full thread engagement. Utilize pliers if necessary to apply a torque advantage.
4. Testing Personnel Requirements:
    4.1. Assign two individuals for the testing process: one to document the test via video recording and the other to execute the test.
5. Data Recording Protocol:
    5.1. Construct a tabular format to document each test, either electronically or on paper systematically.
6. Execution of Test:
    6.1. Position one end of the test specimen over the established fixed point and secure the opposite end to the load scale utilizing the lobster claw.
    6.2. Engage the pulley lock by advancing it forward until an audible click is heard.
    6.3. Activated the load scale and calibrate it to measure force in newtons (N).
    6.4. Instruct the recording individual to commence the video and ensure a clear perspective on the load scale readout.
    6.5. The testing operator should initiate the test by verbally specifying the test parameters, including the test number, test print settings, and test screw dimension.
    6.6. The test operator should gradually apply tension to the sample by rotating the pulley handle in a clockwise direction.
    6.7. Upon failure of the test specimen, cease the recording immediately.

   6.8. Review the recorded footage to obtain the failure load value and record it in the designated table for the corresponding test.

7. Repetition and Analysis:
   7.1. Replicate the steps for each test specimen within the same batch.
   7.2. Conduct the procedure for each test specimen.
   7.3. Analyze the compiled data to deduce conclusions and develop plots.

Figure 93 shows the testing setup employed to tensile test the FDM screws. The limitations include non-unilateral loading, non-uniform loading rate, and measurement device (crane scale).

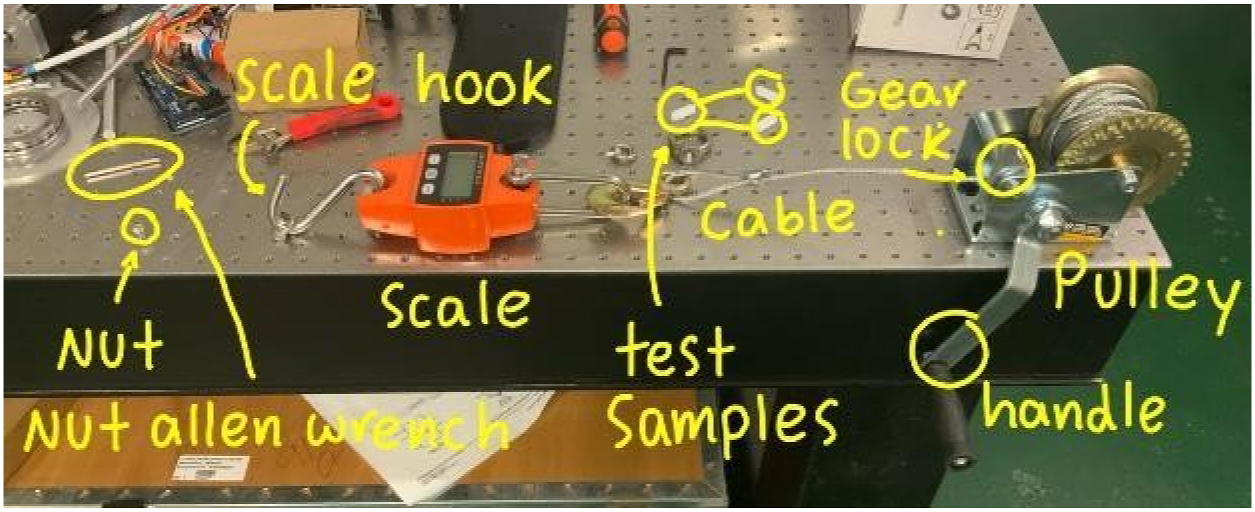

Figure 93: Screw Testing Setup.

## 5.2 Impact Testing Procedures

1. Fabricate the drone components according to the slicing specification for each component discussed in Chapter IV.

2. Assemble the drone as designed:
    2.1. Assemble the drone assembly following the design specifications, ensuring proper integration of all subassemblies and secure attachments of components. Utilization of pliers may be used for torque advantage.
3. Prepare for drop testing:
    3.1. The drop test should be conducted in a controlled environment with a flat unobstructed hard surface and ample vertical space.
4. Personnel Assignment:
    4.1. Allocate roles among three individuals.
    4.2. Test Supervisor: Oversees the test procedure.
    4.3. Data Analyst: Manages data capture and analysis.
    4.4. Technical Assistant: Handles the physical manipulation of the drone.
5. Test Equipment Setup:
    5.1. Gather a high-resolution slow-motion camera (e.g., iPhone 15 Pro), measuring tape, and non-rigid weights (e.g., 5lb ankle weights).
6. Attach the weight:
    6.1. Securely fasten the weights onto the drone, positioning one inside the main body and looping the other one over the top board.
7. Align the height:
    7.1. The Technical Assistant uses the measuring tape to align the bottom of the leg covers with the specified test height
8. Recording Initiation:

    8.1. The Data Analyst begins recording the test in slow motion, ensuring a clear view of the drone throughout the fall and impact.

9. Test Initiation:
    9.1. Before release, the Technical Assistant Verbally states the drone model and specified test height.
10. Stably release the drone to minimize the likelihood of inducing the drone to rotate and land on a single leg.
11. After the drone stabilizes on the ground, stop the recording, and inspect the drone for signs of structural damage such as fractures, cracks, or yielding.
12. If no failure is observed, proceed to the next predetermined drop height and repeat the procedure.
13. Continue the drop test until a structural failure is observed.
14. Review the test recordings to analyze the impact response of the drone and identify the points of failure.
15. Extract keyframes that depict critical movements of the test: the moment of release (drop), the initial response upon impact, the second impact, and the final resting position.
16. Identify any immediate structural deformations that occur during the impact response.
17. Highlight potential weak points in the drone design.
18. Propose design modifications or reinforcements to improve the durability and impact resistance of the drone.

# CHAPTER VI

# RESULTS AND DISCUSSION

This Chapter presents the results of the drone component testing. Additionally, it will correlate the test results with the analytical solutions in Chapter III. The results for the screw designs directly affect the analytical validation for the drone design. An analytical approach could not have obtained this proof strength (Sp).

## 6.1 Screw Testing Results

In this section, the results of the screw testing will be present. Additionally, the results will be analyzed and discussed. The recorded data corresponds to the last observable value from the crane scale before screw failure. Notably, the tested screws were manufactured using HIPS. The testing procedures for the screw test samples were conducted as outlined in Chapter 5.

Table 4: Screw Test 1 [HIPS]

| Screw Test 1 [HIPS] | | | | | | |
|---|---|---|---|---|---|---|
| | **Test 1 [N]** | **Test 2 [N]** | **Test 3 [N]** | **Test 4 [N]** | **Average [N]** | |
| **M5 [HIPS]** | 5.5 | 136.2 | 41.7 | 15.1 | 49.625 | |
| **M10 [HIPS]** | 719.8 | 988 | 950.6 | 925.6 | 896 | |

Table 4 shows the results of tensile testing of the M10 and M5 screws. Notably, the M5 screw tensile proof strength seems to vary drastically between results, whereas the M10 proof strength appears to have less variation. For this reason, the M5 screws should not be implemented in high-loading applications that exceed the lowest value. Figure 94 shows the graphical representation of the values presented in Table 4. The Average $S_p$ for the M10 was 896 newtons.

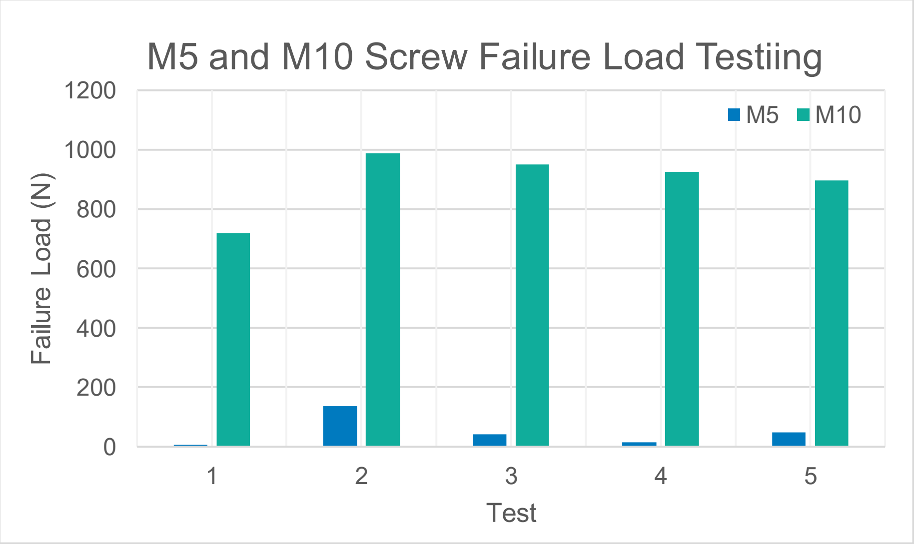

Figure 94: M5 and M10 Screw Failure Load Testing.

Figure 95 shows the M5 failed test samples after testing. Notably, the method of failure is shearing along the treads instead of the cross-sectional area of the screw.

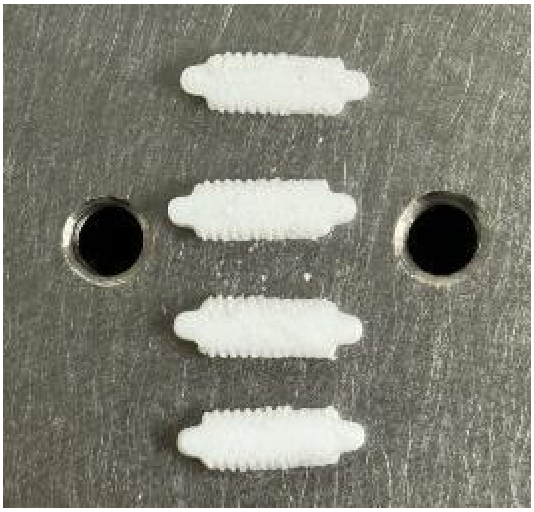

Figure 95: M5 Failed Samples.

Figure 96 shows the M10 failed test samples after testing. Notably, the method of failure is a fracture along the screw midpoint cross-section.

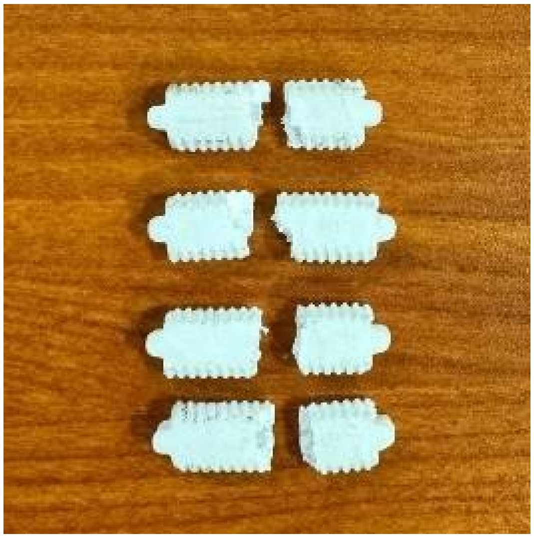

Figure 96: M10 20% Failed Samples.

The conclusion from this testing is that more testing must be conducted to better understand the true $S_p$ of the M10 screws. Notably, the M5 screws need to be redesigned to withstand higher loads. Additionally, during impact testing, the M10 screws failed to resist the impact reaction force. A second test was conducted to analyze if printing parameters for the M10 screws could increase the $S_p$ of the screws. The second test compared the previously printed samples against the new samples of M10 five perimeters, four top and four bottom layers, and 100% infill.

Table 5: Screw Test 2 [HIPS]

| Screw Test 2 [HIPS] | | | | | | | |
|---|---|---|---|---|---|---|---|
| | **Test 1 [N]** | **Test 2 [N]** | **Test 3 [N]** | **Test 4 [N]** | **Test 5 [N]** | **Avg (N)** | |
| **M10 [HIPS] 100%** | 1104 | 1215 | 1264 | 787.9 | 1118 | 1097.78 | |
| **M10 [HIPS] 20%** | 943.7 | 870.7 | 909 | 732.1 | 1019 | 894.9 | |

Table 5 shows the recorded values obtained from tensile testing of the M10 screws at 100% infill and 20% infill. Figure 97 shows the cross-sectional area of the failed samples. Notably, the failure mechanism seems to remain the same regardless of infill percentage.

Figure 97: M10 20% vs 100% Fracture Cross Section.

Figure 98 shows the failed samples for the 100% infill case. Since the failed samples for the 20% infill case closely resembled those in Figure 95 refer to Figure 95 to see the failure mechanism.

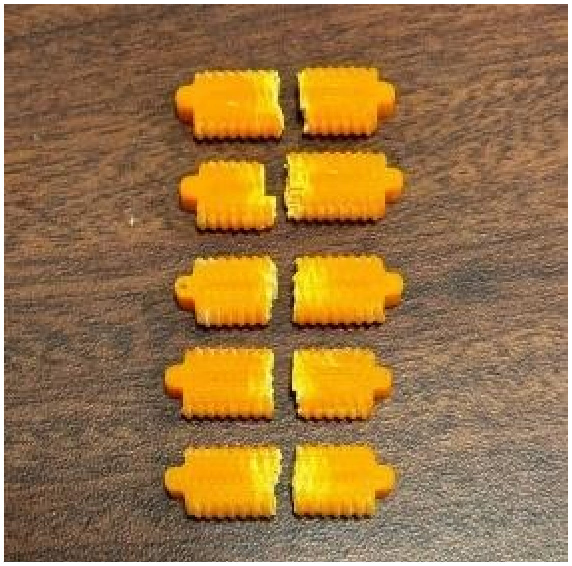

Figure 98: M10 100% Failed Samples.

Based on the test results shown in Table 5 the average proof strength for the M10 100% infill is 1098.2 Newtons. This is an 18.5% increase from the previous proof strength for the M10 20% infill screw which was 895.4 Newtons listed in Table 4. The value for the M10 20% infill observed in Table 5 correlates well with the previous values observed in Table 4. Therefore, the average proof strength for the M10 20% infill is 895 Newtons. If the 100% infill samples follow a similar trend, then the average proof strength for those converges to 1096 Newtons. For the calculations discussed in Chapter 3 the new $S_p$ value for the screws will be 1096 N. Notably, the testing method has some limitations that must be addressed. The first limitation is that this method can only record the failure load and does not provide a stress-strain diagram. The second limitation is the scatter observed within the small sample size, especially for the M5 screw tests. Further testing needs to be conducted on test samples to obtain more accurate failure-proof strength values for these M10 test samples.

## 6.2 Impact Testing Results

Three drone designs were subjected to impact testing. These include drone versions 4, 5, and 6. The testing procedures for the impact testing were discussed in Chapter 5. The results obtained from impact testing are presented below for each drone design.

### 6.2.1 Drone Version 4 Impact Test Results

Figure 99 shows the shearing of Arm V5 near the drone leg after experiencing impact loading.

Figure 99: Drone Version 4 Impact Arm Shearing.

Figure 100 shows the failure of the screw nut on the arm assembly along with the plastic deformation of the Long Spring design incorporated into the Leg design.

Figure 100: Drone Version 4 Impact Nut Shearing and Leg Plastic Deformation.

Figure 101 shows the complete shearing of the Leg design implemented in drone version 4 after being subjected to impact loading.

Figure 101: Drone Version 4 Leg Complete Failure.

The results obtained from impact loading drone version 4 were crucial in addressing the limitations of the design and where to improve and further iterate the design. The first limitation that needed to be addressed was the Long Spring, the second issue was the attachment point for the arm, and the final issue was the shearing on Arm V5. To address the first issue a new spring mechanism was developed (Single Spring). To address the second issue the arm attachment point was split into two with a smaller screw size (M10). This change allowed all the screw connections in the drone to be standard metric screws. To address the shearing of the arms the height of the design was altered so that the stiffness of the arms increased (Arm V8). The material selection was changed from HIPS to PETG due to manufacturing warping issues.

### 6.2.2 Drone Version 5 Impact Test Results

Figure 102 shows the fall of Drone Version 5 from a height of 0.25 m.

Figure 102: Drone Version 5 Impact Drop Height 0.25 m.

Figure 103 shows the initial impact response of Drone Version 5 due to an impact force produced by a drop height of 0.25 m. The springs were completely deformed, and the bottom board was slightly deflected.

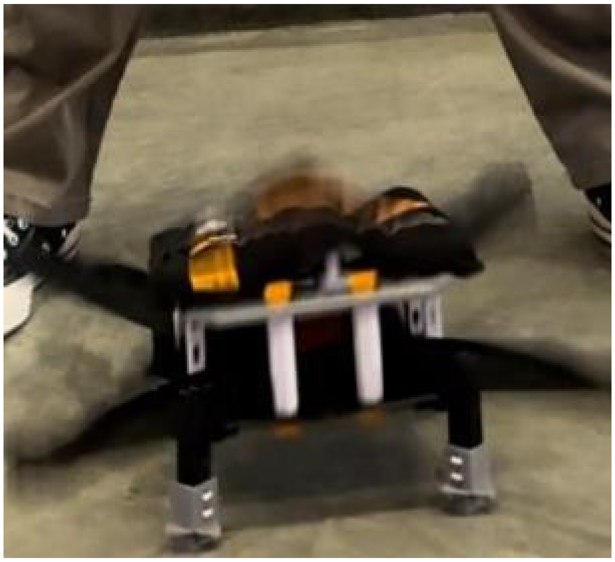

Figure 103: Drone Version 5 Impact Drop Height 0.25 m Initial Impact.

Figure 104 shows the second impact response of Drone Version 5 after the initial impact.

Figure 104: Drone Version 5 Impact Drop Height 0.25 m Impact Response.

Figure 105 shows the final resting position of Drone Version 5 after the second impact. Figure 103 shows that Drone Version 5 survived an impact force produced by a 0.25 m drop height.

Figure 105: Drone Version 5 Impact Drop Height 0.25 m Resting Position.

Figure 106 shows the initial impact response of Drone Version 5 from an impact force produced by a 1 m drop height.

Figure 106: Drone Version 5 Impact Drop Height 1 m Initial Impact.

Figure 107 shows the impact response of Drone Version 5 from a 1 m drop height. Highlighted in the red circle is a visible failure crack.

Figure 107: Drone Version 5 Impact Drop Height 1 m Impact Response.

Figure 108 shows the absolute failure of Drone Version 5 from a drop height of 1 m. The main failure that occurred in the bottom plate near the arm attachment point is highlighted in the figure.

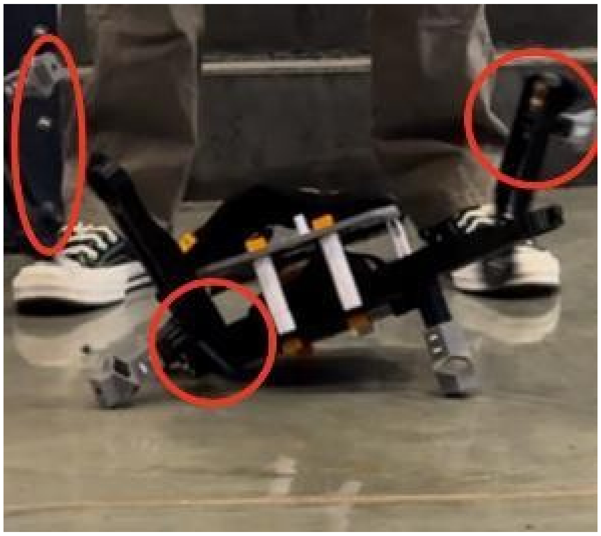

Figure 108: Drone Version 5 Impact Drop Height 1 m Impact Failure.

Figure 109 shows the bottom board of Drone Version 5 after impact testing. The failure shearing occurs near the arm attachment point for all three of the failures observed.

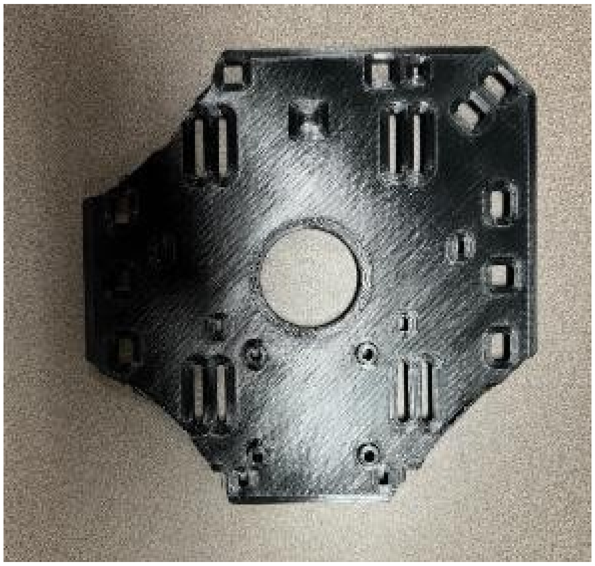

Figure 109: Drone Version 5 Bottom Board.

To address the failures of Drone Version 5 some minor alterations were made to increase its impact resistance. The first alteration was made to the spring mechanism. The stiffness of the spring was increased and an x shape connecting the springs of all the legs was introduced to keep all the feet tethered to one another when experiencing tangential forces. The increased stiffness of the spring mechanisms helped reduce the needed deflection so that the impact force calculated is more accurate than before. Based on these results, the drone's design still needed refinement and impact resistance optimization. The testing shows that the bottom board bends and reacts like a cantilever beam. To increase the stiffness of a cantilever, the mass moment of inertia must be increased. Therefore, the thickness of the bottom board was increased in the subsequent design.

### 6.2.3 Drone Version 6 Impact Testing Results

Figure 110 shows the fall of Drone Version 6 from a height of 1 m.

Figure 110: Drone Version 6 Impact Drop Height 1 m.

Figure 111 shows the initial impact response of Drone Version 6. The drone landing in this test was near ideal with all four springs touching the ground. The spring mechanism absorbed most of the impact force.

Figure 111: Drone Version 6 Impact Drop Height 1 m Initial Impact.

Figure 112 shows the impact response of Drone Version 6 where the stored energy within the springs was released, and the drone assembly got off the ground.

Figure 112: Drone Version 6 Impact Drop Height 1 m Impact Response

Figure 113 shows Drone Version 6 at rest after being subjected to an impact force produced by a drop height of 1 m. Figure 113 shows that Drone Version 6 survived an impact force produced by a 1 m drop height meeting the objective of this study.

Figure 113: Drone Version 6 Impact Drop Height 1 m Resting Position.

Figure 114 shows the fall of Drone Version 6 from a drop height of 1.25 m. The orientation of Drone Version 6 is not ideal and will cause the drone to land on one leg rather than all four.

Figure 114: Drone Version 6 Impact Drop Height 1.25 m.

Figure 115 shows the initial impact response of Drone Version 6 from a drop height of 1.25 m. One of the Legs can be observed to have been deformed and experienced fracture failure. The spring mechanism still had some elastic deformations and stored some of the impact force.

Figure 115: Drone Version 6 Impact Drop Height 1.25 m Initial Impact.

Figure 116 shows the release of the stored energy from the spring mechanism of Drone Version 6. The fracture of the left Leg is more visible in this figure as well.

Figure 116: Drone Version 6 Impact Drop Height 1.25 m Impact Response.

Figure 117 shows the final resting position of Drone Version 6 where most of the assembly is intact except the left Leg. Therefore, Drone Version 6 did not survive an impact force produced by a drop height of 1.25 m.

Figure 117: Drone Version 6 Impact Drop Height 1.25 m Resting Position.

The results of the final testing for Drone Version 6 show that this drone design has key points of failure that are designed in a controlled manner that will fail under certain impact conditions and that this drone design also proved to keep the main shell intact during impact protecting the electrical components inside. After reviewing the performance of the HIPS screws and nuts, the components were observed to have yielded during the impact testing. For this reason, the selection of the materials for most components was altered to PETG except for the M10 and M5 standoffs.

# CHAPTER VII

# CONCLUSIONS AND FUTURE WORK

## 7.1 Conclusion

Designing components for fused deposition modeling FDM is an ongoing challenge. The work presented here is a valid approach to designing, validating, and optimizing components for FDM. One critical FDM parameter must be tuned to meet the homogenous criterion for analytical and FEA analyse to apply to FDM components. The parameter that must be tuned is the cross-section of the part, at the point of failure (My Tech Fun, 2020; My Tech Fun 2021, Slant 3D 2023; Srinivasan, 2020). To be considered homogenous the part must be at 100% infill so that the cross-section can be regarded as homogenous. It is important to note that, FDM components will never be truly homogenous due to the imperfections of the process.

### 7.1.1 FDM Homogenous Methods

There are two methods by which an FDM component can reach 100% solid cross-sectional area. The first method is to select the 100% infill option in the slicer profile. The second is to increase the number of perimeters until the part is essentially nothing but perimeters. The strength variation between the two was observed to be minimal for tension applications. In torsion, the 100% infill samples were stronger than the Max Wall design (“My Tech Fun”). For a drone assembly where weight is a limiting factor, these methods are not optimal for FDM components.

Instead, a variation of partial infill and perimeter count is optimal (CNC Kitchen, 2019; My Tech Fun, 2021; Slant 3D, 2023). The optimal perimeter count discussed in Chapter IV was selected for being the least number of perimeters required to make all the components homogenous at the point of failure. For these applications, the infill parameter contributes to the mechanical performance of FDM components. The Best overall infill pattern for weight is gyroid (3D Printer Academy, 2024). The best infill for bending in Prusa slicer 2.7.3 is cubic (CNC Kitchen, 2018). Since the screws experienced the most loading during impact the optimal printing parameters for these components were selected to be the 100% infill with two perimeter count variations as discussed in Chapter IV.

### 7.1.2 Design For FDM

When designing for fused deposition modeling (FDM), it is important to consider several critical factors. These include the understanding of the loading conditions, stress concentrations, and the limitations/advantages of FDM. The best screw design is the two-slice approach for M10 and M6, while threaded nuts should be manufactured oriented horizontally on the build plate (My Tech Fun, 2020). Additionally, addressing horizontal overhangs requires strategic support placement, such as chamfering bottom surfaces or implementing overlapping bridging (Macro 3D Prints, 2023: Slant 3D, 2023).

## 7.2 Future Work

The future work for this project involves the implementation of sensors embedded into the design, conducting a vibration analysis on the drone arm induced by the electric brushless motors during flight, conducting an aerodynamic analysis for the coefficient of drag of the drone, and running a topological optimization for the drone components.

### 7.2.1 Sensor Development

To embed sensors or any other sensors or bodies into an additive manufacturing component the following steps must be taken: (1) measure the sensor's dimensions and create a container for the sensors; (2) embed the container design into the bottom board or any other body design; (3) during the slicing process for FDM, insert a break in the print a layer before the housing for the sensor is covered and embedded into the design; (4) during printing, when the break occurs at the insert the sensor and resume the print. The development of Sensors using compliant mechanisms and FDM has been discussed by (BubsBuilds, 2024; Turbo_Sunshine, 2020). The development of FDM electrical resistors with conductive filaments has been discussed by Jaksic et al. (Jaksic, 2019).

### 7.2.2 Sensor and Drone Limitations Considerations

The effect of airflow over luminescence sensors has been discussed by Noh et al. (Noh, 2022). As the airflow increased, so did the detection of TNT particles by the sensors. The motors will produce a vibration frequency on the drone arms. The natural frequencies for the arm must be calculated to make sure that the motors do not make the arms resonate. The analysis for obtaining and calculating the natural frequencies of a cantilever beam has been discussed in (Vlab, 2011). The effect color has on an FDM part regarding the heat absorbed by the component is a factor that needs to be further analyzed (Science Buddies, 2024).

### 7.2.3 Weight Optimization

To reduce the weight of the manufactured components the components must be further optimized for the loading conditions using topology optimization (CNC Kitchen, 2018). Fusion 360 has an intuitive topology optimization simulation that costs credits but can be beneficial to help optimize the weight-to-strength ratio of the drone. The YouTube channel “CNC Kitchen” has discussed how adding load-dependent infill increases the strength of additively manufactured components (CNC Kitchen, 2019). Another method of weight reduction can be from changing the infill structures Palomba et al. discussed the use of custom infill patterns to provide better strength-to-weight ratios than traditional infill patterns in slicer software (Palomba, 2022). Another method of reducing the drone's weight by 20% without completely remodeling the drone is by changing the PETG components for ASA components which are 20% lighter. The rationale for not implementing ASA during this study was a concern about not having the appropriate facilities to manufacture components with ASA (CNC Kitchen, 2020), which require proper ventilation.

# REFERENCES

AlexPrint. (2023). FDM vs SLA Explained - APM Designs. Retrieved 2023, from APM Designs.com.

Allain, R. (2019). Calculate the Thrust Force on Your Drone! Retrieved 2023, from Wired.com.

Attaran, M. (2017). The rise of 3-D printing: The advantages of additive manufacturing over traditional manufacturing. Business Horizons, 60(5), 677-688.

Brendan22. (2014). T4 Quadcopter Mini 250 Drone (5 Inch Props) by Brendan22. Retrieved 2023, from UltiMaker Thingiverse.

Bryant, A. (2024). Best Budget 3D Printers 2024: High-Quality Output on the Cheap. Retrieved 2024, from Tom's HARDWARE.

BubsBuilds. (2024). Building and Calibrating 3D Printed Sensor to Better than 5 Micrometers, And It Cost Me under $10. Retrieved 2024, from YouTube.

Buswell, R. A., De Silva, W. L., Jones, S. Z., & Dirrenberger, J. (2018). 3D printing using Concrete extrusion: A roadmap for research. Retrieved 2032. from Cement and concrete research, 112, 37-49.

CNC Kitchen. (2019). Extrusion Width - The Magic Parameter for Strong 3D Prints. Retrieved 2023, from YouTube

CNC Kitchen. (2019). Load Dependent Infill Placement: Smart Infill for FDM 3D Prints!. Retrieved 2023, from YouTube.

CNC Kitchen. (2018). Testing 3D Printed Infill Patterns for Their Strength. Retrieved from 2023, YouTube.

CNC Kitchen. (2020). The Best 3D Printing Material? Comparing PLA, PETG & ASA (ABS) Feat. Prusament by Josef Prusa. Retrieved 2023, from YouTube.

CNC Kitchen. (2018). Tutorial: Topology Optimization in Fusion 360 – 3D Printing Filament Spool Holder. Retrieved 2023, from YouTube.

CNC Kitchen. (2019). Which Layer Height Gives You the Strongest 3D Prints? Retrieved 2023, From YouTube.

Davies, M. (2023). How Heat Resistant Is PETG? (Detailed Analysis). Retrieved 2023, from 3D Print Beast.

Dogan, O. (2022). Short-term creep behavior of different polymers used in additive manufacturing under different thermal and loading conditions. Retrieved 2023, from Strojniški Vestnik - Journal of Mechanical Engineering, 68(7–8), 451–460.

Dynamism. (2016). Technical data sheet TPU 95A. Retrieved 2023, from Dynamism.com

3D Printer Academy. (2024). This 3D Printer Infill Is the Strongest (3D Printer Academy Tested Episode 2). Retrieved 2024, from YouTube.

3DSourced. (2024). How to Anneal 3D Prints for Strength (Nylon, ABS & PLA). Retrieved 2024, from 3DSOURCED.com.

EngineersEscape. (2019). How a Quadcopter Works - Flight Mechanics, Components, & Sensors (2). Retrieved 2023, from YouTube.

FAA. Fact Sheet – Small Unmanned Aircraft Systems (UAS) Regulations (Part 107). The U.S. Mission to the International Civil Aviation Organization. Retrieved 2023, from icao.usmission.gov.

Freedman, Z. (2021). I Tested (Almost) Every Filament on Amazon: Every Single Filament Part I. Retrieved 2023, from YouTube.

Gadget Flow. Droneball Collision Tolerant Drone. Retrieved 2023, from TheGadgetFlow.com

Gleadall, A. (2021). FullControl GCode Designer: Open-source software for unconstrained Design in additive manufacturing. Retrieved 2023, from Additive Manufacturing, 46, 102109.

GlebS. (2023). Vibration of a Cantilever Beam. Natural Frequency of Cantilever Beam Online Calculator. Retrieved 2024, from calcdevice.com.

Guidelines for the Collection of Long-Term Pavement Performance Data. U.S. Department of Transportation Federal Highway Administration. Retrieved 2023, from highways.dot.gov.

Hassanalian, M., & Abdelkefi, A. (2017). Classifications, applications, and design challenges of Drones: A review. Retrieved 2023, from Progress in Aerospace Sciences, 91, 99-131.

Hergel, J., Hinz, K., Lefebvre, S., & Thomaszewski, B. (2019). Extrusion-based ceramics Printing with strictly continuous deposition. Retrieved 2023, from ACM Transactions on Graphics (TOG), 38(6), 1-11.

Holcomb, G., Caldona, E. B., Cheng, X., & Advincula, R. C. (2022). On the optimized 3D Printing and post-processing of PETG materials. Retrieved 2023, from MRS communications, 12(3), 381-387.

Holybro. (2023). S500 V2 Kits. Retrieved 2023, from Holybro Store.

Holybro. (2023). X500 V2 Kits. Retrieved 2023, from Holybro Store.

Hsueh, M. H., Lai, C. J., Wang, S. H., Zeng, Y. S., Hsieh, C. H., Pan, C. Y., & Huang, W. C. (2021). Effect of printing parameters on the thermal and mechanical properties of 3d printed pla and petg, using fused deposition modeling. Retrieved 2023, from Polymers, 13(11), 1758.

Jaksic, N. I., & Desai, P. D. (2018). Characterization of resistors created by fused filament Fabrication using electrically conductive filament. Retrieved 2023, from Procedia Manufacturing, 17, 37-44.

Last, B. (2023). Will PETG Melt in the Sun? The Definitive Answer. Retrieved 2023, from Printing It 3D.

Liu, X., Tang, G., & Zou, W. (2021). Improvement of Detection Accuracy of Aircraft in Remote Sensing Images Based on YOLOV5 Model. Retrieved 2023, from 2021 IEEE International Geoscience and Remote Sensing Symposium IGARSS (pp. 4775-4778). IEEE.

Macro 3D Prints. (2023). 10 EASY Compliant Mechanisms to 3D Print First 2023. Retrieved 2023, from YouTube.

Made with Layers (Thomas Sanladerer). (2024). Do You Even Need Threaded Inserts? Strength Tested!. Retreived 2024, from YouTube.

Made with Layers (Thomas Sanladerer). (2021). Do You Really Need to Dry Your Filament?. Retrieved 2023, from YouTube.

McMaster. (2023). Combination Phillips, Slotted, and Rounded Head Screws. Retrieved 2023, from McMaster website.

MakeItFrom.Com. (2020). Thermoplastic. Glycol-Modified-Polyethylene-Terephalate-PETG. Retrieved 2023, from MakeItFrom.com.

MakeItFrom.Com. (2020). Thermoplastic. High-Impact-Polystyrene-HIPS. Retrieved 2023, from MakeItFrom.com.

Maker's Muse. (2017). How Accurate Is Your 3D Printer? Take the Tolerance Test!. YouTube.

Micro Unmanned Aircraft Systems Aviation Rulemaking Committee (ARC) (2016). ARC Recommendations Final Report. FAA. Retrieved 2023 from FAA.gov.

Miller, L. (2023). 3D Printed Drones from Thingiverse Worth Making. Retrieved 2023, from Learn Robotics.

My Tech Fun. (2021). Creep Test with 3D Printed Plastic Materials: PLA, PETG, ASA, Nylon. Retrieved 2023, from YouTube.

My Tech Fun. (2020). 3D Printed Screw Nuts - Horizontal or Vertical Printing Position Is Better?. Retrieved 2023, from YouTube.

My Tech Fun. (2021). 100% Infill vs Max Number of Walls (or Perimeters or Shells) - Which Is Stronger for Solid Object?. Retrieved 2023, from YouTube

My Tech Fun. (2022). Maybe Too Detailed Flex Filament Test - Polymaker TPU90 vs TPU95 vs TPU95-HF. Retrieved 2023, from YouTube.

My Tech Fun. (2020). Testing Horizontally 3D Printed Bolts without Supports - How Strong Are These Sliced Screws?. Retrieved 2023, from YouTube.

Muralidharan, N., Pratheep, V. G., Shanmugam, A., Hariram, A., Dinesh, P., & Visnu, B. (2021). Structural analysis of mini drone developed using 3D printing technique. Retrieved 2023, from Materials Today: Proceedings, 46, 8748-8752.

Noh, D., Ampadu, E. K., & Oh, E. (2022). Influence of Air Flow on Luminescence Quenching in Polymer Films Towards Explosives Detection Using Drones. Retrieved 2023, from Polymers, 14(3), 483.

Nolan5454, & Instructables. (2017). 3D Printed Quadcopter with Arduino. Retrieved 2023, from Instructables.

Palomba, G., Crupi, V., & Epasto, G. (2022). Additively manufactured lightweight monitoring drones: Design and experimental investigation. Retrieved 2023, from Polymer, 241, 124557.

Pecho, P., Ažaltovič, V., Kandera, B., & Bugaj, M. (2019). Introduction study of design and layout of UAVs 3D printed wings in relation to optimal lightweight and load distribution. Retrieved 2023, from Transportation Research Procedia, 40, 861-868.

Phan, H. V., & Park, H. C. (2020). Mimicking nature's flyers: a review of insect-inspired flying robots. Retrieved 2023, from Current Opinion in Insect Science, 42, 70-75.

Polygenis, T. (2023). ABS VS PETG: A Comprehensive Comparison for 3D Printing Materials. Retrieved 2023, from Wevolver.

Prusa Knowledge Base. (2023). Crash detection. Retrieved 2023, from Help.Prusa3D.com

Prusa Knowledge Base. (2023). How to replace a hotend (MK3S/MK3S+). Retrieved 2023, from Help.Prusa3D.com.

Prusa Knowledge Base. (2023). Insert Pause or Custom G-Code at Layer. Retrieved 2023, from Help.Prusa3D.com

Prusa Knowledge Base. (2023). Preheat error. Retrieved 2023, form Help.Prusa3D.com.

RCLifeOn. (2020). A Flexible 3D Printed Drone That Can't Break. Retrieved 2023, from YouTube.

RCLifeOn. (2017). 3D Printed Drone Propellers - Will It Work?. Retrieved 2023, from YouTube.

Rechtin, M. (2024). Building a DIY 3D Printed FPV Race Quad. Retrieved 2024, from YouTube.

Robby-the-Robot. (2020). Super Simple 3D Printed Drone Build. Retrieved 2032, from Instructables.

Roy Mech. (2023). Screw thread Calculations. Retrieved 2023 from RoyMech.org.

Science Buddies. (2024). How Does Color Affect Heating by Absorption of Light? Retrieved 2024, from SCIENCEBUDDIES.org

Shaikhnag, A., Tyrer-Jones, A., Hanaphy, P., & 3D Printing Industry. (2020). How to Accurately Price for Stereolithography (SLA) 3D Printing Projects. Retrieved 2023, from 3D Printing Industry.

Slant 3D. (2023). Design Snap Fits for Mass Production 3D Printing. Retrieved 2023, from YouTube.

Slant 3D. (2023). 3D Printing Basics: Understanding and Managing Support Material. Retrieved 2023, from YouTube.

Slant 3D. (2023). From 10% to 100%: Infill Compression Strength. Retrieved 2023, from YouTube.

Slant 3D. (2023). How Does Wall Thickness Affect 3D Printed Part Strength? | 3D Printing Testing Lab. Retrieved 2023, from YouTube.

Slant 3D. (2023). Joining Features | Design for Mass Production 3D Printing. Retrieved 2023, form YouTube.

Slant 3D. (2023). Threaded Holes & Inserts | Design for Mass Production 3D Printing. Retrieved 2023, from YouTube.

Srinivasan, R., Kumar, K. N., Ibrahim, A. J., Anandu, K. V., & Gurudhevan, R. (2020). Impact of fused deposition process parameter (infill pattern) on the strength of PETG part. Retrieved 2023, from Materials Today: Proceedings, 27, 1801-1805.

Stanton, T. (2016). 3D Printed Plane - Will It Fly?. Retrieved 2023, from YouTube.

Stanton, T. (2022). How I Designed a 3D Printed Wing. Retrieved 2023, from YouTube.

Stanton, T. (2022). Optimizing a VTOL. Retrieved 2023, from YouTube.

Su, A., & Al'Aref, S. J. (2018). History of 3D printing. Retrieved 2023, from In 3D printing applications in cardiovascular medicine (pp. 1-10). Academic Press.

Szyk, B. (2023). Drone Flight Time Calculator. Retrieved 2023, from Omni Calculator.

Tangled Testing. (2024). Testing Wall Thickness in 3D Printed Beams. Retrieved 2024, from YouTube.

Treyes4. (2017). Make an H Quadcopter with 3D Printing. Retrieved 2023, from Instructables

Trivedi, A. K., Gupta, M. K., & Singh, H. (2023). PLA based biocomposites for sustainable products: A review. Retrieved 2023, from Advanced Industrial and Engineering Polymer Research, 6(4), 382-395.

Turbo_SunShine. (2020). Dial Indicator Using Compliant Mechanisms. Retrieved 2023, from YouTube.

Valvez, S., Silva, A. P., & Reis, P. N. (2022). Compressive behavior of 3D-printed PETG composites. Retrieved 2023, from Aerospace, 9(3), 124.

Vlab.amrita.edu,. (2011). Free Vibration of a Cantilever Beam (Continuous System). Retrieved 2023, from vlab.amrita.edu.

Wu, J. (2018). Study on optimization of 3D printing parameters. In IOP conference series: materials science and engineering (Vol. 392, p. 062050). IOP Publishing.

Xometry. (2023). All about Hips 3D Printing Filament: Materials, Properties, Definition. Retrieved 2023, from Xometry.com.

Xometry. (2022). SLS vs. FDM: Differences and Comparisons. Retrieved 2023, from Xometry.

Yap, Y. L., Toh, W., Giam, A., Yong, F. R., Chan, K. I., Tay, J. W. S., ... & Ng, T. Y. (2023). Topology optimization and 3D printing of micro-drone: Numerical design with experimental testing. Retrieved 2023, from International Journal of Mechanical Sciences, 237, 107771.

Ye, J., Lin, X., Lu, H., Shen, H., Wang, Z., & Zhao, Y. (2024). Layout and geometry optimization design for 3D printing of self-supporting structures. In Structures (Vol. 59, p. 105699). Elsevier.

# VITA

Alan Salvador Urteaga pursued his educational career as an undergraduate student at the University of Texas Rio Grande Valley, where he graduated Magma Cum Laude with a bachelor’s degree in mechanical engineering in December 2022. Alan continued his education at the University of Texas Rio Grande Valley. Alan continued developing his engineering skills and knowledge in designing and manufacturing products using additive manufacturing to help bring products to consumers. Alan completed his Master of Science in Engineering degree in Mechanical Engineering in May 2024. Alan Salvador Urteaga can be reached at alan.urteaga01@gmail.com